Singlet Exciton Fission, a Multi-Exciton Generation Process, in Organic Semiconductor Solar Cells

by

Priyadarshani Jadhav

B.E.(Honors) Electrical and Electronics,
Birla Institute of Technology and Science, Pilani, India (1993)
M.Sc. (Honors) Physics,
Birla Institute of Technology and Science, Pilani, India (1993)
M.S. Electrical Engineering, Boston University, (1995)

Submitted to the Department of Electrical Engineering and Computer Science
in Partial Fulfillment of the Requirements for the Degree of

Doctor of Philosophy

at the

MASSACHUSETTS INSTITUTE OF TECHNOLOGY

June 2012

Author .....
Department of Electrical Engineering and Computer Science
May 16, 2011

Certified by.....
Marc A. Baldo
Professor of Electrical Engineering and Computer Science
Thesis Supervisor

Accepted by .....
Leslie A. Kolodziejski
Professor of Electrical Engineering and Computer Science
Chair of the Committee on Graduate Students

Singlet Exciton Fission, a Multi-Exciton Generation Process, in Organic Semiconductor Solar Cells

by
Priyadarshani Jadhav

Submitted to the Department of Electrical Engineering and Computer Science
on May 16, 2012 in Partial Fulfillment of the Requirements for the Degree of Doctor of Philosophy in Electrical Engineering and Computer Science

ABSTRACT
Organic semiconductor photovoltaics hold the promise of cheap production and low manufacturing setup costs. The highest efficiency seen in research labs, ~10% today, is still too low for production. In this work we explore implementations of a multiple exciton generation process, singlet exciton fission, to work around the Shockley-Queisser limit, according to which, all single junctions cells have a theoretical efficiency limit of 33.7%.

This is the first implementation of a singlet fission photovoltaic. We measured a singlet fission efficiency of 72% at room temperature. We showed that singlet fission can be implemented in bulk heterojunction photovoltaics, which is an important result since some of the highest efficiency organic photovoltaics in the last 5 years have been bulk heterojunction structures.

Secondly, we showed that the magnetic field effect can be used as a probe to investigate triplet dissociation in singlet fission devices.

Thirdly, we implemented singlet fission photovoltaics, using the singlet fission material pentacene as donor and low bandgap infrared-absorptive lead chalcogenide quantum dots as acceptors. Singlet fission can enhance the efficiency of organic photovoltaics only if the fission material is paired with an absorptive low-energy-gap material. We find that pentacene triplet excitons dissociate at the pentacene/quantum dot heterojunctions with an internal quantum efficiency of 35%.

Lastly, we investigate a series of materials to find a better acceptor in singlet fission photovoltaics using the methods and some results from the previous two investigations. We investigate device structures that pair pentacene and 6,13 diphenyl-pentacene as singlet fission donors with C_{60}, perylene diimides, PbS quantum dots and PbSe quantum dots as acceptors.

Thesis Supervisor: Marc A. Baldo
Title: Professor of Electrical Engineering and Computer Science

Acknowledgements

I am wholly indebted to my advisor Marc Baldo for his continued guidance and encouragement through the duration of my graduate studies at MIT. From Marc Baldo, I have learnt not just what comprises good scientific research, but also a new way of looking at scientific research and its place in the world.

I would like to thank my wonderful lab-mates, current and past, for all the interesting research discussions and help in the lab. I would especially like to thank Patrick Brown for teaching me how to work with quantum dots, Aseema Mohanty for all her help in the tetracene photovoltaic project. I would like to thank Nicholas Thompson for his contribution with the pentacene devices and the magnetic field effect measurement system.

I am grateful to all the funding agencies that have made my stay at MIT possible including the Center for Excitonics, funded by the US Department of Energy, and DuPont.

I am very thankful for the support and encouragement of my parents and the rest of my family. To my friends in Cambridge, thanks for being there for me and for providing much needed distractions.

Contents

1 Introduction

Solar energy strikes the surface of the earth at about 1.4×10^8 TWH annually, calculated using a very rough 3KWH/m^2 average daily insolation. Compared to this figure, world energy consumption which was 98,000 TWH in 2008 out of which electricity consumption was 16,700 TWH, is only a fraction.[1] So at about 10% solar cell efficiency, only 1% of the earth's surface can potentially satisfy the world's energy requirements. At present though the cost of photovoltaic generated electricity is 2-4 times the cost of grid electricity This makes the pursuit of more efficient and cheaper photovoltaics a very worthwhile task.

The state of the art of organic semiconductor photovoltaics (OPV) at the time of writing of this thesis is at 10.6% efficiency – a cell made by Sumitomo Chemicals and researchers at UCLA.[2] The promise of OPVs is cheaper, lightweight, flexible devices, and also versatility in synthesis of new materials which can provide control over the rational design of the most efficient cells possible. This chapter deals with a brief description of the photovoltaic landscape today – the various technologies, associated costs, energy payback times, and how OPVs compare.

1.1 Prominent photovoltaic technologies

Silicon is the most commonly used photovoltaic(PV) technology due to its abundant availability and its use in the computer industry. 80-90% of installed panels are crystalline silicon (c-Si).[3] The thickness of these cells is typically between 100-300μm due to the low absorption of silicon. The absorption coefficient of silicon is around 10^2-$10^5 cm^{-1}$ in the 400-950nm wavelength range, which requires a thickness of up to several 10μm for a sufficiently efficient cell. The difficulty of handling thin wafers requires them to be made thicker.

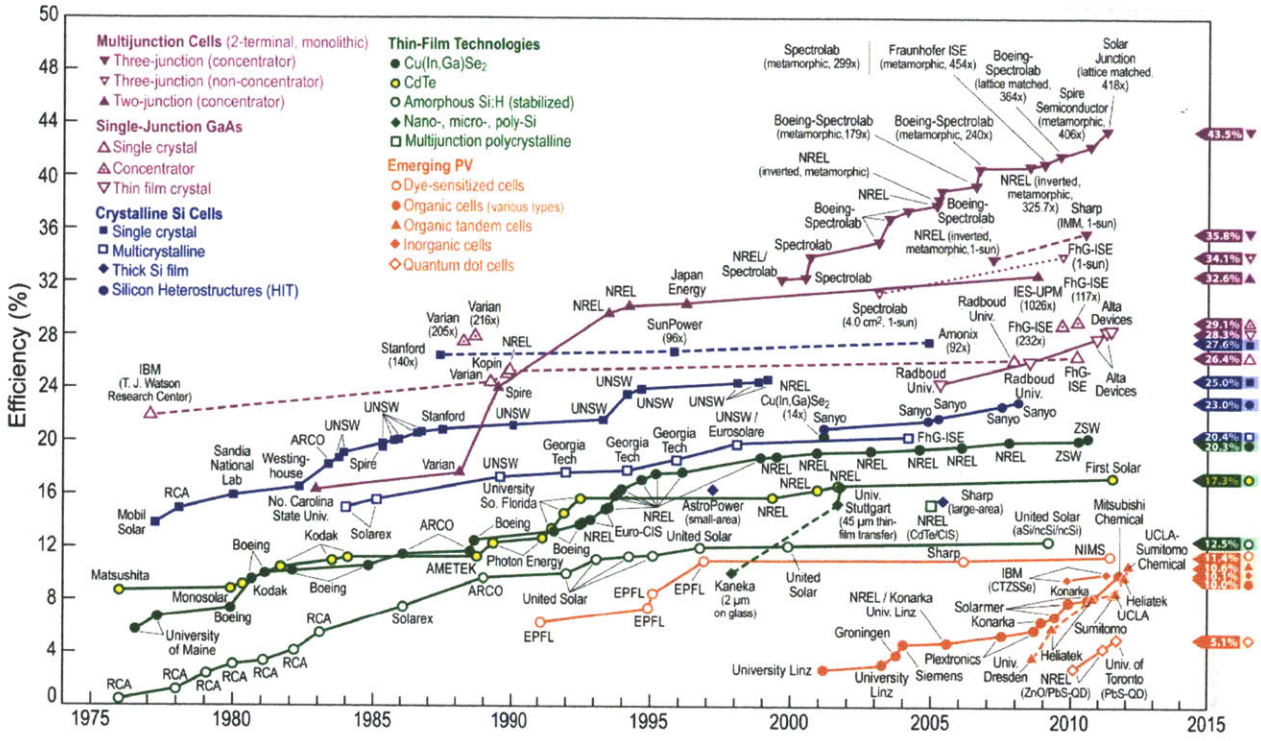

Figure 1.1 Best research-cell efficiencies plot maintained by the National Renewable Energy Laboratory (NREL). [4]

In contrast, technologies like **CadmiumTelluride(CdTe)** and **Copper Indium Gallium diSelenide(CIGS)** have much higher absorption and the crystals are grown up to 10µm thick films on coated glass or steel substrates. These cells are cheaper than c-Si due to the reduced material usage, but are also less efficient. CdTe has a band gap of 1.5eV which is very close to optimum value for the solar spectrum. Currently, CdTe modules have the lowest $/W cost in the market.[5] CIGS has very high absorption, and are much thinner. Industry has not yet been able to reduce the large efficiency gap between lab and production performance.

Table 1.1 Prominent Solar Cell Technologies

Technology	Best research efficiency(%) ₸	Production efficiency (%)	$/$W_p$*	Energy Payback Time (Yrs)	Approx. Thickness (μm)	Band gap (eV)
Monocrystalline -Si	27.6	15-23	1.10	2.1[6]	200-300	1.1
Multicrystalline-Si	20.4	15-17	1.06	1.6[6]	200-300	1.1
Cadmium Telluride	17.3	14.4[7]	0.84	.8[6]	10[8]	1.5[8]
Copper (Indium, Gallium) diSelenide(CIGS)	20.3	13.8[9]			1-2[10]	1.1[11]
Amorphous-Si	12.5	7-9				1.7
Organic semiconductors	10.6	3[12]		Few weeks[13]	300nm	~>1.7

₸ From NREL website

* From www.solarbuzz.com

The $/$W_p$ is the cost of panel divided by the power generated at AM1.5 solar radiation and 25°C at a load that results in maximum power output. The figure is a good direct measure of comparison in certain low requirement settings like homes which do not have grid electricity and could use the power to run a couple of light bulbs. The **Levelized Cost of Electricity**(LCOE) which takes into account Balance of System(BOS) costs that include installation, land use and maintenance, and lifecycle analysis, is a better number for solar farms and it depends on the efficiency of the module as well as the $/$W_p$. Higher efficiency lowers the LCOE since the BOS cost per watt produced is lower.

Triple junction solar cells are the most efficient solar cells manufactured to date. They are tandem cells, which are structures that essentially stack a series of solar cells on top of each other in the path of solar radiation (see Figure 2). Each cell in the stack is optimized to absorb and use a different wavelength range of the solar spectrum. In contrast, single junction cells (which is what all the technologies

described above have been), are optimized for a single wavelength of light and are limited to a theoretical efficiency of 33% known as the Shockley-Queisser limit.[14] A production quality GaInP/GaInAs/Ge cell from Solar Junction, San Jose CA, reached 43.5% at 400 suns in April 2011.[15] Singlet exciton fission, the phenomenon applied to OPVs in this work, is a potential work-around to the Shockley-Queisser limit in a single junction cell. Lattice matching requirement of the different inorganic semiconductors in the stack makes these cells very expensive.

Organic semiconductor photovoltaics are thin film devices with total thicknesses around 300-400nm. In addition they are amorphous and have low purity requirements and results in cheaper manufacturing methods like roll-to-roll printing. Organic semiconductor materials and OPVs are developed in detail in the next couple of chapters.

2 Organic semiconductors

Organic semiconductors are carbon based compounds with weak van der Waal's forces holding the molecules together. Some examples are illustrated in **Figure 2.1**. The weak intermolecular forces leads to narrow electronic bandwidth and unlike covalently bonded crystals there is no band transport. Charge transport takes place by thermally assisted hopping and charge carrier mobilities are generally low: from $3x10^{-6}$ cm^2/Vs in AlQ_3 which forms very amorphous thin films, to 15 cm^2/Vs in rubrene crystal.[16, 17] The low mobilities makes organic semiconductors an unlikely candidate for high speed electronics, but a lot of the interest in organic semiconductors is due to their optoelectronic properties. They emit and absorb light in the visible part of the spectrum, hence their application in Organic semiconductor LEDs (OLED) and in photovoltaics. The very first application of organic semiconductors was in photocopier machines in the 1970s.

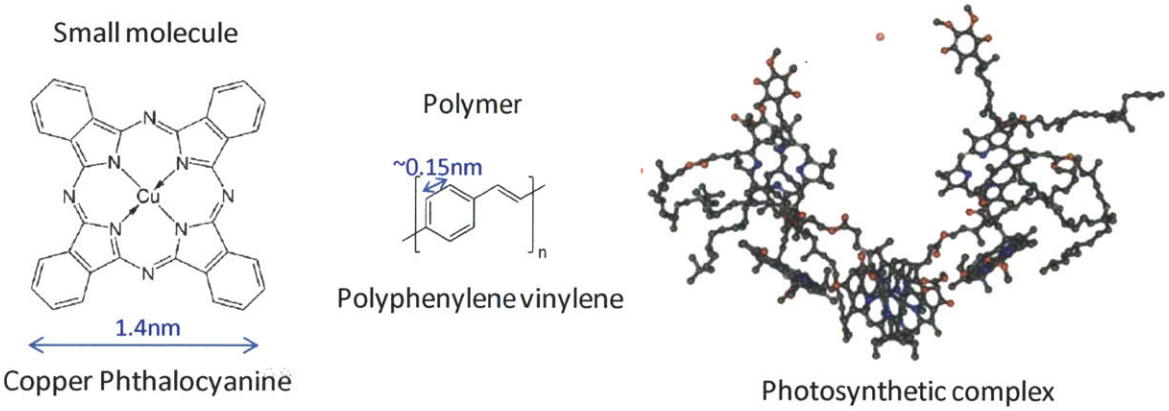

Figure 2.1 Examples of organic semiconductor molecules (a) Copper Phthalocyanine dimensions from[18]

2.1 Conjugation

Because of the weak intermolecular bonds in organic solids, the properties of the solid are very similar to the properties of the individual molecules and so it is important to look at the properties of the individual molecules.

In its ground state, a carbon atom has the atomic orbitals $1s^2 2s^2 2p^2$, two paired electrons in the 2s orbital and two unpaired electrons in two 2p orbitals (out of three 2p orbitals) and hence form two bonds. Or it could exist as $1s^2 2s^1 2p_x^1 p_y^1 p_z^1$, with four unpaired electrons and hence form four bonds.

But instead in methane – CH_4 – carbon forms four equivalent bonds with the four hydrogen atoms. In 1931 Linus Pauling explained this structure of a methane molecule through hybridization. [19]

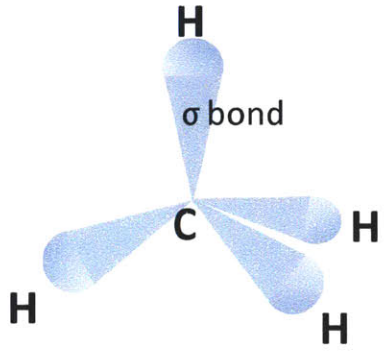

Figure 2.2 Methane molecule. The four C-H bonds are sp3 hybridized and point to the corners of a tetrahedron. From ref [20]

The four outermost orbitals are hybridized to form four equivalent sp^3 orbitals resulting in a tetrahedral structure. In a molecule like ethylene, the bonds are sp^2 hybridized, resulting in three sp^2 bonds and one π bond formed by the p_z orbital, per carbon atom. The three sp^2 bonds are in the plane of the molecule at approximately 120° to each other and are called σ bonds. And the p_z orbital is perpendicular to the plane of the molecule, forming a bond above and below the plane. See **Figure 2.3**.

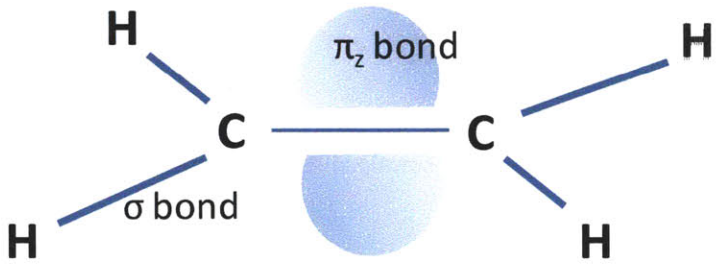

Figure 2.3 Ethylene molecule

In a structure like benzene, the C atoms are sp^2 hybridized forming three σ bonds, with the p_z orbital from each atom being delocalized above and below the plane of the molecule as illustrated in **Figure 2.4**. These bonds are called conjugated bonds.

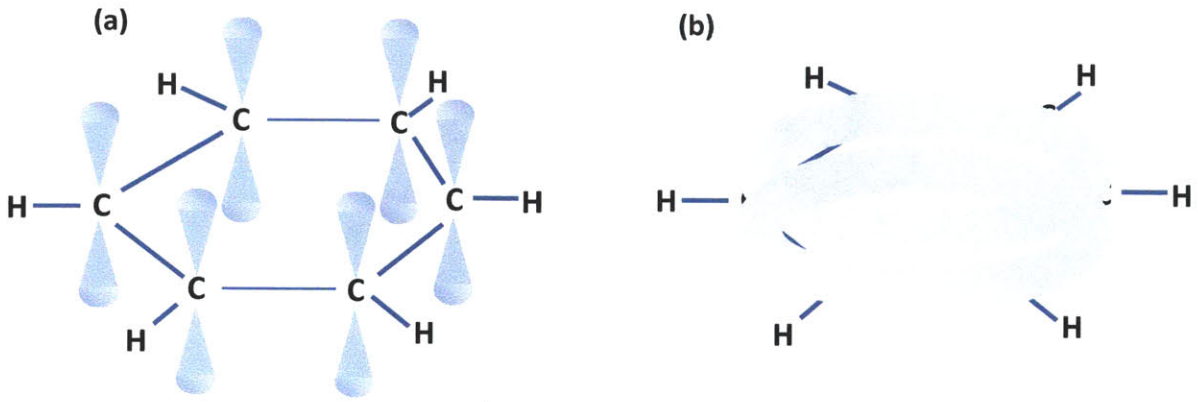

Figure 2.4 Benzene molecule (a)The p_z orbitals of each carbon atom has one unpaired electron (b) They result in a delocalized electron cloud above and below the plane of the molecule.

The overlap of the conjugated bonds in neighboring benzene-like molecules in a crystal makes for better charge and exciton transport along the directions of overlap. For example in tetracene, shown in **Figure 2.5**, the edge to face orientation of two adjacent molecules in the **ab** plane allows π orbital overlap.

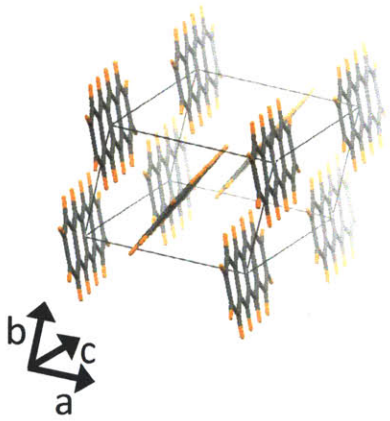

Figure 2.5 Tetracene crystal – herringbone crystal structure

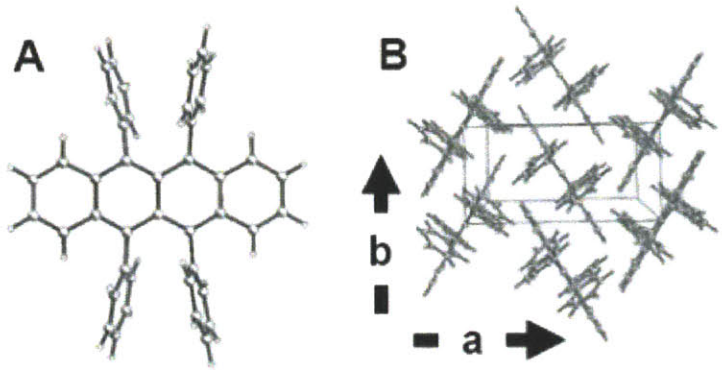

Figure 2.6 (A) Structure of rubrene molecule (B) Herringbone crystal structure of rubrene. From ref [17]

Rubrene has the same herringbone structure as tetracene and charge transport measurements in the ab plane have shown that mobility along the b-axis at 15.4cm^2/Vs is much higher than along the a-axis at 4.4cm^2/Vs due to much better π orbital overlap in the b direction. [17]

This same conjugation is also seen in polymers like regioregular poly(3-hexylthiophene) (P3HT) shown in **Figure 2.7**. P3HT stacks in planes with the conjugated backbone overlap between chains in the bb stacking direction. And in a configuration where the polymer chains are 100% regioregular (part (a)), the bb interplanar separation in the bb direction is less than one with 90% regioregularity (part (b)). This has been shown to lead to improved charge transport. The bandgap is also lowered due to a more delocalized exciton which results in greater absorption in the longer wavelengths .[21]

Other interesting properties of organic semiconductors arise from the pi-conjugated bonds in the molecules. These bonds are the frontier or outermost orbitals and are the ones involved in most of the photophysics involved in organic semiconductor LEDs (OLED), and photovoltaics. The separation of the outermost energy levels in these π-conjugated molecules, is in the visible region of the electromagnetic spectrum which makes them useful in these applications.

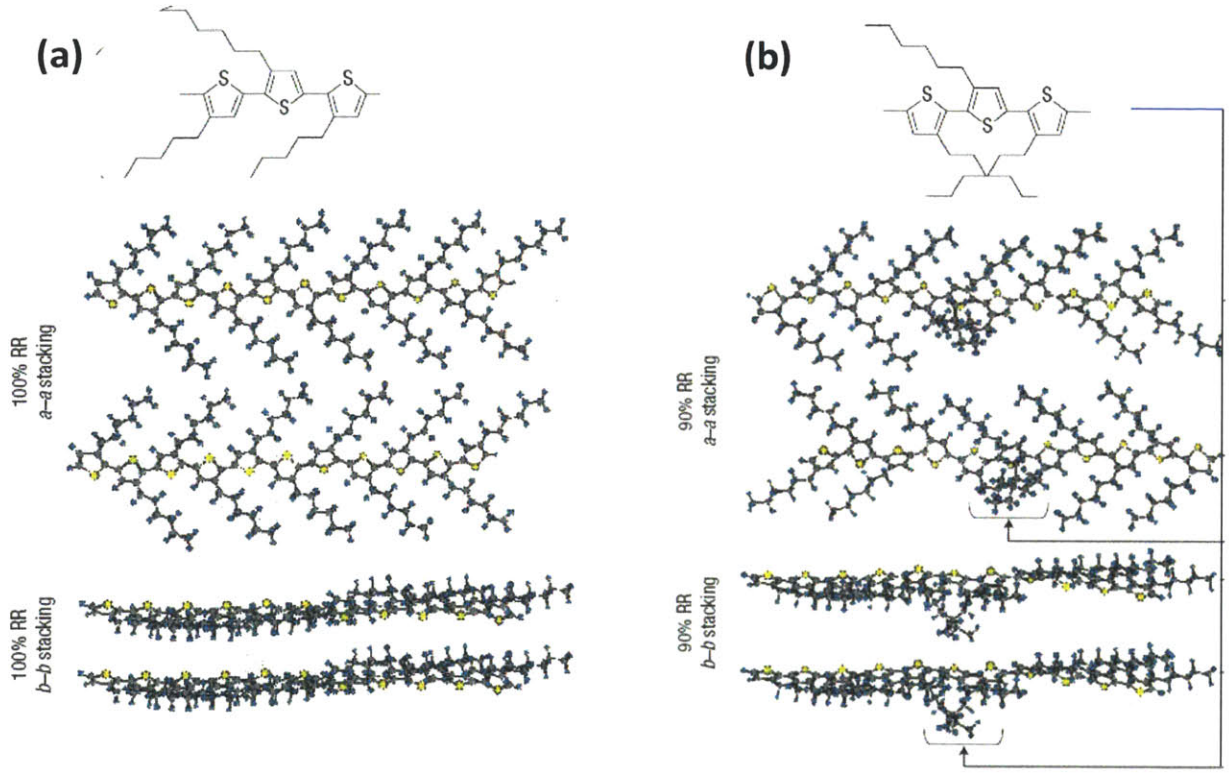

Figure 2.7 Stacking in in regioregular poly(3-hexylthiophene) (**a**) 100% regioregularity configuration and stacking of the molecules in the aa or intraplanar direction and the bb or interplanar direction. (**b**) Same for a 90% regioregularity configuration. From ref [21].

2.2 Charge Transport

The weak van der Waal's forces leads to narrow electronic bandwidth and unlike covalently bonded crystals there is no band transport,. Charge transport takes place by thermally assisted hopping and charge carrier mobilities are generally low: from $3x10^{-6}$ cm^2/Vs in tris(8-hydroxyquinolinato) aluminium (AlQ_3) which forms very amorphous thin films, to 15 cm^2/Vs in rubrene crystal.[16, 17] In comparison doped silicon has a mobility in the order of $10^3 cm^2/Vs$. Organic semiconductors can exist in crystalline as well as disordered forms.

2.2.1 Band Transport

In very pure crystalline solids band transport has been observed. But the purity of the crystal is a strong determinant of the transport properties. The presence of lattice defects and impurities can lead to the transport appear as thermally activated hopping at macroscopic dimensions. **Figure 2.8** shows the

mobilities measured in ultrapure Naphthalene.[22] The mobilities were measured using the time-of-flight method where one end of the sample is radiated with a short pulse of light to generate photocurrent. A constant electric field is applied across the sample and the point where the current drops to zero signifies the charge carriers have reached the electrode and can be used to calculate the mobility. Very high mobilities were observed. The naphthalene sample in **Figure 2.8** shows a $\mu \sim T^n$ trend where $n < 0$ which indicates band transport. At very low temperatures the mobility is electric field dependent with lower fields showing higher mobility.

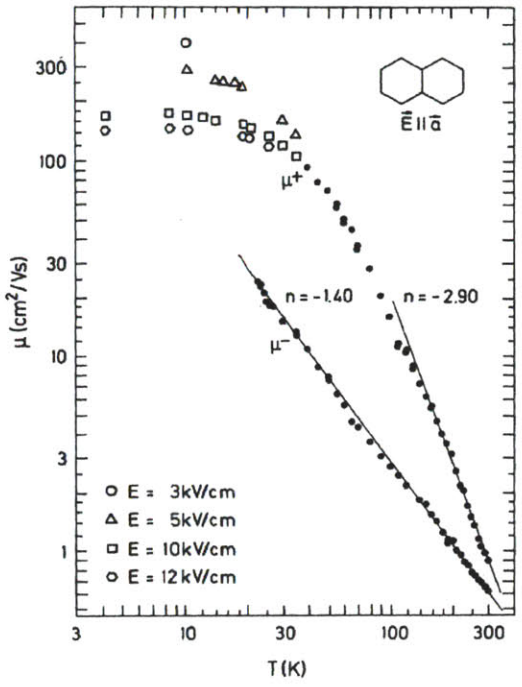

Figure 2.8 Hole and electron mobilities in ultrapure Naphthalene. From ref [22].

2.2.2 Thermally activated transport

Thermally activated transport shows a a $\mu \sim \exp(-E_a/kT)$ trend and is observed when the crystals are of lesser purity or in more amorphous films. Transport takes place by charge carriers hopping from one molecular site to a neighboring one by tunneling. In amorphous films, the physical disorder results in every molecule being surrounded by a different environment and hence resulting in variability in the energy sites of the molecules. The lack of order results in no bands, and instead, there exist localized states with a distribution of energies which is usually assumed to be Gaussian or exponential. It has been measured to be exponential in CuPC with a characteristic energy of 110meV.[23]

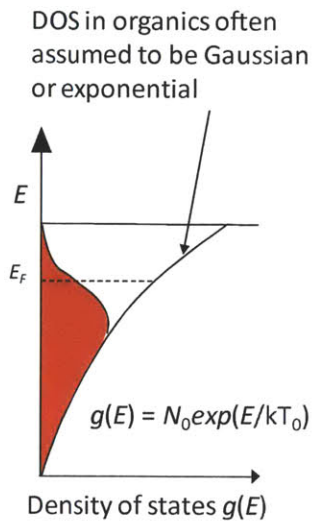

Figure 2.9 The Density of states in an amorphous film shown as exponential in this figure

In addition to being thermally-activated, charge transport in organic semiconductors is also electric field aided. Several groups have proposed an effective temperature with various expressions. A few of which are given below.

Marianer, *et al.* [24] and Baranovskii, *et al.* [25] both ran Monte Carlo simulations considering electrons hopping through an exponential density of states. The resulting electron distribution is a Fermi distribution characterized by an effective temperature of the form:

$$T_{eff}^{n} = T^{n} + \left(\beta T_F\right)^{n}$$

Limeketkai et al [26] proposed a linear expression where the effective temperature is a perturbation of the temperature at low fields:

$$T_{eff} = T + T_f$$

Where $T_f = \frac{qF}{2\alpha k}$ q = electronic charge, α = tunneling length, k = Boltzmann constant, F = Electric field. Limketkai et al use a percolation model of field dependent conductivity starting with the Miller-Abrahams rate model for phonon-assisted tunneling where the hopping rate R_{da} from a site with energy E_d to a site with energy E_a at a distance r_{da} apart is described by:[27]

$$R_{da} = \begin{cases} \nu_0 \exp(-2ar_{da}) \exp\left((E_a - E_d)/kT\right), & E_a - E_d > 0 \\ \nu_0 \exp(-2ar_{da}), & E_a - E_d \leq 0 \end{cases},$$

where ν_0 is the attempt to hop frequency dependent on the phonon density of states and intermolecular overlap. It is important to note that the temperature specified in the Miller Abrahams rates is the temperature of the electron distribution not the lattice temperature. [28] The expression for conductivity derived from the above approach is:

$$\sigma = \frac{\sigma_0}{q}\left[\frac{\pi}{B_C}\frac{T_0^3}{(2\alpha)^3}\frac{16T_{eff}}{(2T_{eff}-T_F)^2(2T_{eff}+T_F)^2}\right]^{T_0/T_{eff}} n^{T_0/T_{eff}}$$

Where n = charge carrier density, σ_0 is a prefactor; B_c = critical bond number, 2.8 in an amorphous three-dimensional system. [29]

2.3 Disorder

The main applications of organic semiconductors - OLEDs and photovoltaics - are thin film devices about 50-100nm thick which are mostly amorphous but may have some degree of crystallinity depending on the material. The disorder results in most effects being localized in these materials and hence impurities and defects can be tolerated. This makes them cheap and easy to use in large area applications. In contrast, inorganic materials are very expensive in large area applications. Roll-to-roll printing and inkjet printing are being researched as inexpensive manufacturing technologies for organic semiconductors.

2.4 Main Applications

The earliest application of organic semiconductors is in xerography where it has been used since IBM introduced it in the 1970s. Organic Light Emitting Diodes (OLEDs) are another important application of organic semiconductors in use today. OLED displays are widely used in many small screen applications like cell phones and mp3 players. Samsung is one of the prominent manufacturers. Large area diffuse lighting is also projected as an important application for OLEDs. Cheap and flexible electronics drive research in Organic Field Effect Transistors (OFET)[30]. While these devices generally exhibit much lower mobilities (.01-1 cm^2/Vs), compared to silicon transistors, there is room in niche applications like flexible displays and RFID tags. OFETs are being researched for applications in sensors[31, 32].

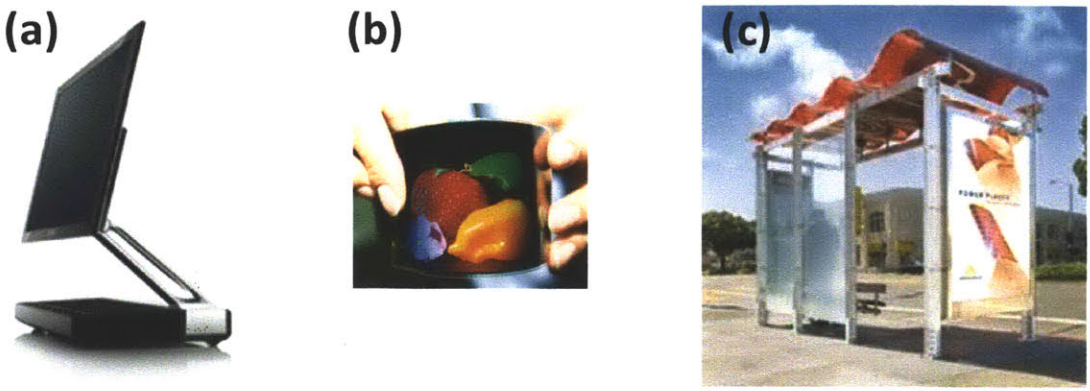

Figure 2.10 (**a**) A Sony OLED TV, 2009, had a 3mm thinness and a 1000,000:1 brightness contrast ratio (**b**) Flexible AMOLED, Samsung, 2010 (**c**) Konarka organic semiconductor photovoltaics on the roof of a bus stop

The wide variety of organic semiconductor materials available with their distinct properties, make them good candidates for sensing applications[33]. Organic semiconductor photovoltaics are still niche products providing attractive colorful and flexible low efficiency cells,[12] but the promise of cheap manufacturing and a versatile library of materials which can keep growing

2.5 Excitons

When light is incident on a material, a molecule can absorb a photon and achieve a high energy state. The high energy state of the molecule is an exciton. Before getting into more details about excitons, let us define some terms in the molecular structure of an organic semiconductor molecule.

The energy levels of a molecule are called orbitals and just like atomic orbitals, one molecular orbital can hold two electrons. The Highest Occupied Molecular Orbital is referred to by its acronym as HOMO, and similarly the Lowest Unoccupied Molecular Orbital as LUMO. These are the only orbitals involved in most of the important transitions and processes, including absorption and emission of light in the visible and near IR region, and in the photovoltaic process.

When an incident photon is absorbed by a molecule, an electron from the HOMO is excited into the LUMO. The empty state left in the HOMO is a called a hole. The hole and excited electron in the LUMO are Coulombically bound, and together form what is called an exciton. The electron and hole move together and are treated as a quasi-particle. **Figure 2.11** shows the evolution of a molecule in the

ground state absorbing a photon and becoming an exciton. The second illustration of the exciton show the hole as an unfilled circle and the electron as a filled circle and also highlights the fact that the energy of the exciton is lower than the energy difference between the LUMO and HOMO because of the binding energy due to the Coulombic attraction between the hole and electron.

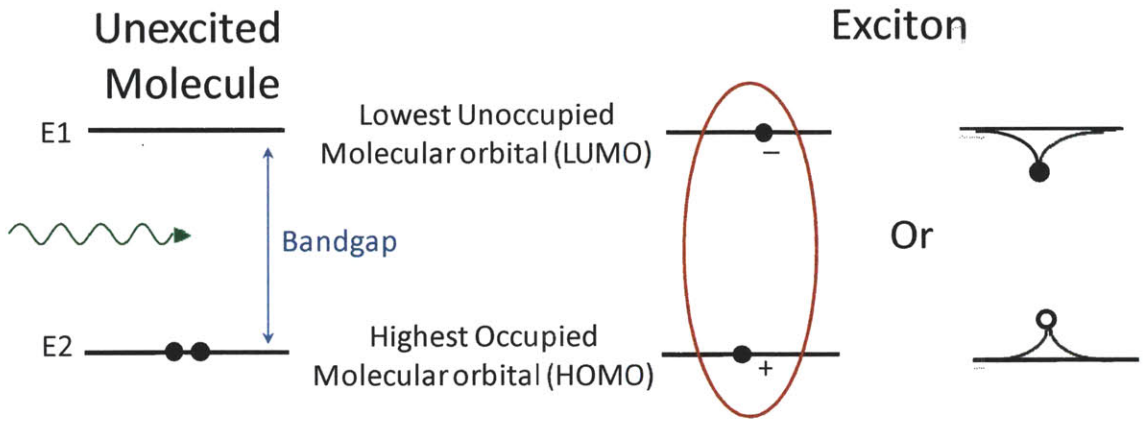

Figure 2.11 A molecule in the ground state absorbs a photon and becomes an exciton

In OLEDs excitons are generated by injection of charge carriers into a material. So an electron can hop onto the LUMO of a molecule, and a hole onto the HOMO of the same molecule thereby generating an exciton.

2.5.1 Wannier and Frenkel excitons

The tightly bound excitons formed in organic semiconductors are called Frenkel excitons. They have binding energies of the order of 1eV. In comparison, excitons formed in most inorganic semiconductors are loosely bound with binding energies of the order of (1-2) kT. These excitons electron and hole can be separated by several lattice constants are called Mott Wannier excitons. The low binding energy can be attributed to the high dielectric constant in inorganic semiconductors: ε_r ~15-20, compared to ε_r ~2-4 in organic semiconductors.

2.5.2 Singlets and Triplets

The excitons in organic semiconductors have one other important categorization based on spin. Singlet excitons, where the spin state of the electron pair is antisymmetric with particle exchange, have spin S =

0, and triplet excitons where the spin state is symmetric with particle exchange have spin S = 1. See Figure 2.12.

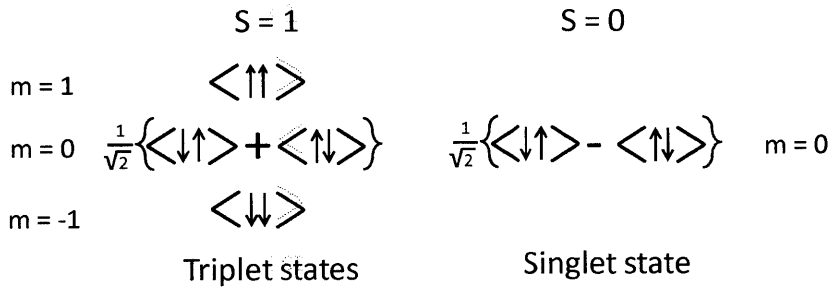

Figure 2.12 The triplet exciton can has three possible states and the singlet exciton has one state. S is the total spin, and m is the z component.

Electrons have spin 1/2. According to Pauli's exclusion principle no two identical Fermion's (particles with half-integer spin) can occupy the same state which implies that two identical electrons should be anti-symmetric under exchange. Since a singlet has an antisymmetric spin state, it must be spatially symmetric, and vice versa for the triplet. Spatial symmetry brings the two electrons closer leading to a bonding orbital for a singlet. See **Figure 2.13**. The triplet on the other hand forms a spatially antisymmetric state which pushes the electrons further apart leading to an antibonding orbital which would result in breaking up the molecular bond. Hence the ground state can only be a singlet.

But if we consider the excited states, with one electron in the HOMO and the other electron in the LUMO or higher state, they *can* exist as singlets or triplets. The combination of spin and spatial symmetry still brings the electrons in the singlet closer together and pushes the electrons in the triplet further apart. The lower Coulombic repulsion results in the triplet state being more stable than the singlet and lower in energy [34].

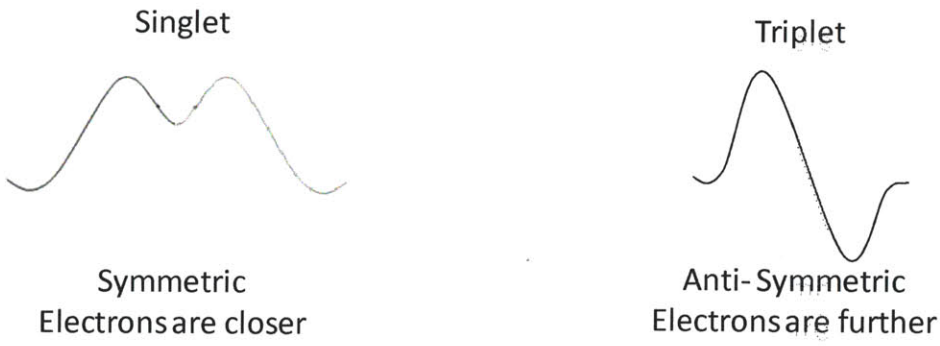

Figure 2.13 Electron distribution functions in triplets and singlets

3 Organic Semiconductor Photovoltaics

This chapter discusses the basic physics of the workings of an Organic Semiconductor Photovoltaic (OPV), the main types of OPVs, and other OPV considerations like cost and built-in losses.

3.1 Basic Organic Semiconductor Photovoltaic (OPV) operation

An OPV is generally made of disordered organic semiconductor materials. The Highest Occupied Molecular Orbitals (HOMO) and the Lowest Unoccupied Molecular Orbitals (LUMO) are the only ones involved in the photovoltaic process. In the simplest OPV structure with two active materials, the HOMO and LUMO of the constituent materials have to be offset in a Type II heterojunction as shown in Figure 3.1. One of the materials is termed the donor and the other the acceptor. The donor-acceptor terminology will be made clear in the following section where the photovoltaic action is described in detail.

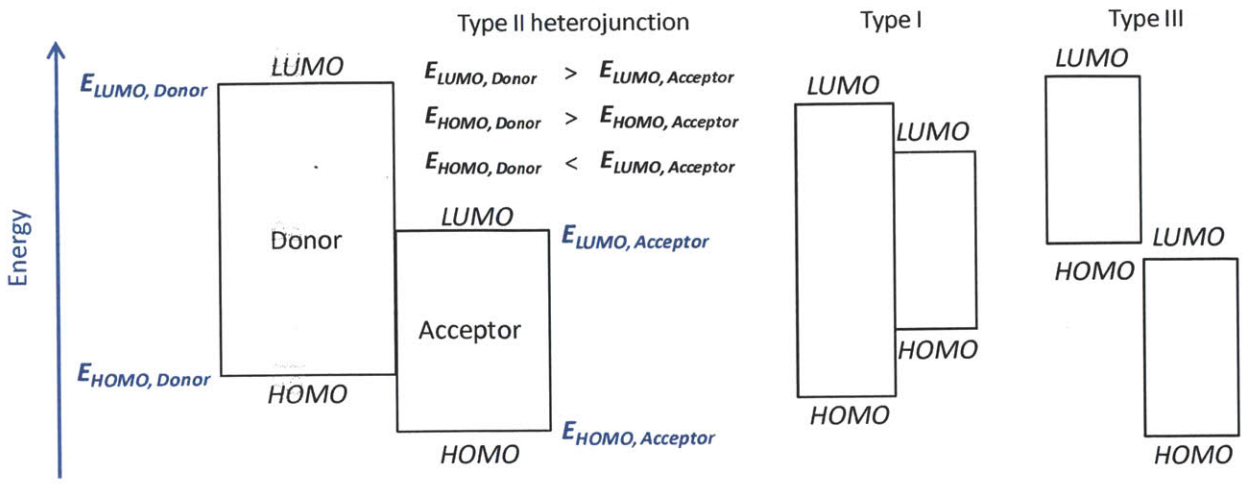

Figure 3.1 Energy levels in the Type II heterojunction, as required in an OPV operation. Types I and III are also shown for reference

In the simplest OPV structure you have the donor and acceptor materials sandwiched between a cathode and an anode in a vertical structure. Figure 3.2 (a) shows a physical picture of an OPV. The substrate is usually glass. The white layer shown in the figure is usually a transparent conducting oxide layer through which solar radiation is incident on the device. We use Indium tin oxide (ITO) in our devices. The brown layer can be considered as the active organic layers. The grey layer on top represents the metal cathode, and there is a glass encapsulating layer on top to protect the device from moisture and oxygen.

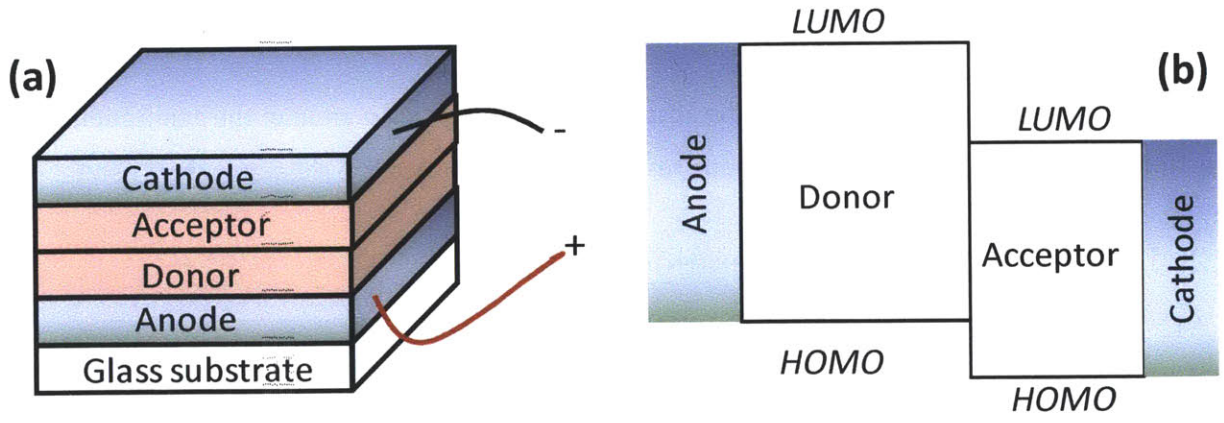

Figure 3.2 (a) A physical schematic of an OPV (b) Energy level diagram and layers in an OPV

Figure 3.3 shows the steps in the photovoltaic action of an OPV. 1) An incoming photon is absorbed by the device, 2) creating an exciton (a bound electron-hole pair) in one of the molecules. In the figure it's a donor molecule, but it could be the acceptor too. 3) The exciton can diffuse to the interface and be split into a charge transfer (CT) state. The CT state is a type of an exciton, with the electron on an acceptor molecule and the hole on a donor molecule. The hop from an exciton to a CT state has to be energetically favorable, $E_{CT} < E_{exciton}$. 4) The CT state can split into an electron and hole which can then diffuse to the cathode and anode respectively, generating current in the external circuit. The terminology of the donor and acceptor is now clear – the donor donates an electron and the acceptor accepts one. The energy o fthe CT state $E_{CT} \sim V_{OC}$ the open circuit voltage of the device.

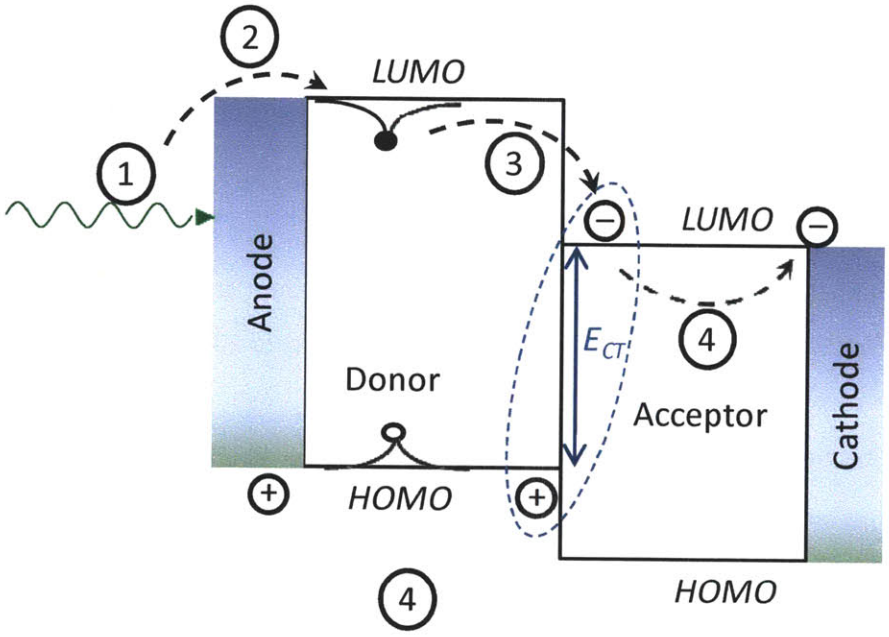

Figure 3.3. Process steps in an OPV from the absorption of an incoming photon to the generation of an electron and a hole in the cathode and anode respectively. The dashed line illustrates the CT state.

3.2 Limiting Issues in OPV operation

3.2.1 Loss due to binding energy

One of the limiting factors in OPVs arises due to the binding energy of excitons. Inorganic semiconductors silicon have high dielectric constants, for example in silicon $\varepsilon = 12$, and so the excited state formed by photon absorption immediately separates into independent charges. In comparison, organic semiconductor materials have low dielectric constants ~3 and hence the generated excitons

have high binding energies of 0.4-1.4eV.[35] The driving force required to dissociate the generated exciton into a CT state is provided by the difference between the optically generated exciton and the CT state formed at the interface. It is found that photoinduced electron transfer can occur when E_g-eV_{CT} > 0.1eV.[36] The greater loss occurs from the CT state energy to the output voltage. For organic bulk heterojunction cells E_{CT} - V_{OC} > 0.5V. The minimal loss from optical absorption to output voltage is estimated as E_g-eV_{OC} =0 .6eV.

3.2.2 Diffusion length of excitons

The diffusion length of excitons is a trade-off with the absorption in organic materials. **Figure 3.4** shows the absorption profile, and exciton diffusion in a bilayer OPV. A thick layer organic is layer is desired to maximize absorption, but then the maximum number of excitons are formed furthest from the interface and a short exciton diffusion length will prevent excitons from reaching the interface. Exciton diffusion lengths of organic semiconductor materials are usually ~10nm. 3,4,9,10-perylenetetracarboxylic bis-benzimidazole (PTCBI) has a diffusion length of 3nm and copper phthalocyanine (CuPC) 8nm. [37]Some are larger, for example C_{60} has a diffusion length of 40nm, and tetracene thin film which makes a polycrystalline film has a diffusion length of 100nm. [37, 38] A typical absorption coefficient is $1x10^{-5}/cm^{-1}$. Hence a thickness of 230nm is required for 90% absorption.

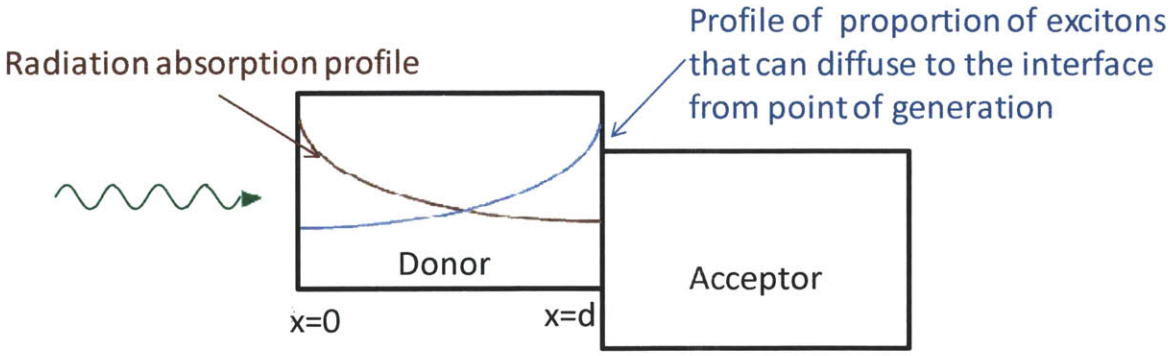

Figure 3.4 Profiles of absorption and exciton diffusion to the interface in a bilayer organic OPV

Triplets generally have longer diffusion lengths than singlets due to the long lifetime of the triplet state in the order of microseconds, compared to singlets which have lifetimes in the order of nanoseconds. Indeed, many of the standard photovoltaic materials in bilayer photovoltaic devices have high intersystem crossing which results in high triplet yield – like C_{60} and CuPC. This intersystem crossing results in an energy loss because the exchange interaction energy is of the order of 1eV. Also, triplets

diffuse by Dexter transfer, in which each hop is only to the nearest neighbor or next nearest neighbor. Singlets diffuse by long range Forster transport by non-radiative dipole coupling, each hop is 4-5nm away. So it is not always the case that triplets have longer diffusion lengths.

One way to get around this trade-off is nanostructured interfaces, which is the solution used in bulk heterojunction cells.

3.3 OPV Model

The equivalent circuit model of an OPV is shown in **Figure 3.5** and is the same as for a solar cell with a pn junction.

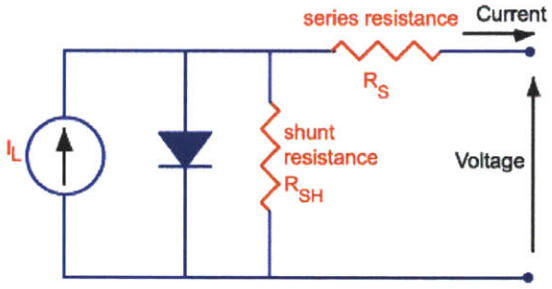

Figure 3.5 Equivalent circuit model of an OPV

The current-voltage characteristics can be modeled by the Shockley equation:[39]

$$J = \frac{R_p}{R_s + R_p}\left\{J_s\left[exp\left(\frac{q(V - JR_s)}{nk_BT}\right) - 1\right] + \frac{V}{R_p}\right\} - J_{ph}(V)$$

Where the reverse saturation current: $J_s = J_{s0}exp\left(-\frac{E_g}{2nk_BT}\right)$

n is the ideality factor and E_g is the CT state energy

$J_{ph}(V)$ is the photocurrent generated in the device at voltage V: $J_{ph}(V) = \int \frac{q\lambda}{hc}\acute{\eta}_{EQE}(\lambda, V)S(\lambda)d\lambda$

The shunt resistance R_p models recomination losses and is lower when recombination is high at the interface, and the series resistance models mobility of charge carriers in the bulk as well as interface resistances.

3.4 OPV architectures

3.4.1 Planar structure

The structure described in the last section is a basic bilayer planar structure with the acceptor stacked on the donor. The first OPV made by C.W.Tang in 1986 is a bilayer structure comprised of Copper Phthalocyanine (CuPC) as the donor and 3, 4, 9, 10 perylenetetracarboxylic bisbenzimidazole (PTCBI) as the acceptor. [40] The efficiency of this cell was 1%, the open circuit voltage 0.45V and the fill factor was 65%. In such a structure the charges flow to the electrodes by diffusion and the built-in field arising due to the difference in work functions of the electrodes. The thicker the active layers the more the absorption of light, but thickness of the layers is limited by the exciton diffusion length. The open circuit voltage of any OPV is determined by E_{CT}.

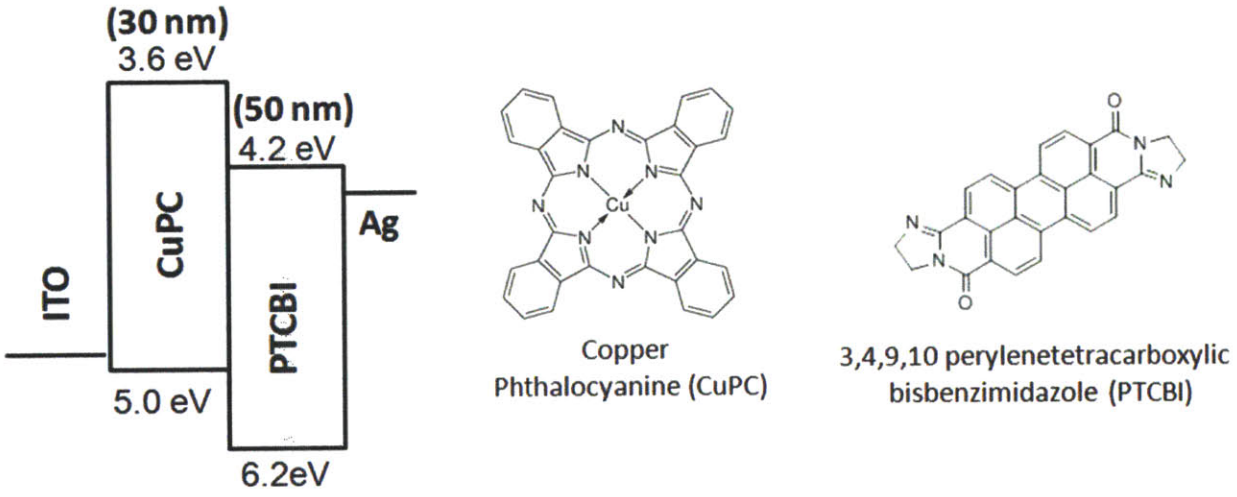

Figure 3.6 Structure of first OPV made by C.W.Tang

3.4.2 Bulk Heterojunction

The planar structure is limited by the exciton diffusion in the active layers. The exciton diffusion lengths of most materials is too short compared to their absorbance. For example CuPC has an exciton diffusion length of 10nm and an absorbance of 50nm at its peak absorption wavelength of 636nm. Hence a thickness of 10nm will only absorb 33% of the incident light (assuming two passes of the incident light

through the thickness of the active layer). Making the active layer too thick will mean that fewer excitons will get to the charge generating interface. A bulk heterostructure gets around this problem by having the donor and acceptor mixed in the bulk of the device, so that every exciton formed is now next to an interface and dissociates into a CT state. See Figure 3.7.

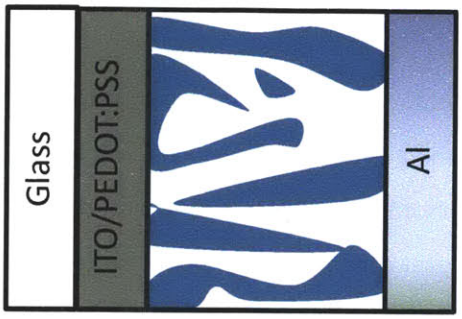

Figure 3.7 This illustration only shows the physical structure of the device, the energy levels are not indicated. Typical anode and cathode are shown the structure. The blue and white swathes in the active layer are representative of the donor and acceptor materias.

Typically bulk heterojunction cells are made by solution processing. [41]The reason that bulk heterojunction cells work is that there is lateral phase separation in the donor acceptor layers and hence there is a path for holes and electrons to flow from the charge generating interface to their respective electrodes. The built-in potential due to the difference in the Fermi levels of the electrodes causes the charge carriers to flow in a certain direction.

3.4.3 Tandem cells

This is a type of a cell where more than one cell is stacked one on top of the other connected in series. This allows a larger thickness for absorption, and sometimes the two cells absorb different parts of the spectrum. The tandem cell, introduced in chapter 1, with regard to triplet junction cells, is a structure that can get around the Shockley-Queisser limit. The problem with a tandem cell is that the two devices need to be current matched for the cell to be effective. Figure 3.8 shows a polymer tandem cell.[42] Since polymer tandem cells are solution processed they have the additional complication that the solvents for the various layers need to be orthogonal.

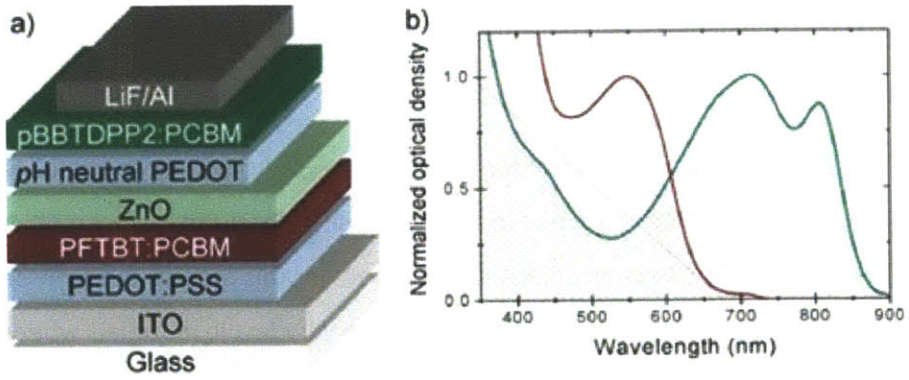

Figure 3.8 **(a)**A tandem cell. The active layers of the two component cells shown in green and red **(b)** The absorption of the two component cells. Figure from reference [42]

3.5 Manufacturing Cost

One of the big potentials of OPVs, is the low cost of production. If printed on flexible substrates like plastic sheets, standard printing processes like roll-to-roll processing should result in cheap manufacturing. Kalowekamo and Baker have done some cost estimates and seen that a 5% efficiency and a 5 year lifetime module time leads to module costs between $1.00 and $2.83/W, and an LCOE between 49¢ and 85¢/kWh.[43]This is far from competitive considering the cost of electricity production from a new coal plant is estimated at 8.3¢/kWh.[44] Assuming 15% efficiency and a 20-year lifetime, Kalowekamo and Baker find an LCOE between 7¢and 13¢/kWh. The highest costs have been associated with a glass substrate and transparent conducting oxide(TCO).

Lifetime is an important factor in LCOE, and is one of the issues of OPVs. Studies done on cells with high performing polymers PVs P3HT and PCDTBT have shown lifetimes of 3.1 and 6.1 years respectively.[45]

The low efficiency of OPVs increases LCOE even with low module cost. But this may not be a drawback for certain niche applications. For example, in third world countries, for areas that do not have access to grid electricity, low module cost is the most important factor for lighting purposes. A study done under "Lighting Africa", a World Bank initiative, manufactured, and field tested polymer solar cells integrated with white LEDs and a Lithium ion battery in Zambia.[46] The cost was estimated to have the potential to come down to 7€ compared to the typical lighting cost of 3€ in the same conditions.

4 Singlet fission in organic semiconductor photovoltaics

4.1 Singlet fission

In some organic semiconductors, a singlet exciton can spontaneously split into two lower energy triplet excitons. See Figure 4.1. The energy contained in a singlet exciton localized on one molecule gets split into the energy of two triplet excitons on adjacent molecules. For this process to be possible, $E_s > 2*E_t$ should be satisfied. This process is spin-conserved and hence very fast in materials where the energy requirement is satisfied.

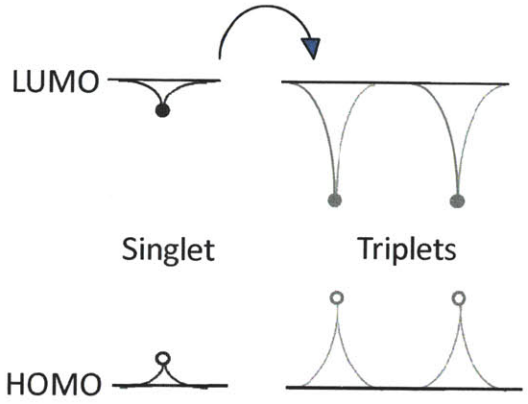

Figure 4.1 Singlet fission: a singlet on one molecule splits into two triplets on two adjacent molecules. To differentiate the two species, triplets will be shown in gray and singlets in black.

Singlet fission has been studied extensively in tetracene[47, 48] and pentacene[49, 50] in the 1970s. It has mainly been observed in these two acenes and their derivatives (see Figure 4.2).

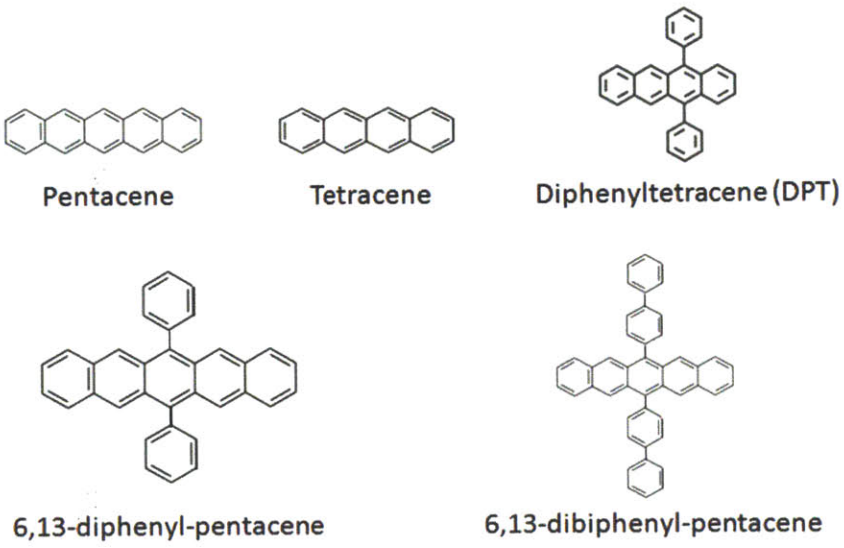

Figure 4.2 Some materials that exhibit singlet fission

Indeed this phenomenon is of much interest to the community because multiple exciton generation can be used to get around the Shockley-Queisser limit.

4.2 Shockley-Queisser limit

The Shockley-Queisser limit says that the efficiency of a single junction solar cell can never be more than a certain theoretical limit.[30] This is because of mainly two types of losses, thermalization and band gap losses, illustrated in Figure 4.3.

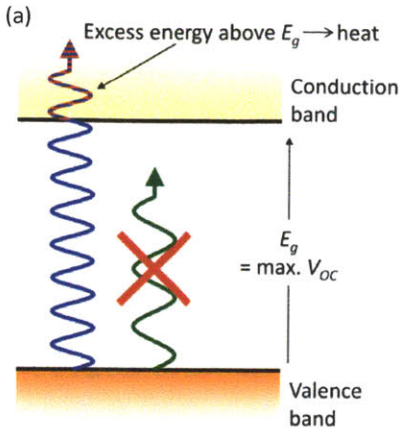

Figure 4.3 A high energy photon (blue) excites an electron much above the band gap, that electron then thermalizes to the band gap losing the energy to the phonon bath of the material. A low energy photon (green), because it has energy below the band gap, is not absorbed.

While the band gap and thermalization losses limit the efficiency to 48%, additional losses stem from blackbody radiation and recombination. The Shockley-Queisser limit considers a detailed balance limit, wherein required radiative losses are the only recombination losses and predicts the maximum efficiency of 33.7% at a band gap of 1.34eV.[51]

Besides singlet fission some other schemes have been devised or proposed to get around this limit. The most important one is tandem cells which we describe in the next section. There are others like multiexciton generation in quantum dots, also discussed below, hot carrier collection, and impurity photovoltaic effect. [52, 53] [54, 55]

4.3 Tandem Cells

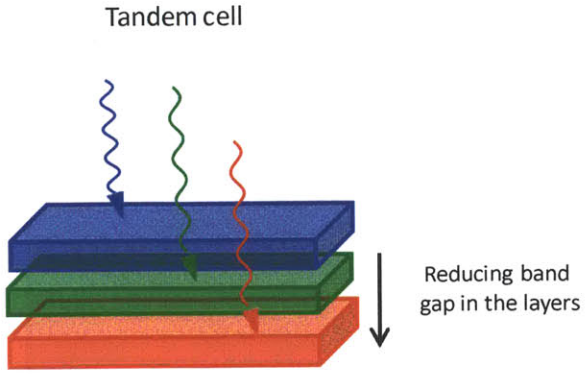

Figure 4.4 Tandem cells can get around this limit but need to be current matched and can be expensive to fabricate in some material systems.

A multiple-junction solar cells is effectively made up of several single-junction cells stacked up one on top of each other as shown in Figure 4.4. The topmost cell has a high band gap energy and absorbs only the highest energy photons and effectively outputs a high voltage. The next cell has a slightly lower band gap and absorbs the next highest set of photons, and so on. The output voltage of the complete cell is the sum of the voltages of each single junction cell. In this way thermalization as well as band gap losses are minimized.

For example in a lattice-matched GaInP/GaInAs/Ge cell, the band gaps are GaInP:1.9eV (653nm), GaInAs:1.4eV(886nm), Ge: .67eV (1850nm). See **Figure 4.5**. The cell has an efficiency of 43.6% certified by NREL. The drawback of inorganic tandem cells is that they are expensive to manufacture and in general, the cells need to be current matched in any material system, including in OPVs.

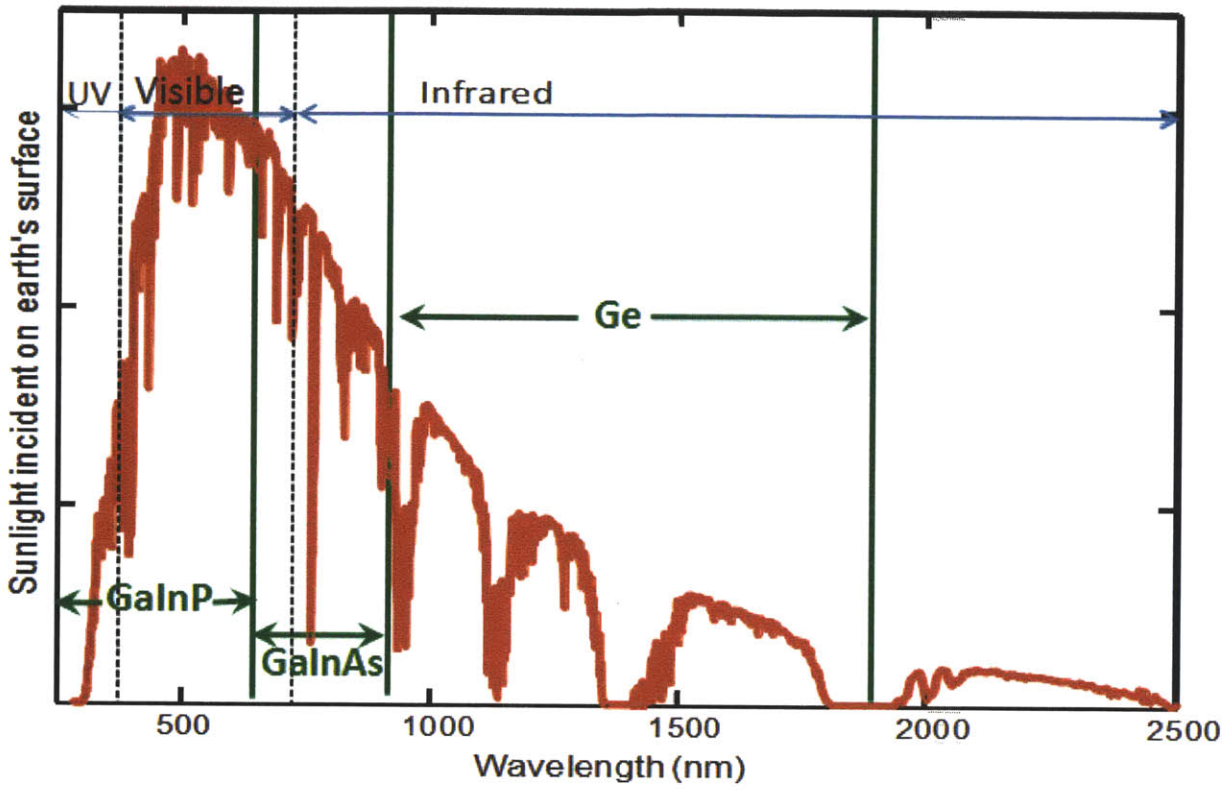

Figure 4.5 Parts of the solar spectrum being absorbed by the three junctions in the GaInP/GaInAs/Ge tandem solar cell

In organic photovoltaics, where solution processed devices are the cheap alternative, tandem cells would require the use of orthogonal solvents for each layer, which adds to the complexity of the structure.

4.4 Multiple Exciton Generation in Quantum Dots

Impact ionization in bulk semiconductors results in more than one e-h pair when the absorbed photon is many multiples the energy of the bandgap. The phenomenon, called multiple exciton generation (MEG) in quantum dots, is much more efficient because the discretization of the energy levels results in slowing down the process of thermal relaxation, by of what is termed the phonon bottleneck. MEG was first reported in PbSe dots in 2004 at excitation energies of $3E_g$.[56] There have been a number of reports in other material systems subsequently. There has also been some doubt about the existence in some systems and the high reported efficiency in some. In 2007 Nair and Bawendi reported that they did not observe MEG in CdSe and CdTe QD as reported by others.[57] An Internal Quantum Efficiency, the

number of charge carriers generated per photon absorbed, of greater than one was reported in PbS quantum dots in a photodetector for excitation energies of ~3E_g.[58]

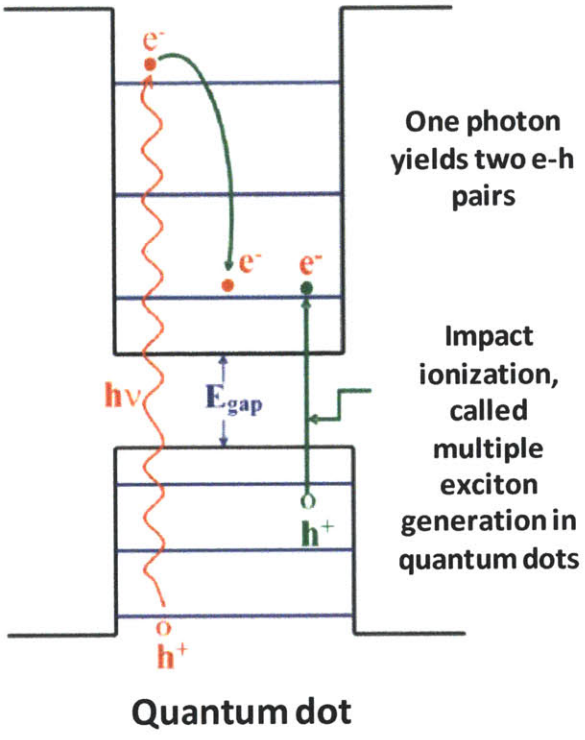

Figure 4.6 Multiple exciton generation in a quantum dot. From ref [59].

4.5 Singlet fission in an OPV

We now see how singlet fission can help the performance of a single junction OPV. **Figure 4.7** (a) shows a bilayer device structure with a large band gap donor that absorbs in the high energy (blue) part of the

spectrum, and a small band gap acceptor that absorbs in the low energy (red) part of the spectrum.

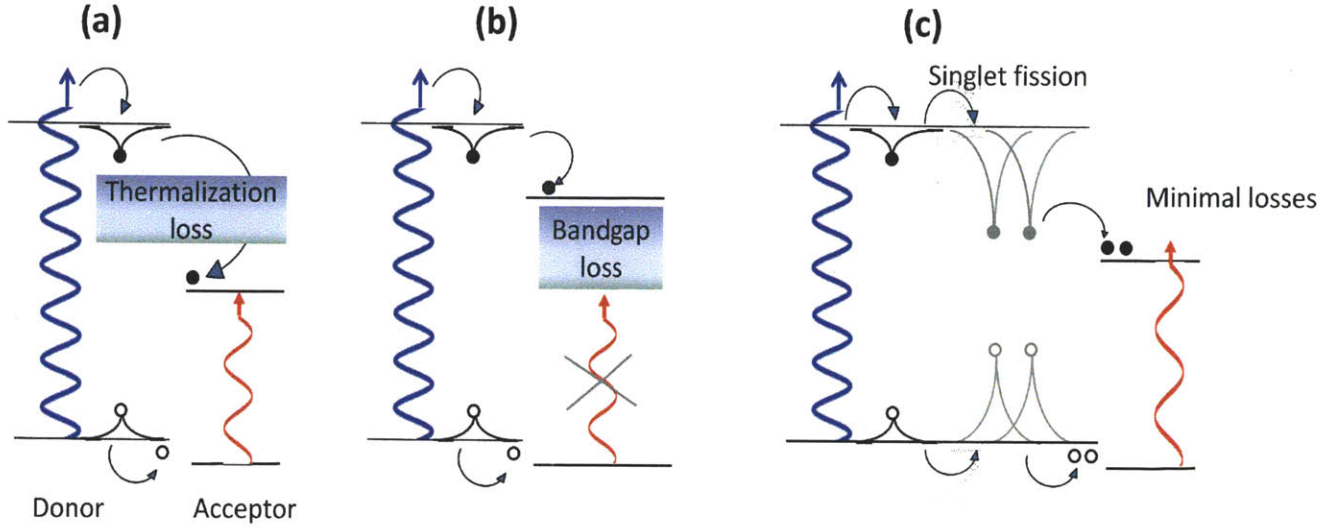

Figure 4.7 How singlet fission is useful in an OPV

The donor absorbs a blue photon generating a high energy exciton which diffuses to the interface and becomes a CT state. The conversion from a high energy exciton to a low energy CT state results in thermalization loss. This loss can be avoided by increasing the LUMO of the acceptor as shown in **Figure 4.7** (b). But this step results in a larger band gap acceptor which means that fewer low energy photons are absorbed than before thereby increasing the band gap loss. This is the tradeoff in a regular single junction solar cell.

Let's go back to the original structure where one of the materials is a low band gap material, and instead introduce a singlet fission material as the large band gap absorber (in this example the donor. In **Figure 4.7**(c) the high energy singlet excitons generated in the donor, split into two lower energy triplet excitons which split into two pairs of CT states and hence two pairs of charge carriers. The thermalization loss in (a) has been converted into an extra pair of charge carriers.

Note that singlet fission is a useful scheme only when a high energy singlet fission material is coupled with a low band gap material. This is because if we look at only the high energy singlet fission material, though we double the current, at the same time we half the voltage, since the voltage is proportional to the energy of the CT state and hence in an indirect way depends on the energy of the excitons. It is only because we couple it with a low band gap material that we also pick up the low energy photons and hence can overcome the Shockley-Queisser limit.

4.6 Theoretical efficiency limits for various schemes

The theoretical efficiency limit using singlet fission increases to 41.9% from 33.7% for the single junction limit as can be seen in the plot below. The efficiency for a multiple exciton generation cell with a multiplication of six energy levels is not much higher at 44.4%.

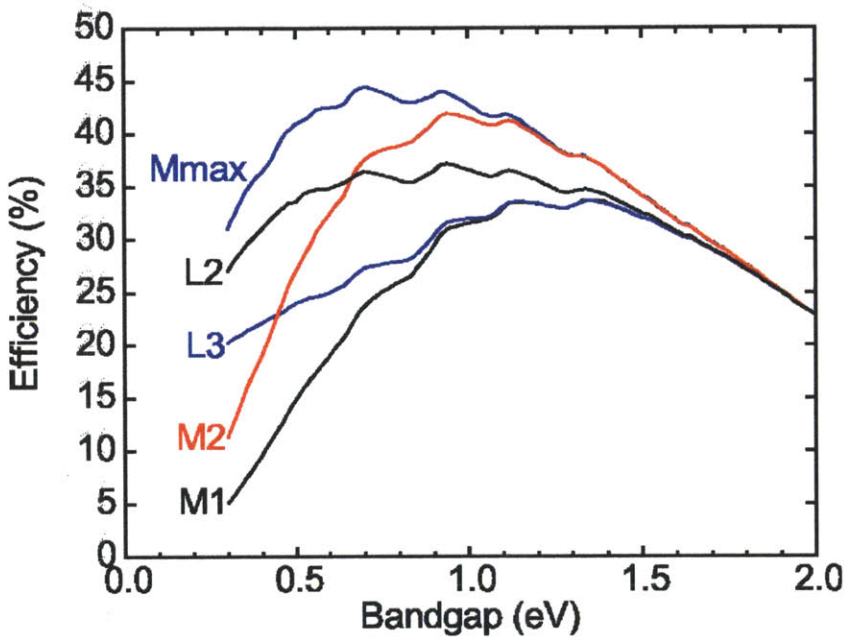

Figure 4.8 Theoretical limiting efficiencies for (i) a single junction cell - M1 (ii) a singlet fission cell - M2 (iii) a tandem cell with 6 energies – Mmax. L2 and L3 are linear absorbers beyond 2*Eg and 3*Eg. From ref [51].

5 Singlet exciton fission

Singlet exciton fission was first observed in tetracene crystals in 1968. Leading up to its discovery was the reverse process, triplet-triplet annihilation (TTA) or triplet fusion, seen in anthracene crystals in 1963.[60]

5.1 Discovery of Singlet Exciton Fission

The lifetime of the singlet state in anthracene as measured by direct excitation is 0.26ns and is at an energy of 3.42eV, see Figure 5.1.[61] Kepler et al in ref [60] saw the same fluorescence spectrum by excitation of triplets at 1.8eV using a laser radiation of 1.79eV using a ruby laser.

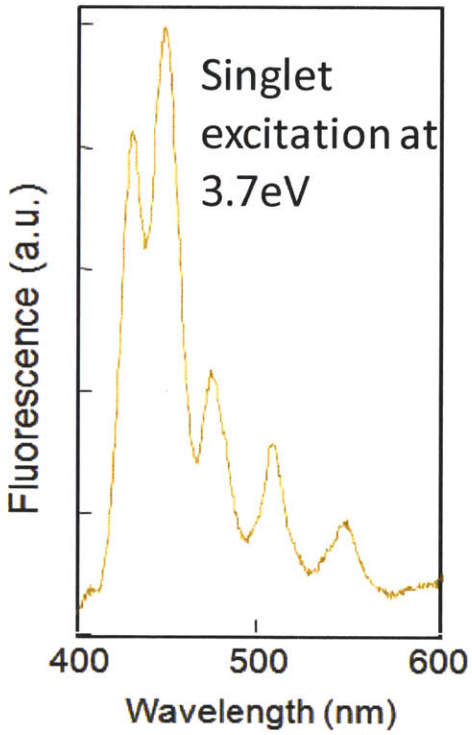

Figure 5.1 Anthracene fluorescence generated by excitation at 3.7eV

F

But the fluorescence had a much longer lifetime in the order of ms. See **Figure 5.2**. They attributed the delayed fluorescence to TTA leading to the generation of a singlet state.

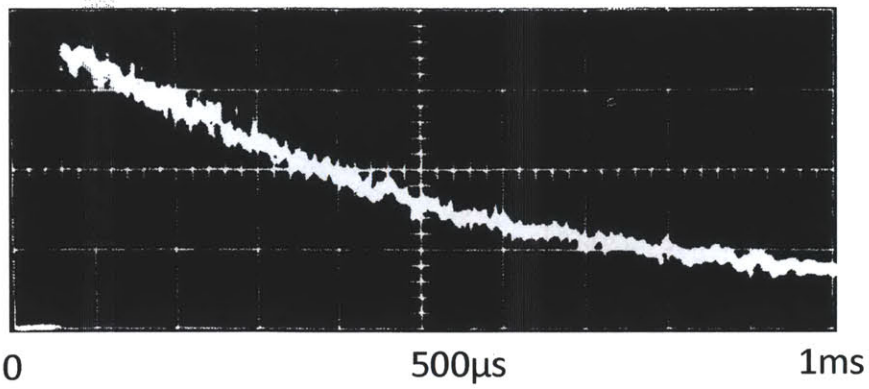

Figure 5.2 Time dependence of the blue anthracene fluorescence by excitation of the triplet at 1.8eV. From Kepler et al. in ref [45]

In 1965 Singh et al suggested that the reverse process of a singlet splitting into two triplets should also be possible.[62] In 1967 Kazzaz and Zahlan observed a very low fluorescence quantum yield of 0.02% in tetracene at room temperature which increased a 100-fold on cooling to 4K, see **Figure 5.3**.[63] In 1968 Swenberg and Stacy proposed the reason for this to be the decay of a singlet into two triplets and also predicted its possible existence in pentacene.[47]

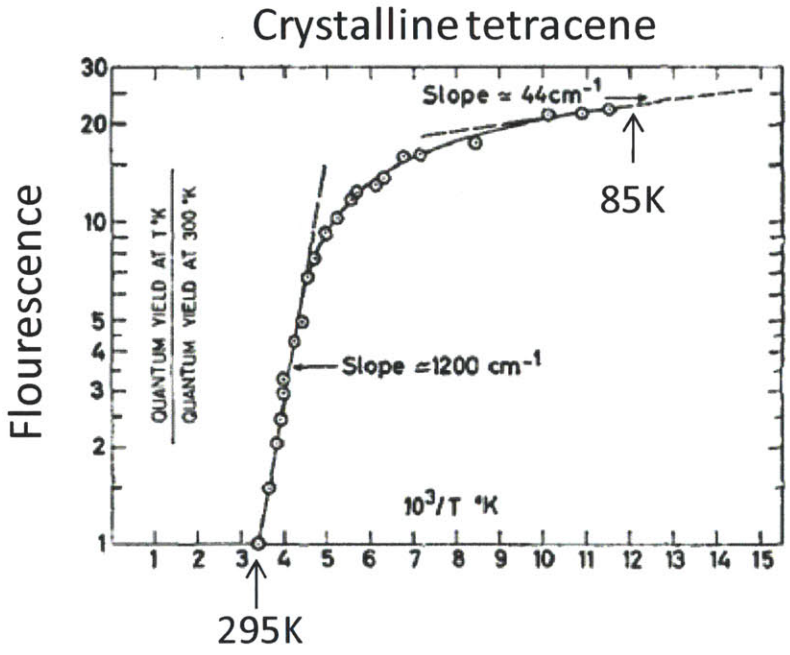

Figure 5.3 Low fluorescence yield in tetracene crystal which rises 20-fold on cooling to 85K. From ref [63].

The similarity of the effect of a magnetic field on both the processes – the delayed fluorescence in anthracene and the prompt fluorescence in tetracene shown in **Figure 5.4** - provided final proof of singlet fission.[48, 64]

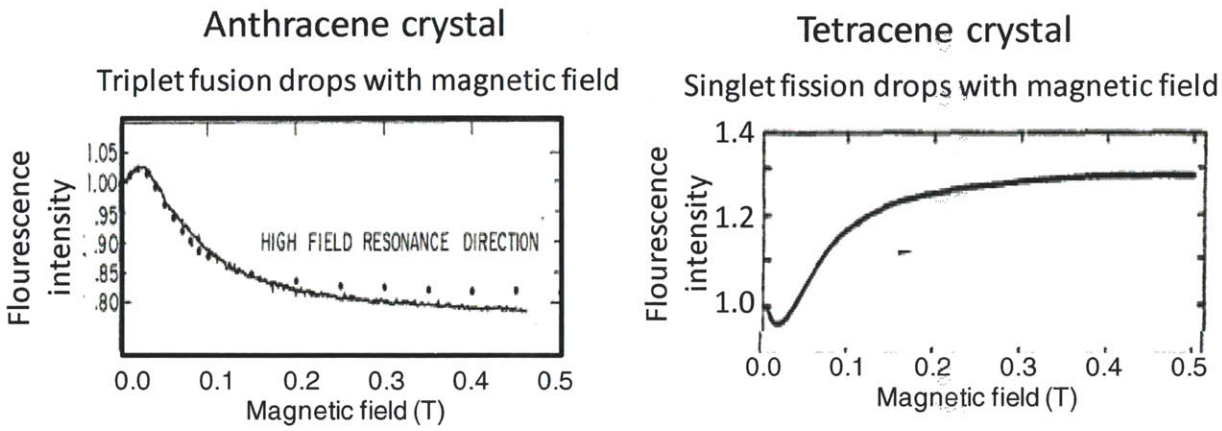

Figure 5.4 Magnetic field effects on anthracene and tetracene from refs [65] and [48] respectively.

While much work has been done on the magnetic field effect of singlet fission, the basic physics of the process is still being investigated. The recent interest in multiexciton generation processes as an offshoot of photovoltaic research has led to renewed interest in singlet fission.

5.2 Materials

A lot of work is begin done to come up with new materials that undergo singlet fission. But the strongest contenders are still the acenes. It seems that the quantity $E_s > 2*E_t$ determines the efficiency of the singlet fission and triplet fusion.

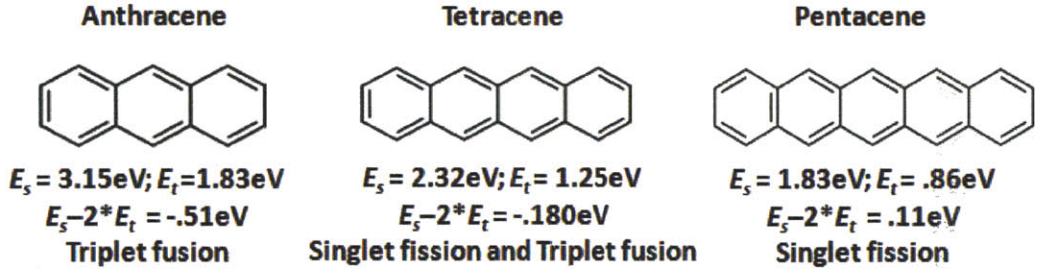

Figure 6.2 Singlet and triplet energies in the three acenes that show TTA and/or singlet fission

In anthracene E_s is much lower than $2*E_t$ and it shows triplet fusion. [66] [60] In tetracene E_s is only a little lower than $2*E_t$ and it shows both singlet fission and triplet fusion, [67] singlet fission being thermally activated. [64] In pentacene E_s is much larger than $2*E_t$ and it shows singlet fission. There is some evidence that singlet fission is possible to a very small extent at very high excitation energies in anthracene.[66] Singlet fission exhibits a rate constant of 100ps in tetracene and 80fs in pentacene.[49, 68] **Figure 5.5** illustrates the timescale at which singlet fission takes place compared to other organic semiconductor processes.

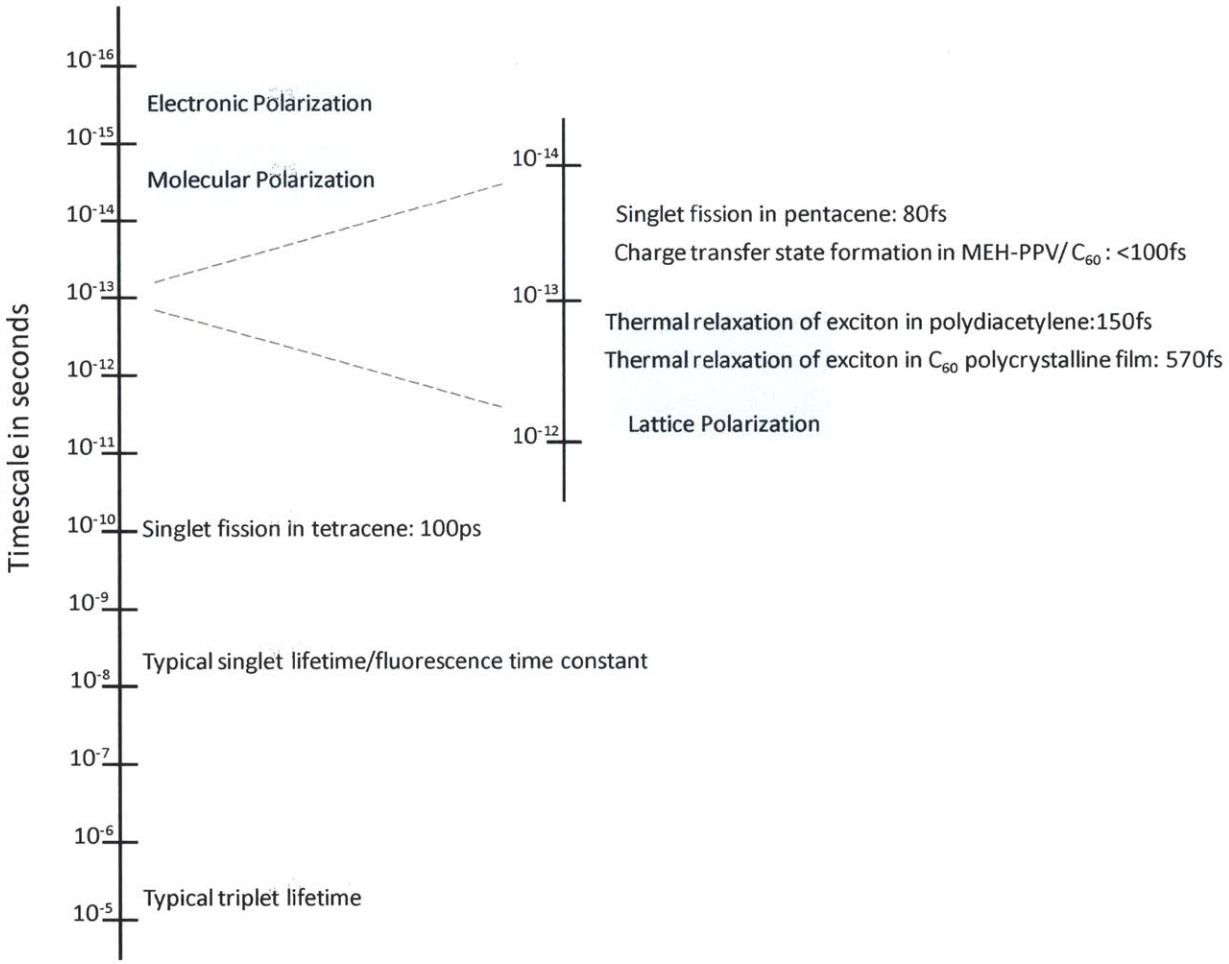

Figure 5.5 Timescales of various processes in organic semiconductors. The polarization numbers are taken from [69]; singlet fission from [49, 68]; thermal relaxations from [70, 71]; Charge transfer formation from [72] .

Some other materials have been identified as displaying singlet fission: carotenoids, polydiacetylene. [73, 74] The search is on to identify more materials.[75] 1,3-Diphenyl isobenzofuran was designed

specifically for singlet fission.[76] But the highest efficiency is still observed in tetracene and pentacene and in their derivatives like rubrene, diphenyl tetracene, diphenyl pentacene, and di-biphenyl pentacene. Some of the structures are shown in **Figure 5.6**.

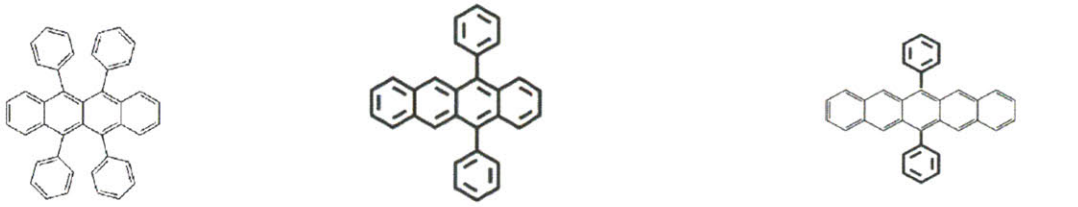

Rubrene **Diphenyl Tetracene** **Diphenyl Pentacene**

Figure 5.6 Acene derivatives that show singlet fission

5.3 Magnetic field effect of singlet fission

Two theories were proposed early on, the simpler one being the Merrifield theory.[77] In its simplest form, the process can be described by a rate equation:

$$S_0 + S_1 \underset{\gamma}{\overset{\gamma'}{\rightleftharpoons}} T_1 + T_1$$

At equilibrium when the rates of the fusion and fission reactions are equal:

$$\gamma'/\gamma = \frac{[T_1]^2}{[S_0][S_1]} = 9\, exp\left(-\left(2E_{T_1} - E_{S_1}\right)/kT\right)$$

where the populations of the two species are described by their Boltzmann distributions. The factor of 9 comes in because 9 triplet pair states are possible since each triplet can have any one of three spin states. It was proposed that an intermediate correlated triplet pair is formed before it splits into two decoherent triplets.

$$S_0 + S_1 \underset{k_2}{\overset{k_{-2}}{\rightleftharpoons}} (TT) \underset{k_1}{\overset{k_{-1}}{\rightleftharpoons}} T_1 + T_1$$

This intermediate state was required to explain the magnetic field effect, which we shall see later.

The Suna theory is more accurate but is also known to be very complex.[78] It does not have an intermediate ^{1}(TT) state, it takes into account exciton diffusion in a crystal, and it fits the magnetic field data better.[79]

The rate of singlet exciton fission is affected by a magnetic field. The rate mostly drops with magnetic field from 0.1T to 0.3T, reaching saturation at around 0.3T. **Figure 5.7** shows the prompt and delayed fluorescence in crystalline tetracene as a function of magnetic field. The prompt fluorescence is inversely proportional to the rate of singlet exciton fission. As can be seen from the figure there is a very small decrease in the rate from 0 to 0.035T, reaching the unchanged rate at 0.05T. Thereafter, the rate keeps increasing until about 0.3T when it saturates.

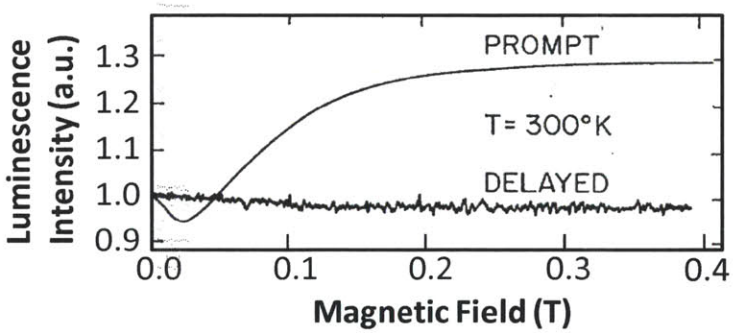

Figure 5.7 Magnetic field effect on prompt and delayed fluorescence in crystalline tetracene. From ref [52].

Extensive work has been done in the 1970s on the magnetic field effect of singlet exciton fission, mostly in tetracene. Singlet fission is observed through delayed and prompt fluorescence. In the above data the tetracene crystal is illuminated with blue light. The generated singlet excitons can either recombine radiatively resulting in prompt fluorescence, or they can undergo the competing process of fission to form triplets. Hence the prompt fluorescence yield is inversely proportional to the rate of singlet fission.

The sample was also illuminated with near infrared light to generate triplets. Triplet-triplet annihilation, the opposite process of singlet exciton fission, resulted in the formation of singlet excitons. These singlets then recombined radiatively, resulting in delayed fluorescence.

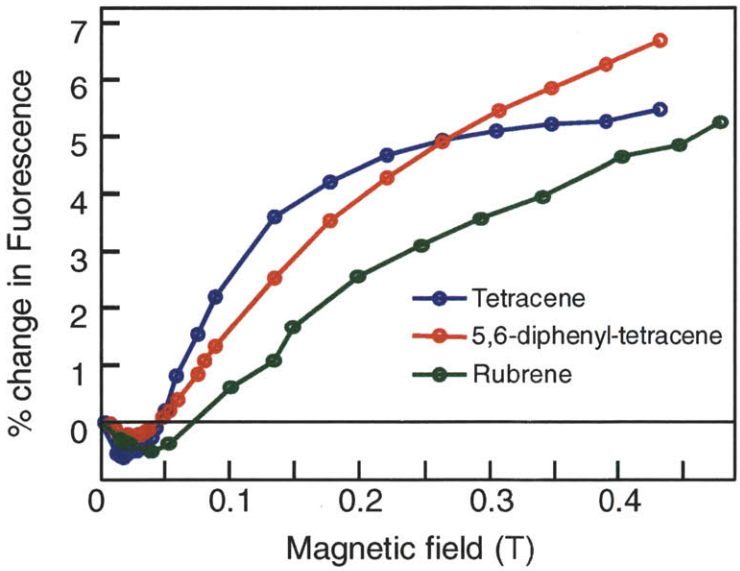

Figure 5.8 Magnetic field effect on fluorescence on tetracene, diphenyl-tetracene and rubrene thin films. The rubrene film was spin-coated from solution, tetracene and DPT were vacuum thermally evaporated.

Figure 5.8 shows steady state fluorescence data from tetracene and its derivatives. In this data the singlet state is generated by the incident radiation. Some of them undergo fluorescence leading to prompt fluorescence, some undergo singlet fission to form triplets. Those triplets in turn undergo fusion leading to delayed fluorescence. The observed steady state fluorescence is the sum of prompt and delayed. The application of a magnetic field changes the rate of the both the fusion and fission reactions similarly, but since the singlets are generated initially and not all triplets generated undergo fusion to resulting in delayed fluorescence, the application of the magnetic field shows the same effect, at least in polarity, as if it were prompt fluorescence.

5.3.1 Physics of the magnetic field effect

A simple way to look at the effect is to consider the Hamiltonian acting on the intermediate ^{1}(TT) state. It can be split into two parts $H_{el} + H_{spin}$. The electrostatic part acts on the nuclear and electronic wave functions and affects the rate of singlet fission as a function of the molecular structure. The basic assumptions of the Merrifield theory are: (i) The overall process is spin conserving (ii) H_{spin} does not commute with the spin operator of the ^{1}(TT) state and hence the spin states are non-stationary (iii) the spin Hamiltonian can be approximated by the zero-field splitting Hamiltonian and the Zeeman interaction that arises from the coupling of the triplet spins with an external field:

$$H_{spin} = g\beta \boldsymbol{H}.\boldsymbol{S} + DS_z^2 + E(S_x^2 - S_y^2)$$

The first term is the Zeeman term and the other two parts are the zero-field splitting or the fine structure term arising from the magnetic field of dipoles of the unpaired electrons in the triplet state. At zero field the fine structure term lifts the degeneracy of the triplet states. The zero-field eigenstates are:

$$|x\rangle = \frac{1}{\sqrt{2}}(|-1\rangle - |+1\rangle)$$

$$|y\rangle = \frac{1i}{\sqrt{2}}(|-1\rangle + |+1\rangle)$$

$$|z\rangle = 0$$

At the high field limit where the Zeeman term is high compared to the fine-structure terms, the fins-structure terms can be treated as a first order perturbation on the Zeeman levels $|0\rangle$, $|+1\rangle$, $|-1\rangle$, which are quantized with respect to the external field. And the pair states can be:

$$|+1,+1\rangle,\ |+1,0\rangle,\ |0,+1\rangle,\ |0,0\rangle,\ |+1,-1\rangle,\ |-1,+1\rangle,\ |-1,0\rangle,\ |0,-1\rangle,\ |-1,-1\rangle$$

Looking at the following equation :

$$S_0 + S_1 \underset{k_2}{\overset{k_{-2}}{\rightleftharpoons}} (TT) \underset{k_1}{\overset{k_{-1}}{\rightleftharpoons}} T_1 + T_1$$

the correlated triplet pair can become a singlet at rate $k_2|S_I|^2$ where $|S_I|^2$ is the fractional singlet character of the pair. In high field notation the pure singlet state that is made of pair state contributions is:

$$|S\rangle = \frac{1}{\sqrt{3}}(|0,0\rangle - |+1,-1\rangle - |-1,+1\rangle)$$

When there is no magnetic field, three pair states have singlet character given by the states that comprise the pure singlet state, given above.

High Field Effect

When a magnetic field greater than 1 kG is applied, only two pair states have singlet character:

$$\psi_1 = \frac{1}{\sqrt{2}} \left(|+1,-1\rangle + |-1,+1\rangle \right)$$

$$\psi_2 = |0,0\rangle$$

Applying a magnetic field reduces the number of triplet pair states that can become singlets from three to two and this leads to a decrease in the rate of the process both for singlet fission as well as triplet fusion. We must note that there is a magnetic field effect because there is a competition between the forward and reverse processes starting from the ^{1}(TT) state. If $k_{-1} = 0$ or ∞, there would be no magnetic field effect.

While the rate always decreases, the magnitude varies depending on the magnetic field direction relative to the crystallographic axis. This is because at certain directions called on-resonance, ψ_1 and ψ_2 become degenerate, and linear combinations of ψ_1 and ψ_2 result in only one state. And so at on-resonance positions, the magnetic field effect is greatest. See **Figure 5.9**.

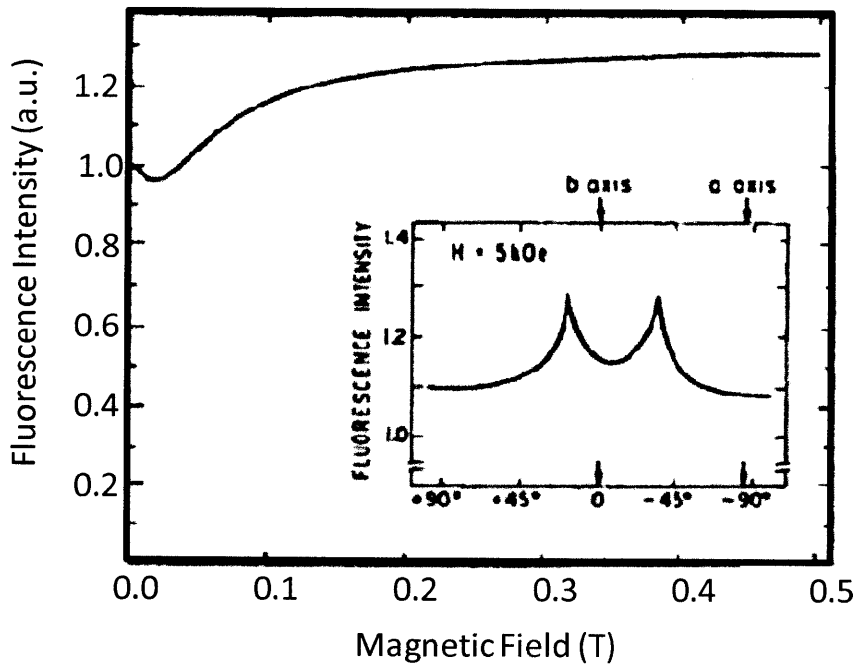

Figure 5.9 A plot showing the change in fluorescence from a tetracene crystal as a function of magnetic field. Inset shows the variation at 0.5T with the orientation of the magnetic field in the ab plane of the crystal. The high field resonance positions occur at angles +18° and -34° with respect to the b-axis. From ref [48].

Low Field Effect

In the low field where H < 1kG when the zero field splitting is comparable to the Zeeman effect, it can be shown that six of the nine intermediate pair states have singlet character and hence the rate of singlet fission or triplet fusion increases from no magnetic field to a certain small value H < 1KG. This results in different set of dips as a function of the orientation of the magnetic field. High field and low field dips are shown for anthracene crystal in **Figure 5.10**.

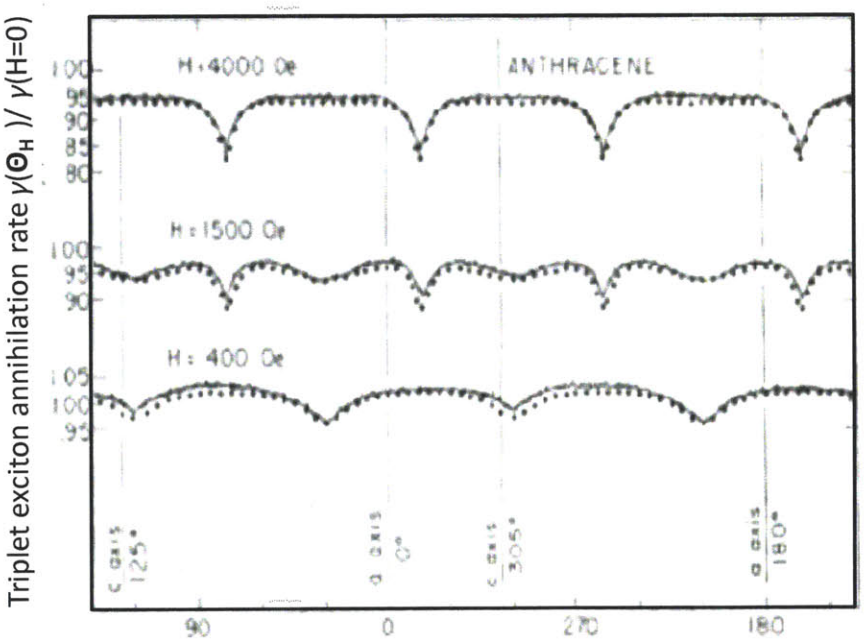

Figure 5.10 Experimental measurements and theoretical calculations (dots) of the anisotropy of the annihilation rate in the ac plane for three magnetic field strengths. The high-field resonances are evident at 4000 Oe (0.4T) and the low-field resonances at 400 Oe(0.04T). At 1500 Oe (0.15T), both sets of resonances coexist. From ref [77].

The magnetic field effect of singlet fission depends entirely on the spins of the species involved and we only took into account H_{spin} in the explanation. The mechanism of the process is still unknown and the renewed interest in singlet fission has led to a lot of work in the area. In the next section we look at a few theories.

5.4 Current theories of singlet fission

5.4.1 Multiexciton intermediate state measured by TR-2PPE

Singlet fission dynamics in pentacene have been explored by Chan et al using Time Resolved 2 Photon Photoemission spectroscopy (TR-2PPE).[80] The main postulate of this work is a multiexciton state that is created almost as fast as the singlet state.

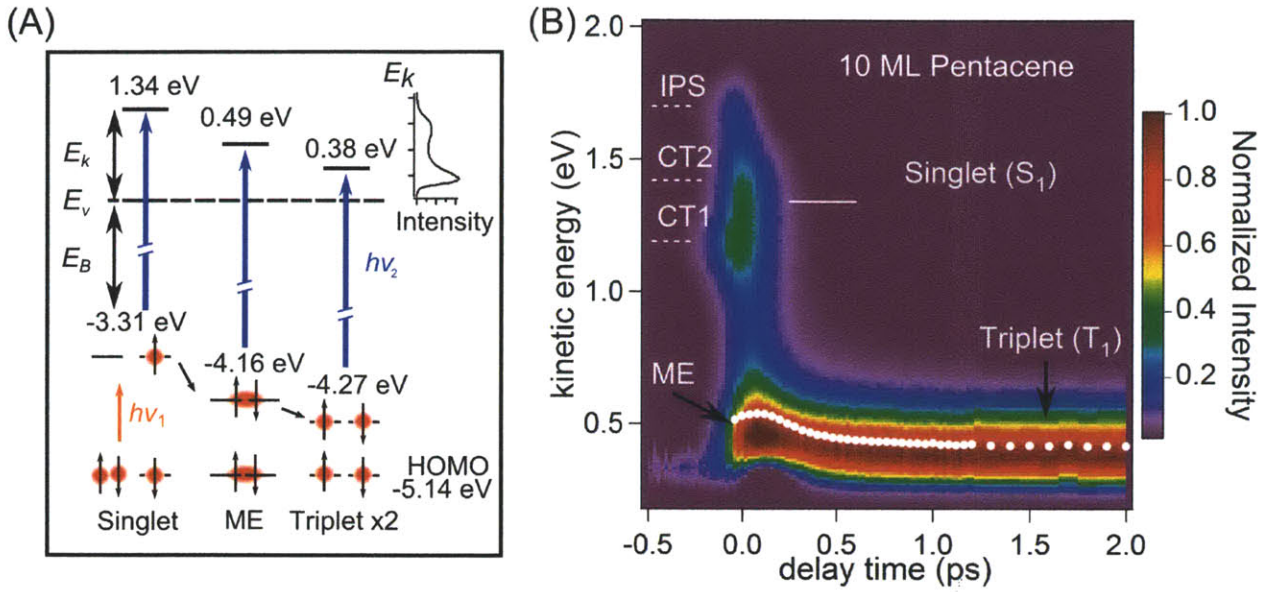

Figure 5.11 Time Resolved - 2 Photon Photoemission Spectroscopy data from ref [80]

The technique excites singlets with a 2.15eV laser pulse pump. This excites singlets states in the pentacene which decay into other states. An ultraviolet 4.25eV probe laser pulse ionizes the excited species, and the energy of the emitted electrons is observed in a hemispherical analyser. **Figure 5.11**(A) shows the energies of the species being probed and of the emitted electrons. A multiexciton (ME) state is stated to be observed at an energy 0.11eV above the triplet state, indicating a triplet pair which has the same energy as the singlet before it can relax to two triplets. Singlet fission in pentacene is an exothermic reaction with an excess energy of 0.11eV.

The time resolved data is show in **Figure 5.11** (B). The notable features are a singlet state at 1.34eV formed within 100fs, and an ME state also formed at the same time, but showing a much higher intensity. They propose that the singlet is formed by absorption of a photon and it couples to the dark ME state with a difference in rise times of less than 20fs – the resolution of the measurement. Modelling the data with this short coupling time, results in a coupling constant of 330meV. The ME

energetically relaxes with a time constant of 260fs and is the main reason for decoupling from the excited singlet state.

They further look at the electrons generated at a C60-pentacene interface and propose that the ME state results in two electrons at the heterojunction. Since a magnetic field effect has been observed in a pentacene-C60 photodetector, their have to be a substantial number of singlets, 55%, which result in a singlet electron before they become an ME or triplets.[81]

5.4.2 Direct singlet fission as seen through quantum beating in tetracene fluorescence

Oscillations in the delayed fluorescence signal from tetracene crystal were seen as early as 1980 in ref [82]. Burdett and Bardeen revisit this work and conclude from the data that there is no electronic coupling between the singlet and triplet states and singlet fission proceeds though the 'direct' mechanism. **Figure 5.12** shows the observed oscillations in the delayed fluorescence of a tetracene crystal, but the same phenomena is also observed in thin films.

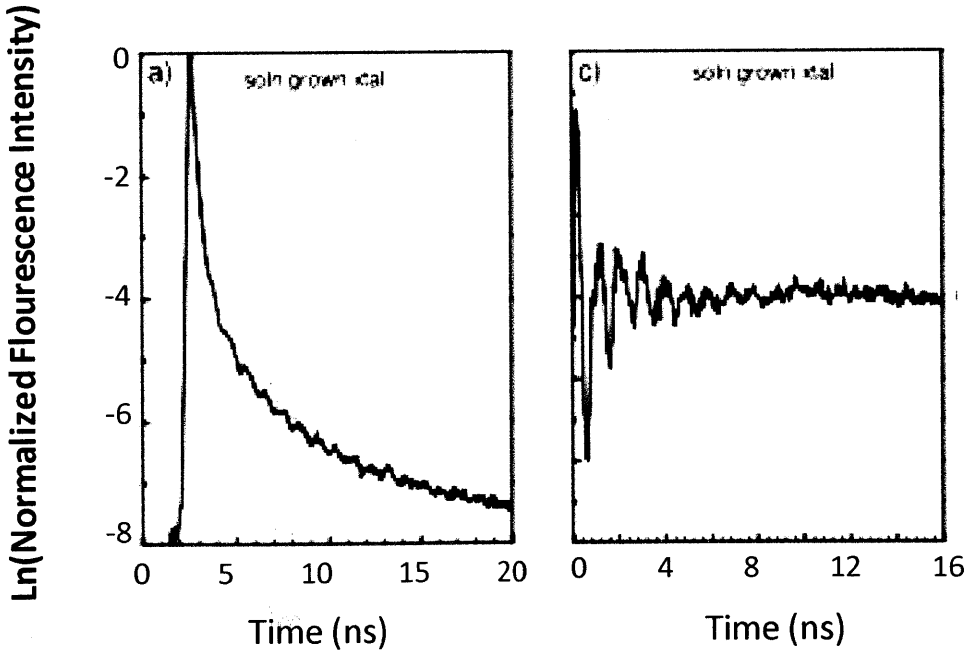

Figure 5.12 (a) Oscillations seen in the delayed fluorescence of a tetracene crystal (b) Same signal after subtracting an exponentially decaying baseline in order to isolate the oscillations. From ref [83].

As we saw earlier in Physics of the magnetic field effect, the excited singlet state couples to the triplet pair states through the nine state basis. At zero field:

$$|S\rangle = \frac{1}{\sqrt{3}}(|xx\rangle + |yy\rangle + |zz\rangle)$$

This is a non-stationary state and the state evolves in time giving rise to quantum beats which couple back to the singlet state at some point giving rise to oscillations at frequencies corresponding to the energies of the three pair states that comprise the singlet. The quantum beating results from coherent geminate triplet pairs and not random encounters of triplets.

The energies of the three stationary states with singlet character are:

$$E_{xx} = 2\left(\tfrac{1}{3}D^* - E^*\right)$$

$$E_{yy} = 2\left(\frac{1}{3}D^* + E^*\right)$$

$$E_{zz} = 2\left(-\frac{2}{3}D^*\right)$$

D^* and E^* are zero field or fine structure parameters that can be determined from EPR (Electron Paramagnetic Resonance) or ESR (Electron Spin Resonance). The energies obtained from calculations are very close to the frequencies extracted from the Fourier transforms of the oscillations. Calculations and data are shown in **Figure 5.13**.

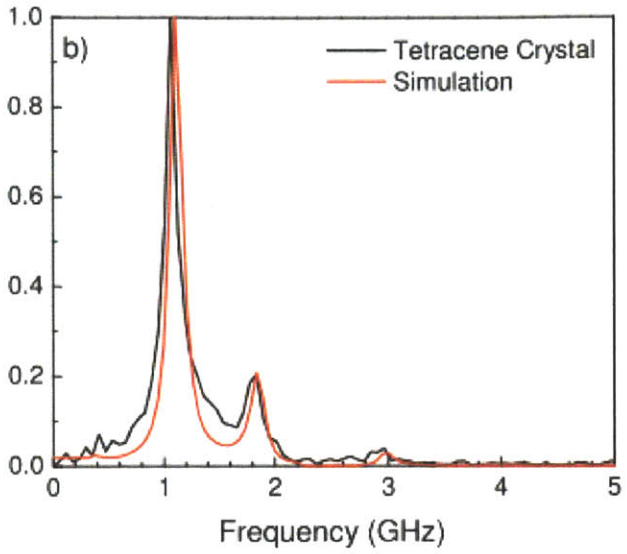

Figure 5.13 Normalized Fourier transforms of the extracted frequencies from tetracene crystal shown in **Figure 5.12**and the simulated data. From ref [83].

A full density matrix treatment model predicts the amplitudes of the oscillations and the damping in addition to the energies. At low temperatures the oscillations decrease due to the slowdown in the rate of singlet fission.

5.5 Low temperature effect on singlet fission in tetracene

Singlet exciton fission in tetracene is thermally activated with an activation energy of 180meV since E_s = 2.32eV and E_t = 1.25eV. This has been observed in the magnetic field effect. As the temperature decreases from room temperature, the increase in fluorescence seen with the application of a magnetic field goes down, as shown in **Figure 5.14**.[64] Triplet-triplet annihilation is not affected by temperature.

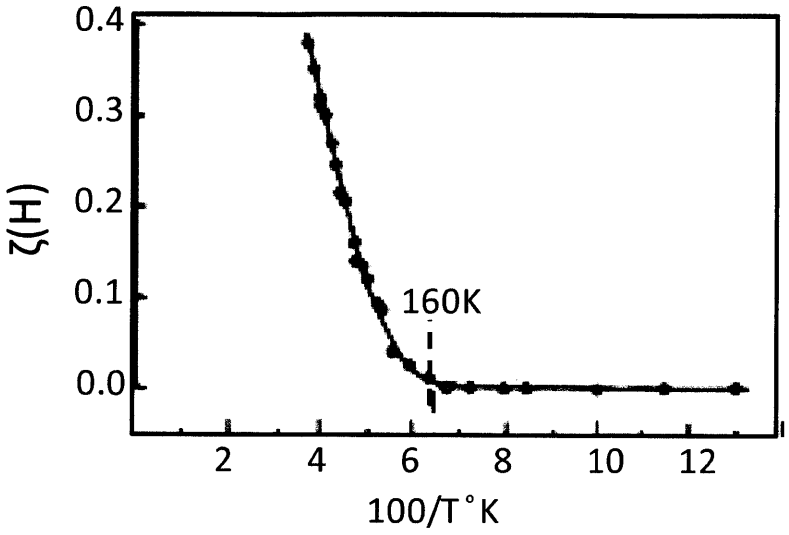

Figure 5.14 Fractional change in the magnetic field effect on fluorescence in tetracene crystal as a function of temperature at 0.4T. At about 160K, singlet fission has been completely quenched. Taken from ref [64].

6 Exploiting singlet fission in a photovoltaic

There has been much interest in multiple exciton generation in quantum dots for implementation in photovoltaics. But heretofore singlet exciton fission had not been implemented in OPVs. Singlet fission was first implemented in a device as a photodetector in a pentacene-C_{60} structure.[81] An external quantum efficiency (EQE) of over 100% was observed at the pentacene absorption peak, and calculations showed an internal quantum efficiency (IQE) enhancement of 145%. In this work we demonstrate a singlet fission photovoltaic comprised of tetracene, copper phthalocyanine and the buckyball C60. To test tetracene in nanostructured blends, we fabricate co-evaporated bulk heterojunctions and multilayer heterojunctions of tetracene and C60. We measure a singlet fission efficiency of (71±18)%, demonstrating that exciton fission can efficiently compete with exciton dissociation on the nanoscale.

6.1 Materials and device structure

We implement here a photovoltaic using the singlet fission material tetracene. Tetracene has a singlet energy of 2.32eV and a triplet of 1.25eV. The ideal band gap for a multiple exciton generation device of multiplicity two is around 0.9eV to 1.1eV. Both tetracene with a triplet at 1.25eV and pentacene with a triplet at 0.86eV are not far from this ideal number. But using pentacene would mean finding a low energy absorber with a band gap of 0.9eV to pair. This is hard in organic semiconductors, so we use tetracene. Tetracene is a very efficient singlet fission material with an observed time constant of ~80ps.[84, 85]

We pair tetracene with C_{60} or buckminister fullerene, a widely used, and only useful acceptor because it has a long exciton diffusion length (40nm) and high electron mobility. If we look at the absorption characteristics of C_{60}, in Figure 7.1, we see it absorbs in the same wavelength region as tetracene 400-550-nm. As we saw in chapter 4, for a singlet fission photovoltaic to be effective, the second material should absorb at half the energy of the singlet fission material. To work around this problem we added a second donor, Copper phthalocyanine (CuPC) to absorb the photons at longer wavelengths. Figure 6.1 also shows the absorption for CuPC. It absorbs from 550-750-nm.

Molecular structures for the active materials are shown in Figure 6.2.

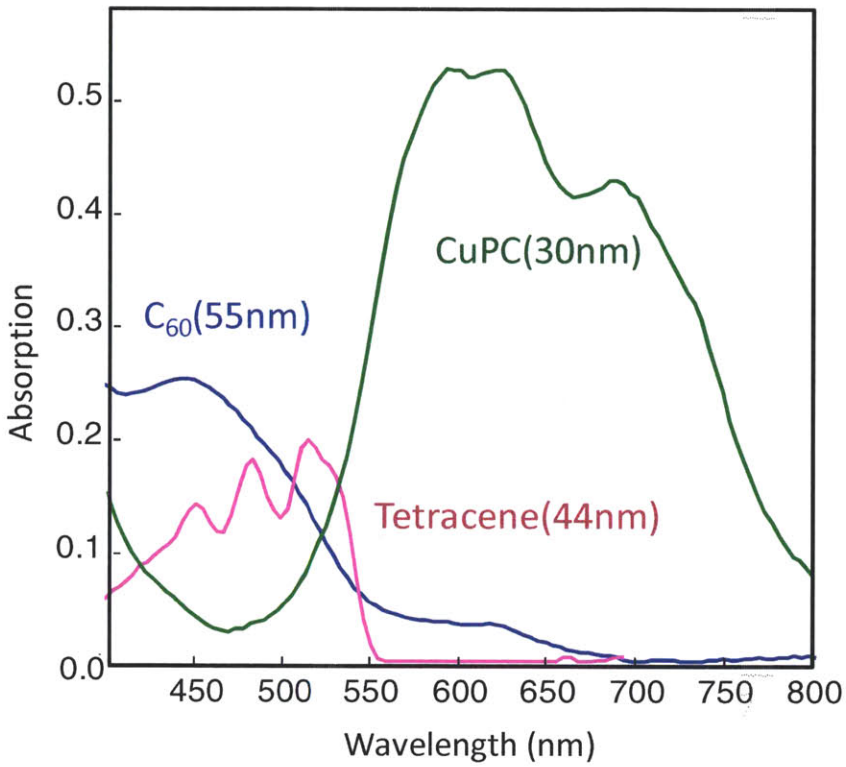

Figure 6.1 Absorptions of vacuum evaporated thin films on glass

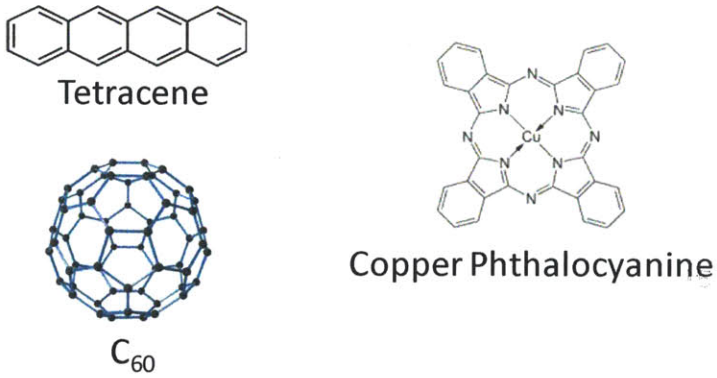

Figure 6.2 Molecular structures of active materials

The implemented device structure is shown in Figure 6.3.

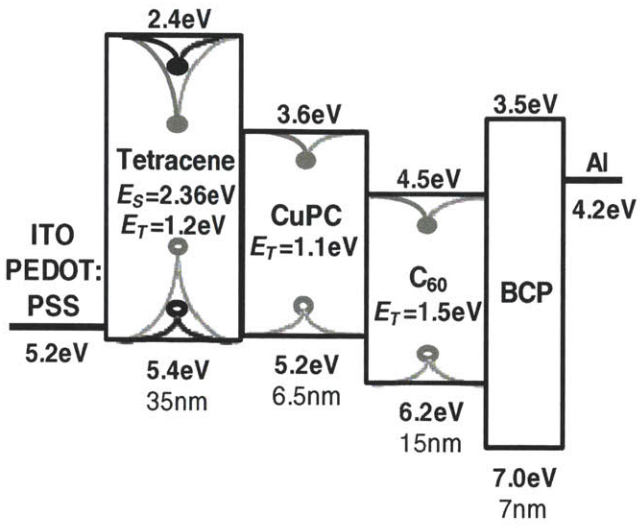

Figure 6.3 The device structure. The grey excitons represent triplets and the black excitons represent singlets.

Besides the active materials, the rest of the device structure is standard for small molecules OPVs.

Indium Tin Oxide (ITO) is the transparent anode deposited on glass through which solar radiation can enter the device. The ITO used in our device has a resistance of 20 Ω/cm^2.

Poly 3,4 -ethylenedioxythiophene:poly4-styrenesulphonate (PEDOT:PSS) is a polymer blend which increases the work function at the ITO interface slightly and also planarizes the ITO surface.

Bathocuproine (BCP) is an exciton blocking layer. The large band gap prevents exciton diffusion to the metal cathode which can quench excitons. The electrons from C_{60} can diffuse to the cathode by hopping through traps below the LUMO created in the BCP layer during metal deposition.

The Aluminum cathode acts as a reflector in OPVs, thereby providing a double path length for the light through the device and hence increasing the absorption in the device. [86]

6.2 Operation

Charge is generated at the CuPC/C_{60} interface[87]. Tetracene absorbs at $\lambda < 550$ nm, and it exhibits singlet exciton fission, generating two triplet excitons with energy $E_T = 1.25$ eV. CuPC absorbs at $\lambda < 700$ nm, and its triplet energy is $E_T = 1.1$ eV, lower than that of tetracene. Thus, triplet excitons from tetracene can diffuse through CuPC to reach the charge generation interface. The highest occupied

molecular orbital (HOMO) energies of CuPC and tetracene are close, (5.2±0.1) eV and (5.40±.05) eV[88, 89], respectively, so hole extraction through tetracene should not present a significant barrier.

6.3 Fabrication

Standard fabrication techniques were employed to build the devices. Devices were fabricated on precleaned glass substrates coated with indium tin oxide. A layer of poly 3,4 - ethylenedioxythiophene:poly4-styrenesulphonate (PEDOT:PSS) was spun-coated onto the glass. All other layers were deposited by thermal evaporation at 3×10^{-6} Torr pressure. The aluminum cathode was defined by a 1-mm-diameter shadow mask. Devices were packaged in a nitrogen environment between two glass slides using an epoxy seal.

6.4 Device structure optimization

The performance of a device depends on the exciton diffusion lengths, charge carrier mobilities, and absorptions in the various materials. We did not know the exact triplet and singlet diffusion lengths in a Tetracene thin film. Also, it was not known how efficiently excitons from tetracene would traverse through CuPC. An optimal set of layer thicknesses were reached by trying out a few different devices structures. Figure 6.4 shows the external quantum efficiency (EQE) measurements carried out on these devices.

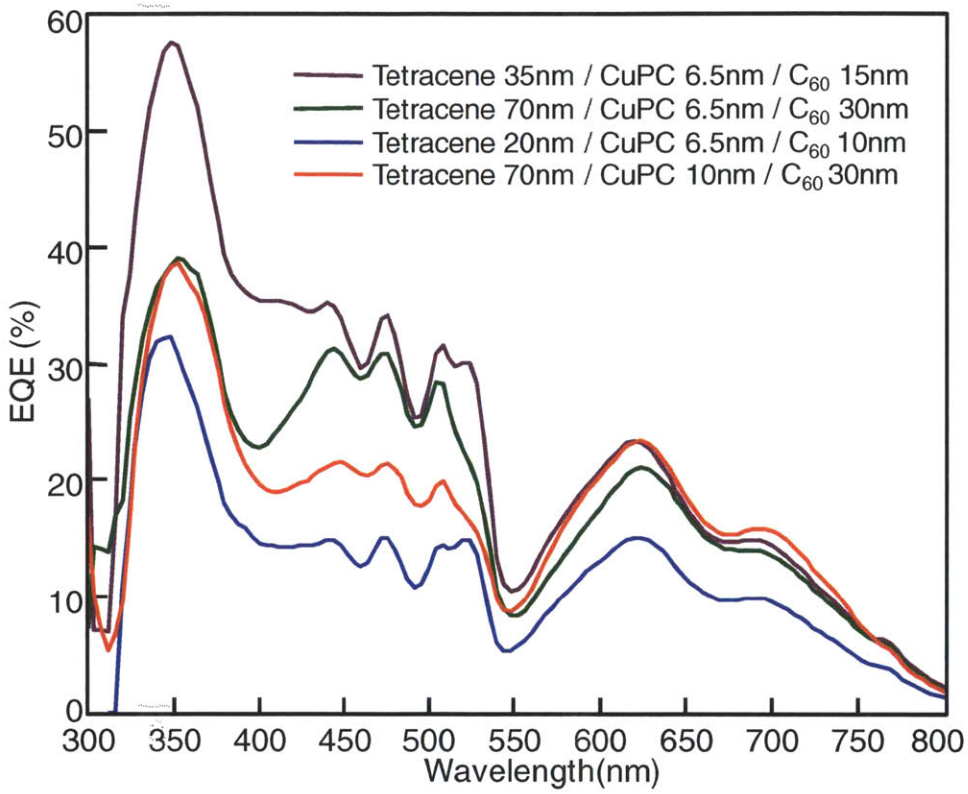

Figure 6.4 External quantum efficiency (EQE) measurements of a number of devices with varying active layer thicknesses

External quantum efficiency or EQE is defined as

EQE = No. of charges generated / No. of photons incident

It is measured as a function of wavelength. The measurement is done by focusing the light from a lamp through a monochromator onto our device and measuring the current at various wavelengths. This measures the number of charges generated. A Newport 818 UV-VIS photodetector is then substituted for the device. With a similar scan across wavelengths, the photodetector output is used to extract the number of photons incident.

6.5 Characterization and Analysis

The device with the overall highest EQE was selected for characterization, and that is the structure in Figure 6.3. The measured EQE for the device is shown in Figure 6.5.

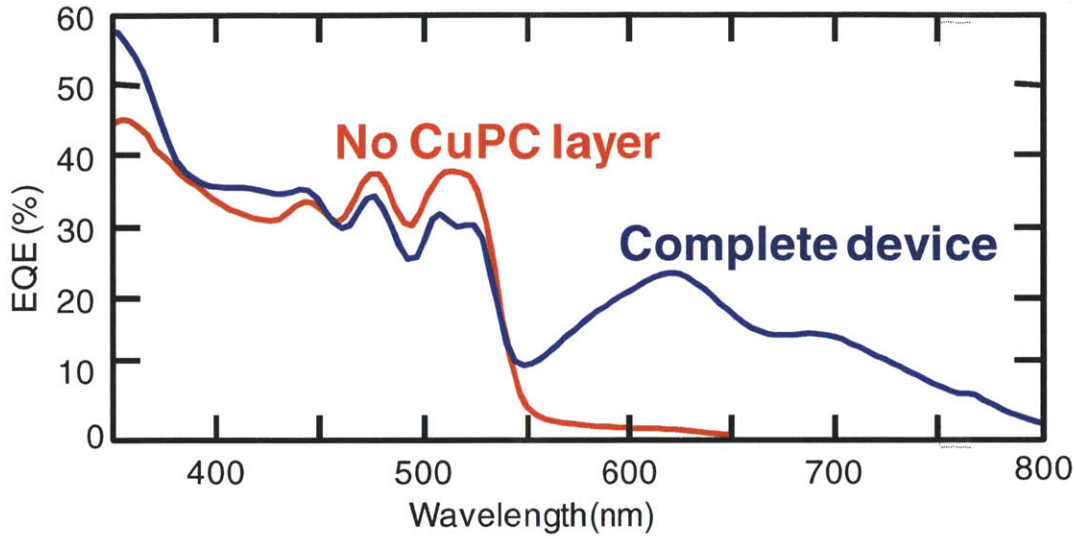

Figure 6.5 The blue line is the EQE for the device in figure 6.1. The red line is the EQE of a similar device minus the CuPC layer

The blue line shows the EQE of the complete device. The shape of the EQE reflects the absorption is the three active materials. We also made a device without the CuPC layer to see what effect the CuPC layer has on the flow of excitons from tetracene to the CuPC-C_{60} charge generating interface. The EQE of this device is the red line in Figure 6.5. Comparing the two EQEs demonstrates that there is no major decrease in the quantum yield of tetracene given the addition of CuPC. This means that the tetracene triplets flow with some efficiency through CuPC.

To get an idea of exciton flow from tetracene through CuPC to charge generating interface we look at the EQE for a tetracene-C_{60} device in **Figure 6.6** and we see a peak EQE of 58% at 530nm and shows a strong contribution from tetracene as can be seen from the much lower value of EQE of 35% at the purely C_{60} peak at 350nm. The device has a tetracene thickness of 100nm. In contrast the maximum EQE for a tetracene-CuPC- C_{60} device is achieved at a tetracene thickness of 35nm, and the EQE at 530nm is 35%.

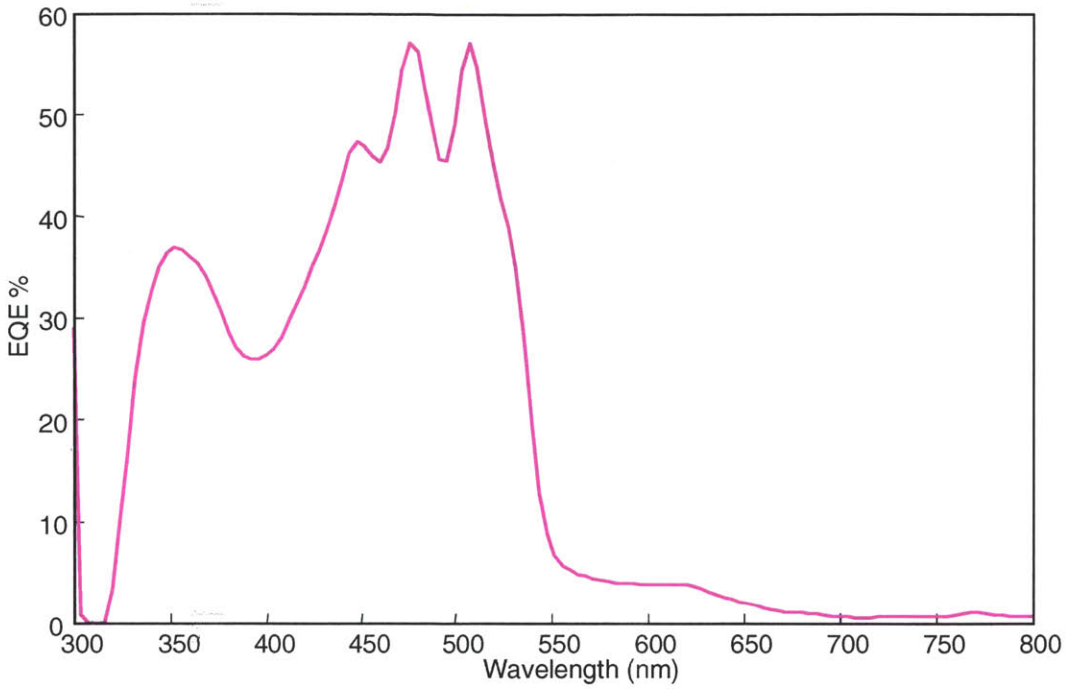

Figure 6.6 EQE data for a tetracene-C_{60} device with structure: ITO/PEDOT:PSS/tetracene (100nm) / C_{60} (30nm) / BCP (9nm) / Al(100nm)

Singlets are transported by the Forster mechanism[90] where the probability of energy transfer from the donor molecule to the acceptor molecule is given by:

$$P_{da} = \frac{3\hbar^4 c^4}{4\pi\varepsilon_r^{\ 2} R^6} \frac{\alpha_a}{N_a} \frac{1}{\tau_d} \int \frac{f_d(E) F_a(E)}{E^4} dE$$

Where R is the separation distance between the two molecules, α_a is the total absorption coefficient of the acceptor (m^{-1}), N_a is the number density of acceptor molecules (m^{-3}), and τ_d is the actual mean lifetime of the donor, $f_d(E)$ is the normalized donor emission spectrum, and $F_a(E)$ is the normalized acceptor absorption spectrum.

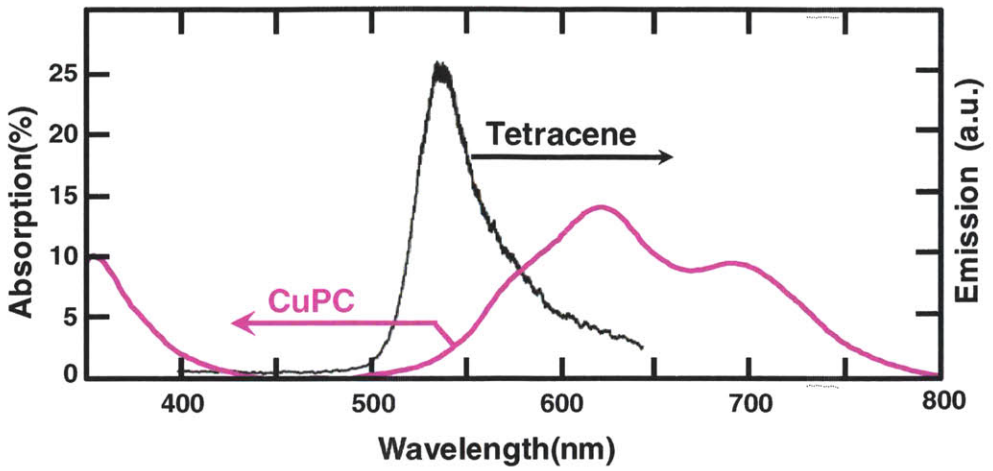

Figure 6.7 Emission spectrum of tetracene[91] and absorption spectrum of CuPC

Figure 6.7 shows a small overlap between tetracene emission and CuPC absorption. But since the distance is to the sixth power in the denominator, it is the overriding factor. And thickening the tetracene should only make it harder for the singlets more than 35nm away from the tetracene-CuPC interface. Which in any case will not make it to the interface and will undergo singlet fission since the singlet diffusion length is ~31nm in thin film – see data in Table 6.1. Hence the drop in EQE from 58% to 35% can be mostly attributed to fewer triplets transferring from tetracene to CuPC.

Table 6.1 Diffusion constants in thin film tetracene

	Triplets	Singlets
Lifetime	100ns[68]	80ps[68]
Diffusion constant cm^2/s	4×10^{-3}[92]*	2×10^{-2}[93]*
Diffusion length $=\sqrt{6\tau D}$ (nm)	490nm	31nm
Diffusion length measured in thin film	100nm[38]	

*Measured in tetracene crystal in ab plane

Figure 6.8 shows the current-voltage characteristic under AM1.5 illumination for the complete device and also without the CuPC layer. For the complete device, VOC = 0.48V, JSC = 2.6 mA/cm2, and the power conversion efficiency = 1.27%. For the device without CuPC, VOC = 0.52V, JSC = 1.0 mA/cm2, and the power conversion efficiency = 0.58%.

The complete device with the CuPC shows an increase in photocurrent over the device without CuPC but only a slight decrease in open circuit voltage.

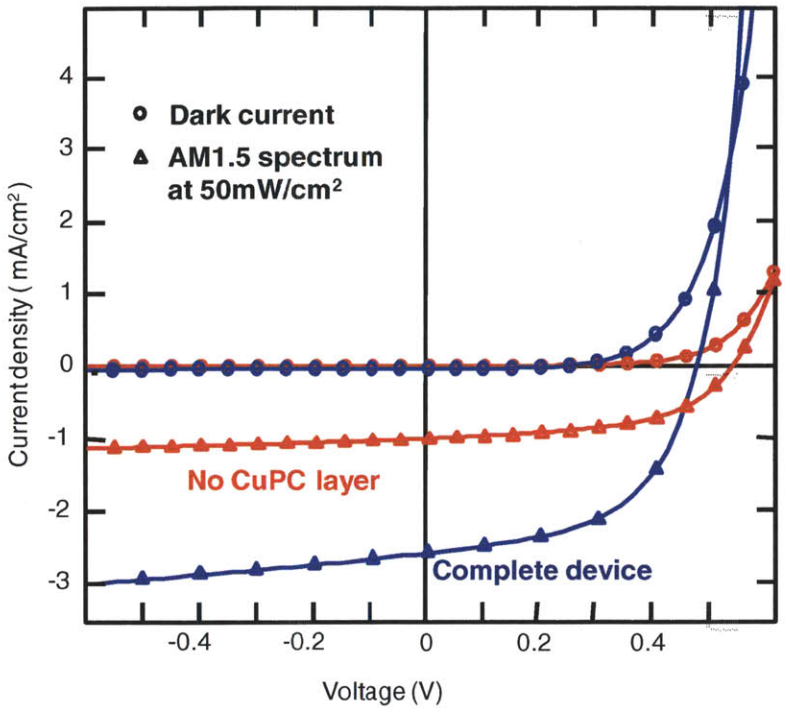

Figure 6.8 Current voltage characteristic for the complete device, and the device minus CuPC layer

This concludes the basic characterization of the device. The next step is to test the presence of singlet fission and quantify the contribution of singlet fission.

6.6 Observing the effect of singlet fission

6.6.1 Magnetic field effect

We used a magnetic field to observe the effect of singlet fission in our device. We saw in section 5.3 that the rate of singlet fission is affected by a magnetic field. In tetracene, it increases from about .05T to .3T and saturates above .3T. In our device we expect that each singlet that undergoes fission contributes to two charge carrier pairs instead of one, hence as the rate of singlet fission drops, the photocurrent should also drop.

We did photocurrent measurements varying the magnetic field and a clear drop in photocurrent is observed on application of a large enough magnetic field (> .1T), thus proving the presence of singlet fission in the operation of our device. The data is presented in Figure 6.9.

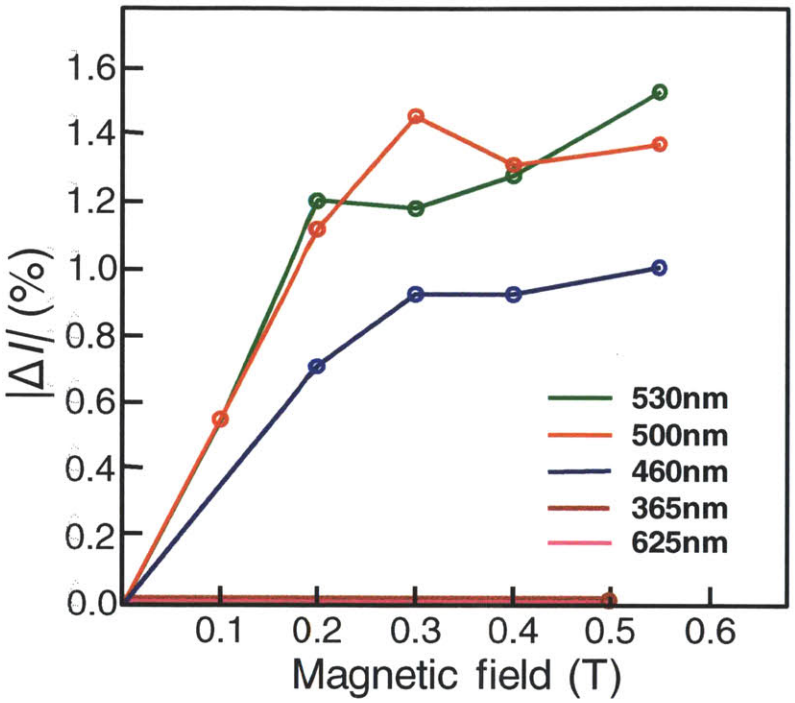

Figure 6.9 Magnetic field dependence of photocurrent in the photovoltaic

The photocurrent was measured at several different excitation wavelengths. The y-axis shows the absolute % change in photocurrent. At 365nm and 625nm where C60 and CuPC respectively have substantial absorption and tetracene has almost none, the effect is non-existent. At the other three wavelengths in the figure, 530nm, 500nm and 460nm, the effect is roughly proportional to the tetracene absorption. This is made more obvious in Figure 6.10. The solid lines shows the calculated absorptions in tetracene, CuPC and C_{60}. The blue symbols show the magnitude of the magnetic field effect at .55T for the various wavelengths from Figure 6.9.

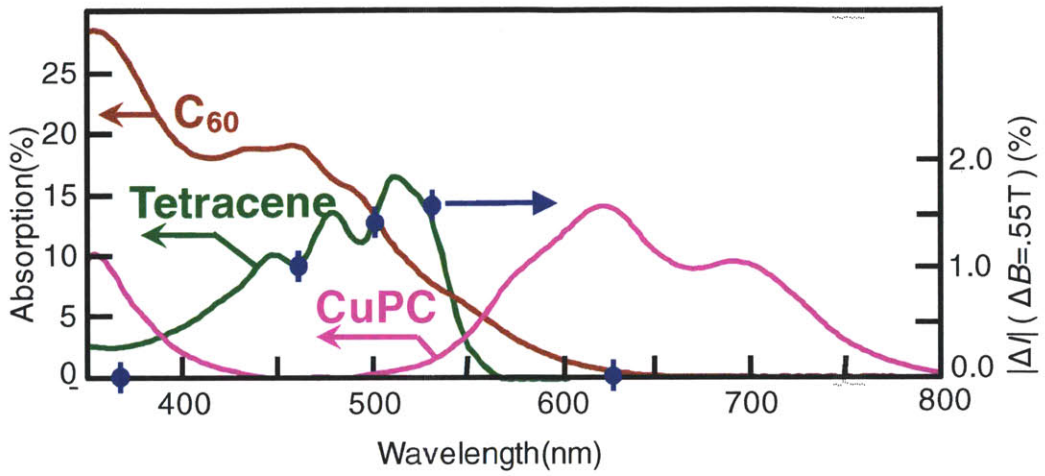

Figure 6.10 Calculated absorptions in the active layers. The blue symbols show the magnetic field effect at different wavelengths

Other than singlet fission, a magnetic field can also affect the photocurrent through charge reaction and recombination effects. But since the magnetic field effect is clearly a function of tetracene absorption we can be certain that this is the effect of singlet fission. The noise is too high to see the effect below .1T else we should have seen a reversal in the effect and a corresponding increase in the photocurrent.

The magnetic field effect proves the desired effect of singlet fission but it is hard to find the quantitative contribution from this data. We would need the rates of singlet fission, charge transfer state formation, singlet transport and triplet transport in tetracene and CuPC.

The common method used in MEG devices, is to calculate the internal quantum efficiency (IQE).[81] [58]IQE is defined by:

IQE = no. of charges generated / no. of photons absorbed

= EQE / fraction of incident photons absorbed

In a device that exhibits MEG the IQE is greater than 1. Since we cannot measure the absorption in the individual layers in the device separately, we calculate the absorption in each of the layers in our device using optical modeling. Figure 6.11(b) shows the calculated absorption in the active layers on the device and Figure 6.11(a) shows the EQE. If we look at the CuPC absorption from 600-700-nm, the IQE is greater than one which is unexpected since there is no MEG in CuPC.

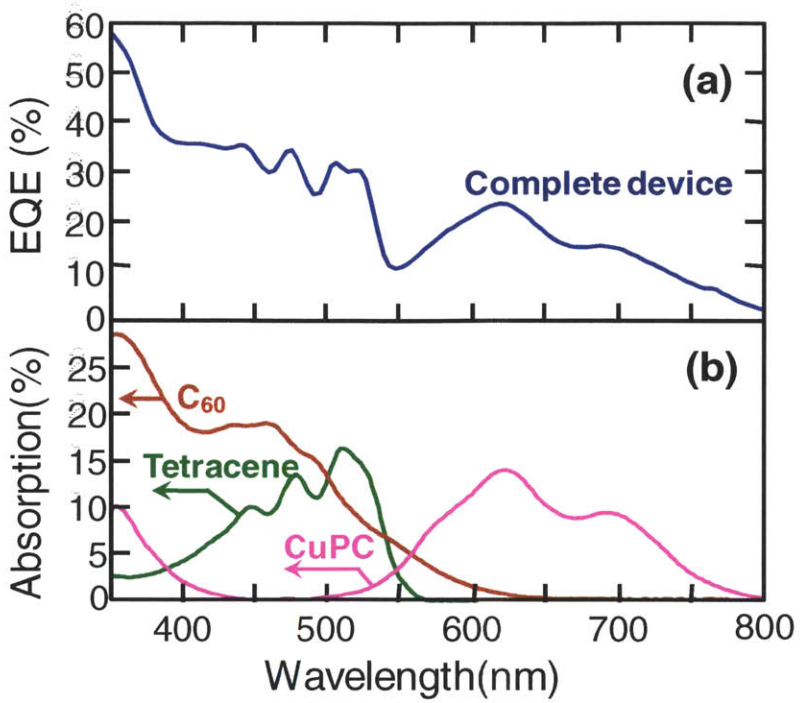

Figure 6.11(a) EQE of tetracene-CuPC-C60 photovoltaic (b) Calculated absorption in the active layers of the device

We postulate that this is because the actual absorption in the device is greater than the calculated absorption. This is because the tetracene thin film is highly polycrystalline as can be seen from the scattering nature of film and also from x-ray diffraction studies[94]. This leads to a rough cathode, scattering in the device, and hence higher absorption than the optical modeling technique which assumes planar layers would calculate.

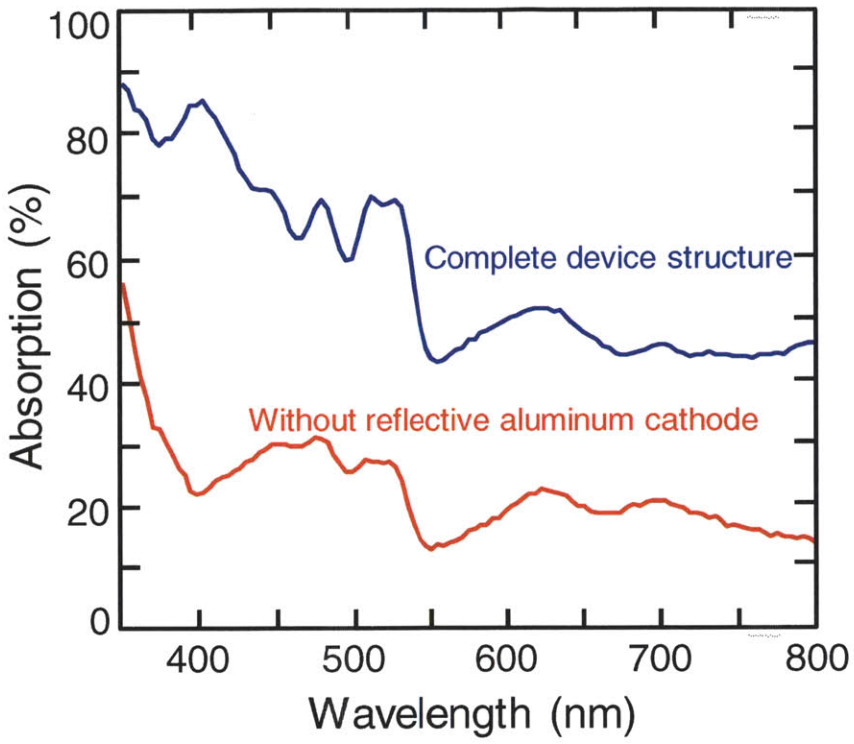

Figure 6.12 Absorption measurements carried out in an integrating sphere on the photovoltaic device structure with and without reflective aluminum cathode

Figure 6.12 has the results of an absorption measurement carried out in an integrating sphere. The cathode seems to add a baseline absorption, especially in the infrared near 800nm. The metal cathode is known to add parasitic absorptions through all wavelengths, but more so in the 650-800-nm region.[95] The scattering film and the parasitic absorptions together make it hard to estimate the absorption in each of the active layers separately. And so we cannot use absorption to calculate the IQE. We use another property, the low temperature effect on singlet fission in tetracene, to determine the increase in IQE due to singlet fission.

6.6.2 Low temperature effect of singlet fission in tetracene

In tetracene the process of singlet fission is thermally activated[64]. The singlet energy E_s = 2.32ev and triplet energy E_t = 1.25eV, so E_s is slightly lower than 2*E_t. At lower temperatures the singlet fission yield will drop.

If we consider any OPV, with a reduction in temperature the performance of the OPV will drop due to reduced charge carrier mobility, shorter exciton diffusion lengths in the case of triplets since Dexter

transfer is a thermally activated process, and also perhaps lower charge transfer (CT) state splitting rate. But in a tetracene OPV that exploits singlet fission there will be the additional effect of the singlet fission yield dropping.

In a device with just two materials tetracene and C_{60}, as the temperature drops, the tetracene contribution should drop faster than the C_{60} contribution. The EQE in C_{60} can be quantified as:

and the tetracene absorption is very low. At 200K that trend is reversed thereby proving that the EQE_{Tc} drops faster than EQE_{C60}

$$EQE_{C60}(T) = \eta_{A,C60} \times \eta_{ED,C60}(T) \times \eta_{CT,C60}(T) \times \eta_{CC,C60}(T) \qquad 1$$

The terms, in the order they appear in the equation, are: efficiency of exciton diffusion to a tetracene-C60 interface, efficiency of charge generation at the donor/acceptor interface, the efficiency of charge collection. The EQE in tetracene will have an additional term due to singlet fission:

$$EQE_{Tc}(T) = \eta_{A,Tc} \times \eta_{ED,Tc}(T) \times \eta_{CT,Tc}(T) \times \eta_{CC,Tc}(T) \times \left[1 + \eta_{sf}(T)\right] \qquad 2$$

η_{sf} is the efficiency of singlet fission.

We try to construct a device structure where except for the absorption, and the singlet fission efficiency, if all the other terms are the same in both materials. $\eta_{CT}(T)$ and $\eta_{CC}(T)$ are the same for both materials since they are efficiencies that relate to the tetracene-C_{60} CT state, which is the same regardless of the provenance of the exciton. To get the same $\eta_{ED}(T)$ we construct a multilayer structure with very thin alternating layers of the two materials as shown in Figure 6.13. Since the thicknesses of the layers are very thin, 2nm and 1nm respectively, all excitons will get to a charge generating interface, hence $\eta_{ED}(T)=1$ for both materials. This structure and strategy was used by *Lee et al* in a pentacene-C_{60} photodetector[81].

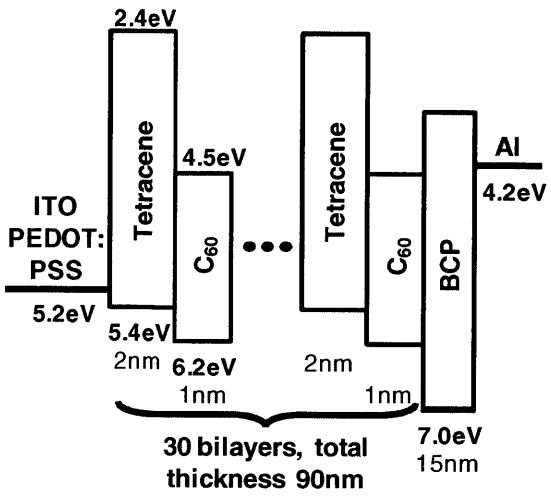

Figure 6.13 A tetracene –C_{60} multilayer device structure ensures an exciton diffusion efficiency of one

In such a structure:

$$\frac{EQE_{\mathrm{Tc}}(T)}{EQE_{\mathrm{C60}}(T)} = \frac{\eta_{\mathrm{A,C60}}}{\eta_{\mathrm{A,Tc}}}[1 + \eta_{\mathrm{sf}}(T)] \qquad 3$$

We made the device in Figure 6.13 and measured the EQE at various temperatures. The data is displayed in Figure 6.14. The solid lines are the EQEs at various temperatures and the dashed lines are the absorption spectra of the two materials. The absorption spectra are shown only for consideration of the shapes, the relative or absolute magnitudes are arbitrary

As the temperature drops, the EQE in the device drops at all wavelengths. But a closer look shows that the tetracene contribution drop faster than the C60 contribution. At 292K, the tetracene peaks (420-550-nm) are higher than the EQE at 370nm at the left edge of the plot where the C_{60} absorption is high

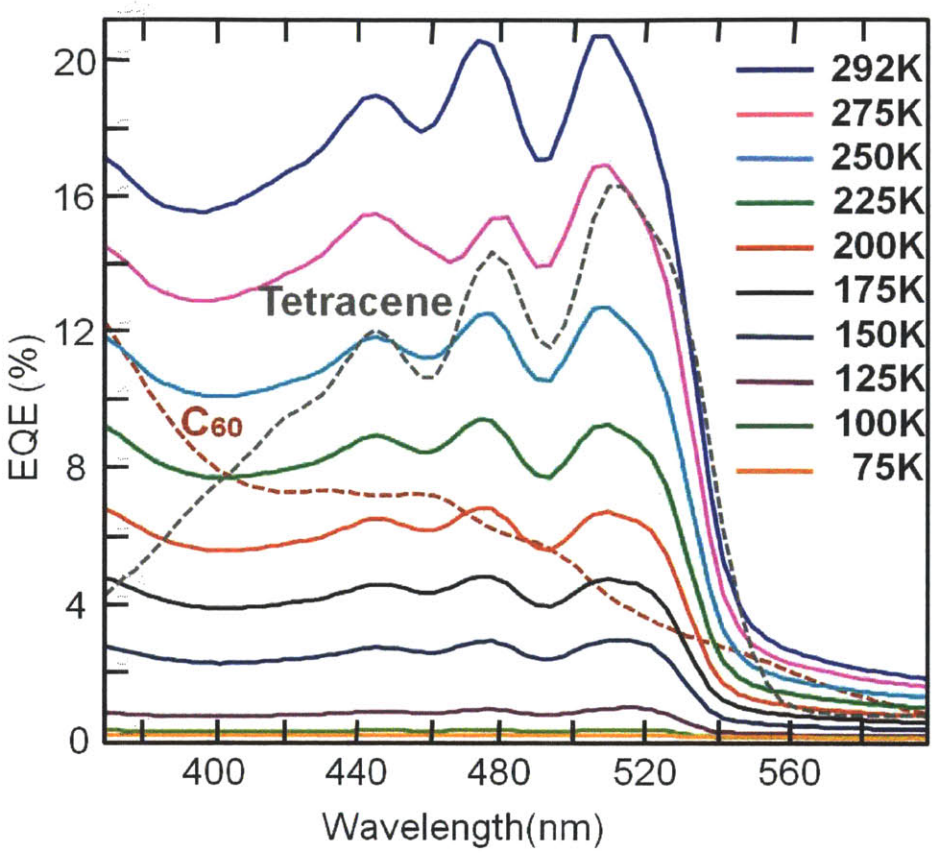

Figure 6.14 EQE of multilayer tetracene-C_{60} device at various temperatures. The dashed lines are the absorption spectra of tetracene and C_{60}

and the tetracene absorption is very low. At 200K that trend is reversed thereby proving that the EQE_{Tc} drops faster than EQE_{C60}. We now quantify this effect.

The *EQE*s can be written in terms of the absorptions and the internal quantum efficiency or *IQE*, where *IQE* = (no. of photons absorbed) / (no. of charges generated):

$$EQE_{C60} = \eta_{A,C60} \times \left[IQE_{C60} = \eta_{ED,C60}\, \eta_{C,C60} \right] \quad (4)$$

$$EQE_{Tc} = \eta_{A,Tc} \times \left[IQE_{Tc} = \eta_{ED,Tc}\, \eta_{C,Tc}(1 + \eta_{sf}) \right] \quad (5)$$

$$EQE = EQE_{C60} + EQE_{Tc} \quad (6)$$

We calculated the absorption yields in the two materials through optical interference modeling using the transfer matrix method.[86] Then we find the *IQE*s (which are constant across wavelengths) by

finding fits to the EQE data with the calculated absorptions. This is shown in Figure 6.15(a). Only three of the temperatures are included in the figure for clarity.

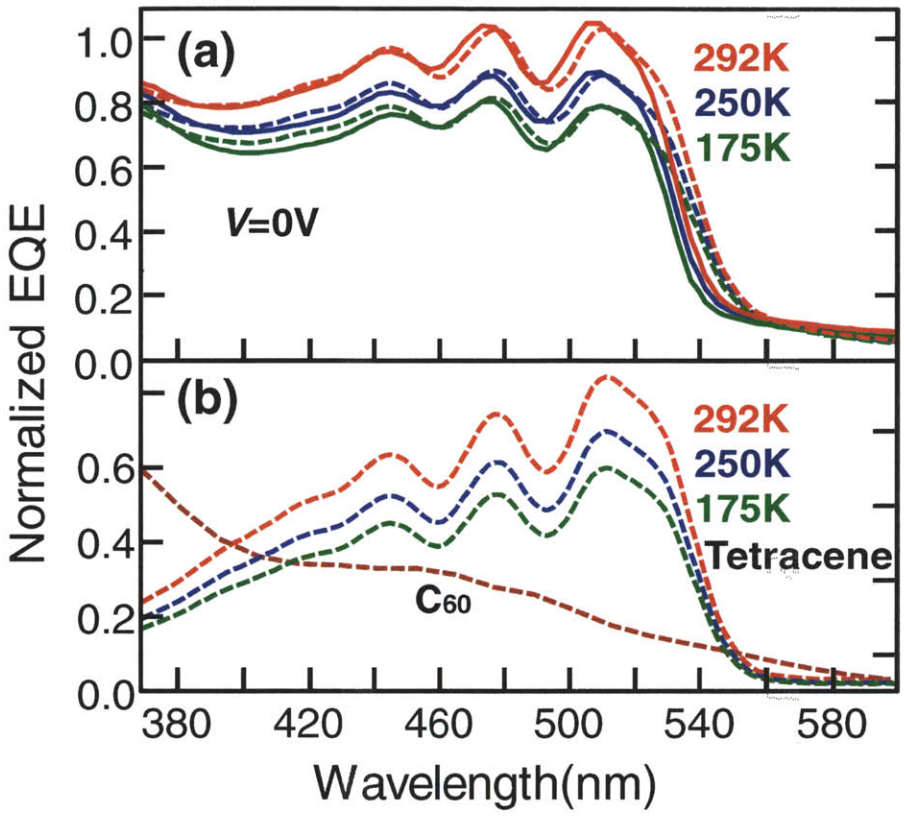

Figure 6.15(a) EQE data for the tetracene-C_{60} multijunction photodetector structure. Solid lines show measured EQE at three different temperatures. The dashed lines are simulations. (b) Simulations split into EQE contributions from tetracene and from C_{60}. All the EQE data in this figure has been normalized to keep the C_{60} EQE constant. The tetracene EQE is seen to drop with temperature.

The EQEs generated from the fits are used to calculate the singlet fission efficiency using equation 3. The results are shown in Figure 6.16. The blue dots are generated from the fits displayed in Figure 6.15, and the error bars represent the efficiency generated from simulation fits within a correlation of .88 to the data. As can be seen at room temperature, of all the excitons that contribute to current, 28% singlets that become charge carriers and 72% of the singlets undergo fission to generate triplets that become charge carriers.

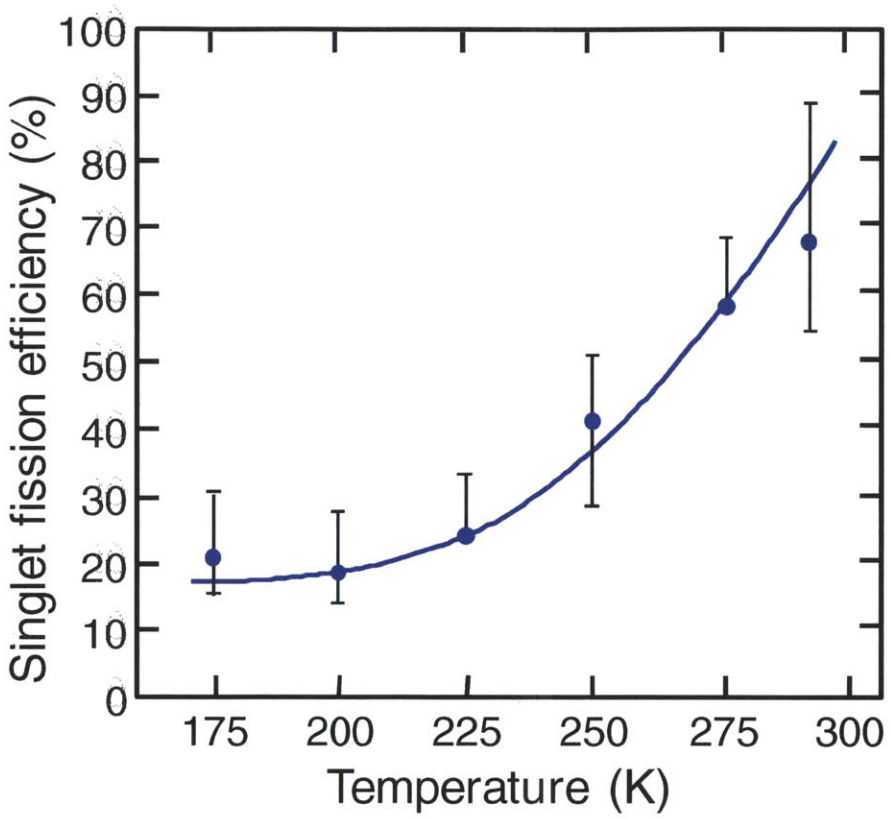

Figure 6.16 Singlet fission efficiency determined from the EQE simulations. The line is a guide to the eye. The error bars represent simulation fits with a correlation of .88 or greater to the EQE data.

This high singlet fission efficiency result is somewhat unexpected in this structure considering the rates of singlet fission and CT state formation. The time constants for singlet fission in tetracene have been observed as 50ps[50], and more recently as 10 ps[68]. Typical CT formation time constants are: in C_{60} - BCHA-PPV and P3OT, an upper limit of 300fs[96] , in C_{60} - MEH-PPV less than 100fs, limited by the resolution of the measurement[72], in PCBM - MDMO-PPV 45fs as measured with a resolution of 10fs[97], in CuPC-C_{60}, a singlet formed in CuPC transfers an electron to C_{60}within 100fs[98]. From these numbers it was expected that the singlets close to an interface would form CT states faster than they could undergo singlet fission, which is not the case in this multilayer structure. This could partially be due to aggregation of tetracene. We explored this further through a series of bulk heterojunction structures which is the subject of the next section.

6.7 Tetracene-C_{60} bulk heterojunction structures

We fabricated a series of co-evaporated blend structures as shown in Figure 6.17. A series of such devices were made with varying tetracene-C_{60} ratio. We expected that as the tetracene content decreased, the probability of an exciton undergoing fission rather than forming a CT state would decrease. We measured the magnetic field-induced modulation of the photocurrent in these devices to observe the effect of singlet fission.

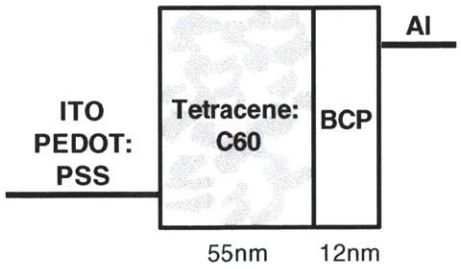

Figure 6.17 Bulk heterojunction tetracene-C_{60} photovoltaic

As shown in Figure 6.18, we observe no significant change in the singlet fission efficiency for tetracene concentrations down to 12%. Theory suggests that exciton fission can occur given two adjacent tetracene molecules[99], and this data confirms that the process can compete with exciton dissociation even in blended morphologies.

This is an important result because it means that singlet fission can be exploited in bulk heterojunction photovoltaics which are among the most efficient organic solar cells today.

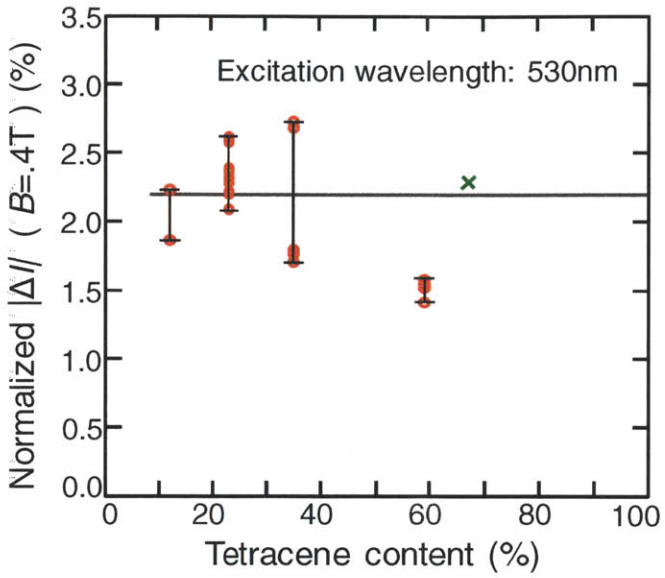

Figure 6.18 Magnetic field effect on bulk heterojunction devices with varying tetracene content. Each red dot represents one device. |ΔI| has been normalized by the tetracene content since C60 also generates current at λ = 530nm. The line is a guide to the eye. The green cross represents the multilayer structure which has a fractional tetracene content of 0.67.

To conclude, we demonstrated a photovoltaic cell structure that exploits singlet exciton fission leading to improved efficiency. The alternative structure of stacked multijunction organic solar cells must satisfy current matching constraints at each junction, and the complete device can be challenging to fabricate, especially using solution processing. In contrast, here we have demonstrated that singlet exciton fission is compatible with blended solar cell morphologies, suggesting that it may be employed to boost the performance of conventional solution-processed organic solar cells.

7 Anomalous singlet exciton fission magnetic field effect in diphenyltetracene-C_{60} solar cells

In our quest for exploiting singlet fission in photovoltaics we went on to explore more materials and configurations. Since we saw that singlet fission was possible in bulk heterostructures, we looked for materials that are soluble and can be used in solution processed bulk heterojunction cells. Tetracene and pentacene are highly insoluble, but there derivatives with added side chains are soluble. With this in mind we made devices from 5,6-diphenyl-tetracene (DPT), and saw some interesting magnetic field effects.

In this chapter we show the presence of singlet fission in DPT and explore its effect in a DPT-C_{60} device. The effect of singlet fission is to lower the current in the device rather than increase it like in previous device implementations, the tetracene solar cell described previously and a pentacene photodetector.[81, 100] This is because the energy of the triplet E_t = 1.2eV is too low to form charge transfer states (CT) at the DPT- C_{60} interface. We explore the reasons for the strong magnetic field effect observed in the device and propose an isotropic magnetic field detector exploiting this effect.

7.1 Singlet fission in 5,6-diphenyl-tetracene

A clear signature of singlet fission[48] is observed in the magnetic field effect on DPT fluorescence shown in Figure 7.1. Also shown for comparison is the same measurement on a thin film of tetracene. The data in Figure 7.1 is a steady state measurement showing the total fluorescence. The magnetic field reduces the rate of singlet fission as well as of triplet-triplet annihilation (TTA), or triplet fusion, hence increasing the prompt fluorescence and at the same time decreasing the delayed fluorescence[67]. But since the excitation wavelength generates singlets, there is an overall increase in fluorescence.

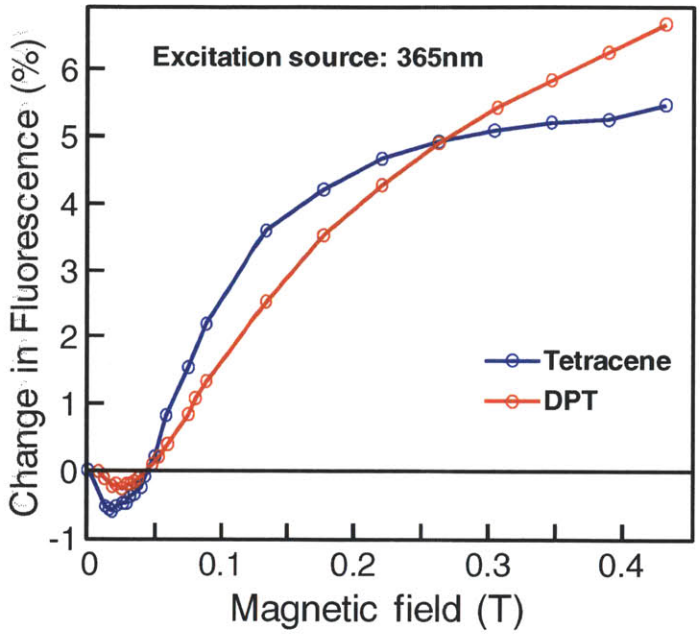

Figure 7.1 Change in fluorescence with magnetic field for tetracene and DPT thin films. The films were packaged in a nitrogen environment to protect from exposure to oxygen and moisture.

7.2 DPT-C_{60} device structure and characterization

Figure 7.2 shows the DPT-C_{60} device being investigated.

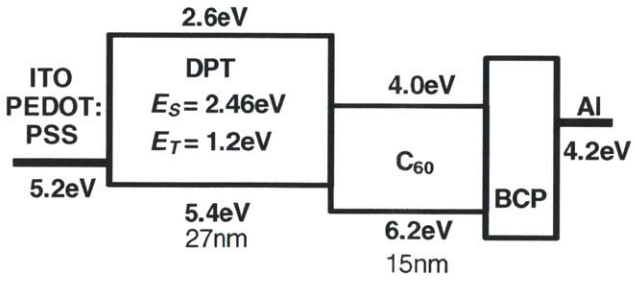

Figure 7.2 Structure of DPT-C_{60} device

The device external quantum efficiency (EQE) in Figure 7.3 has the three DPT absorption peaks from 440-500-nm[101], and the broad C_{60} contribution from 400-530-nm[100]. The EQE of the device is in general low compared to the tetracene-C_{60} bilayer device in the last chapter.

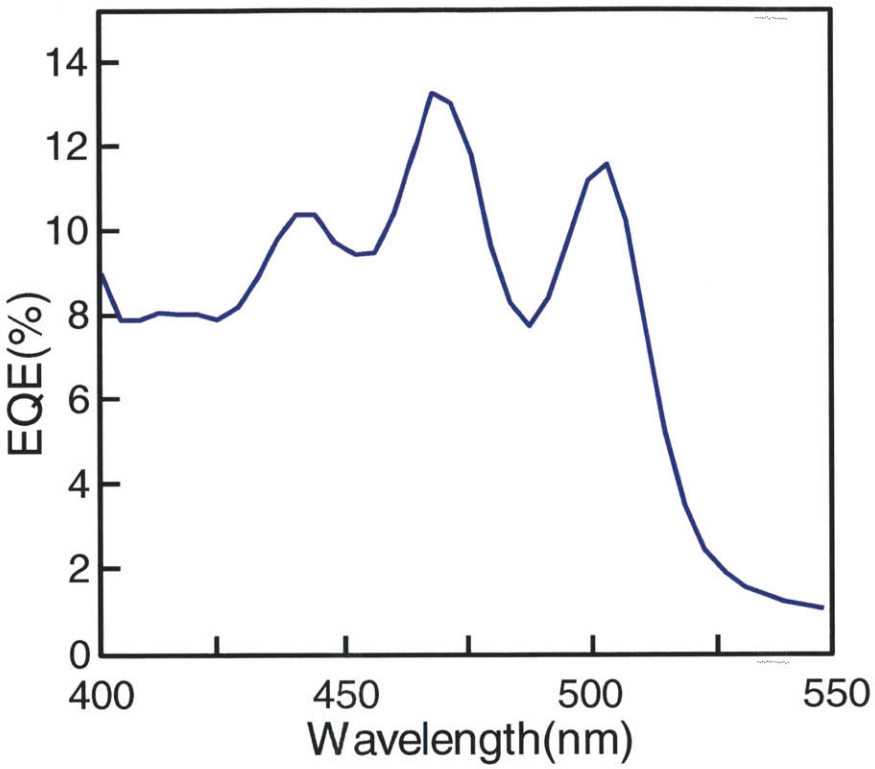

Figure 7.3 External quantum efficiency (EQE) data for the DPT-C_{60} device under investigation

The current-voltage characteristic shown in Figure 7.4 exhibits a slight S-shaped curve near V_{oc} which may be indicative of charge trapping resulting in a slightly higher V_{oc} = .975V compared to Roberts et al.[101] Some devices did not have the S-shaped curve and in those cases V_{oc} = .725V.

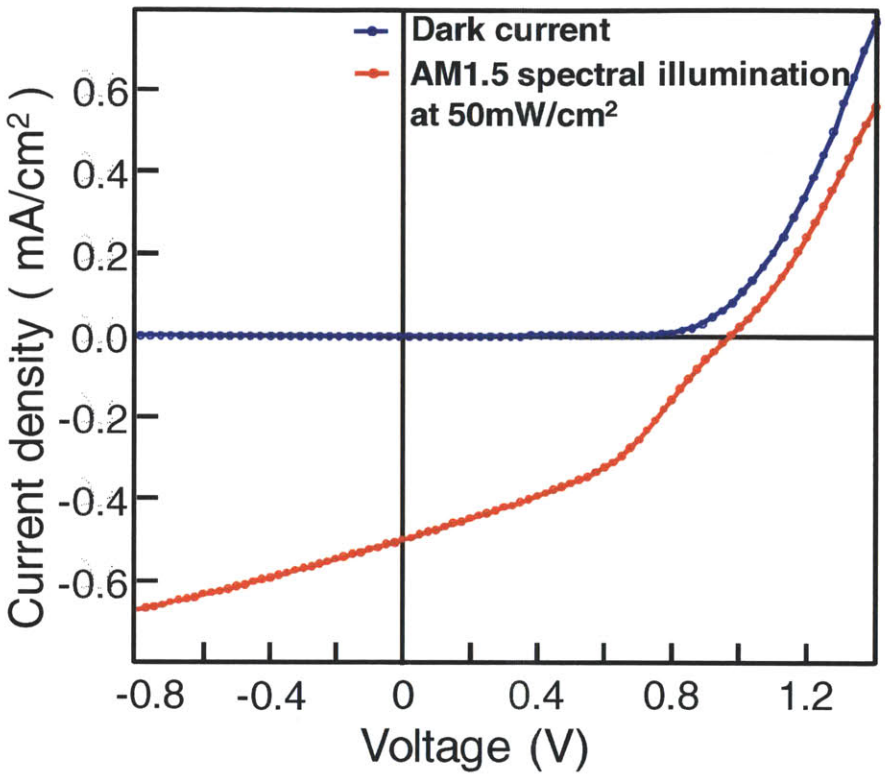

Figure 7.4 Current-voltage characteristic for the DPT-C_{60} device under investigation

7.3 Anomalous magnetic field effect

We use the magnetic field effect to observe singlet fission in the devices. The effect of singlet fission in the device is demonstrated by the variation of photocurrent with magnetic field shown in Figure 7.5. At an excitation wavelength of 500nm, where the DPT absorption is dominant, there is a clear positive change in photocurrent.

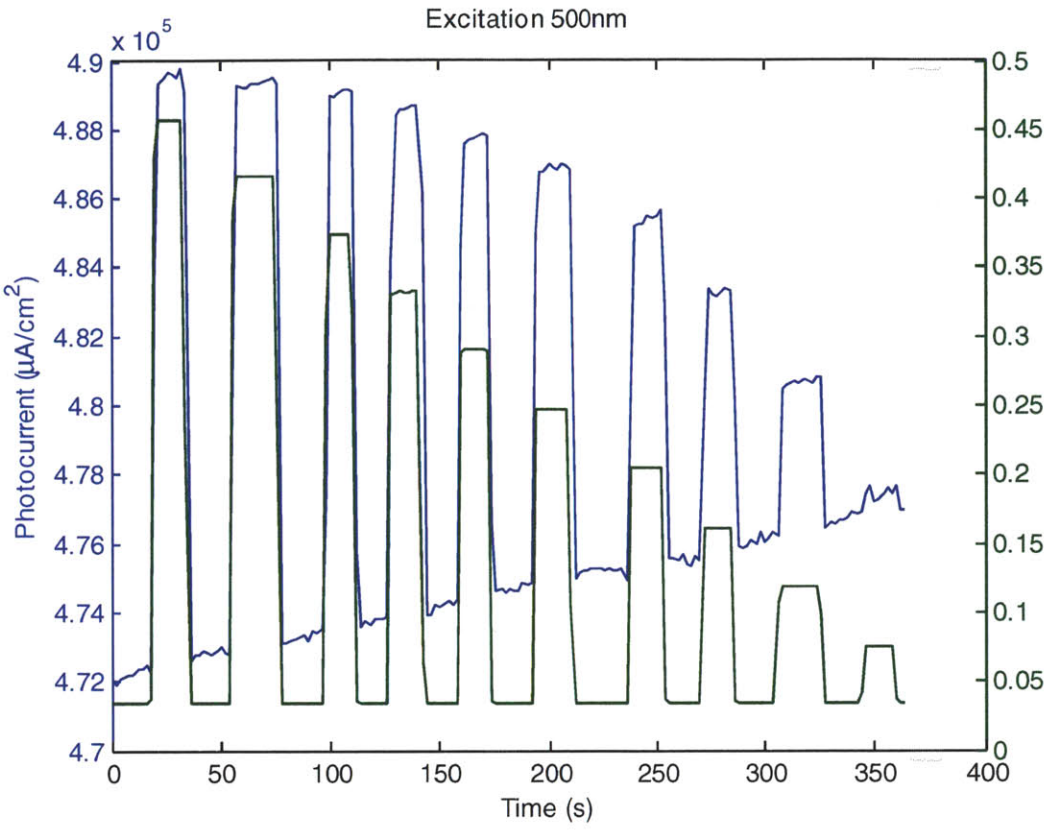

Figure 7.5 Change in photocurrent and magnetic field as a function of time in the DPT-C60 device. For magnetic fields shown here > .07T, the change is always positive with an applied magnetic field.

The effect is positive in this device as opposed to tetracene-C_{60} where the effect if negative.[100] This can be explained by the relative energies of the triplet, CT, and singlet energies: $E_{t,\,DPT} = 1.2eV < E_{CT,\,DPT\text{-}C60} < E_{s,\,DPT} = 2.4eV$[102]. It is energetically favorable for the singlets in DPT to form CT states and result in photocurrent, but not for the triplets. Since a magnetic field suppresses singlet fission, it will result in fewer triplets and more singlets, thereby leading to higher current. See **Figure 7.6**. The high CT energy is also borne out by the high open circuit voltage of .725V in the device.

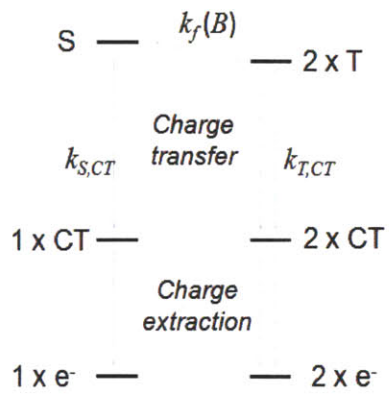

Figure 7.6 Singlet fission and CT state formation dynamics at a heterojunction

Figure 7.7 shows the change in photocurrent at very low magnetic fields too, and the dip in photocurrent at very low fields is a clear signature of singlet fission. At 365nm where the DPT absorption is very low and C_{60} has a strong absorption, we see a .5% effect at .45T. This slight effect may be because the excitation source had a spread of ~50nm, and there is some DPT absorption at 375-400-nm. But effectively we see magnetic field effect from DPT and not from C_{60}. These two observations confirm that the effect we are seeing is due to singlet fission and not due to dissociation or charge reaction which have been observed in organic semiconductor devices.[103, 104]

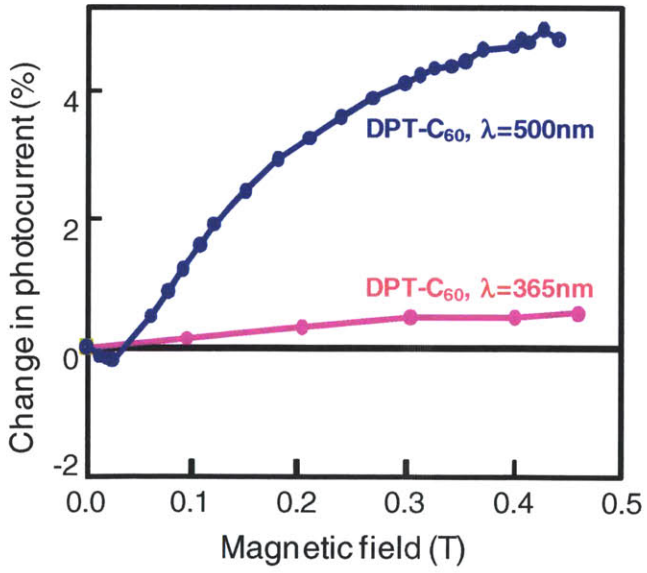

Figure 7.7 Change in photocurrent with magnetic field as a function of wavelengths

To confirm our hypothesis we substitute the acceptor C_{60} with a different material with a much lower LUMO level, hoping to reduce the CT energy. We use F_{16}CuPC which has a LUMO level of 4.8ev,[105] much lower than C_{60} LUMO at 4.0eV,[106] so we expect $E_{CT,\ DPT\text{-}F16CuPC}$ to be much lower than $E_{CT,\ DPT\text{-}C60}$ and hence allow the DPT triplets to form CT states at the DPT-F_{16}CuPC interface. Figure 7.8 has the three devices that we use in our analysis: Tetracene-C_{60}, DPT-C_{60} and DPT-F_{16}CuPC.

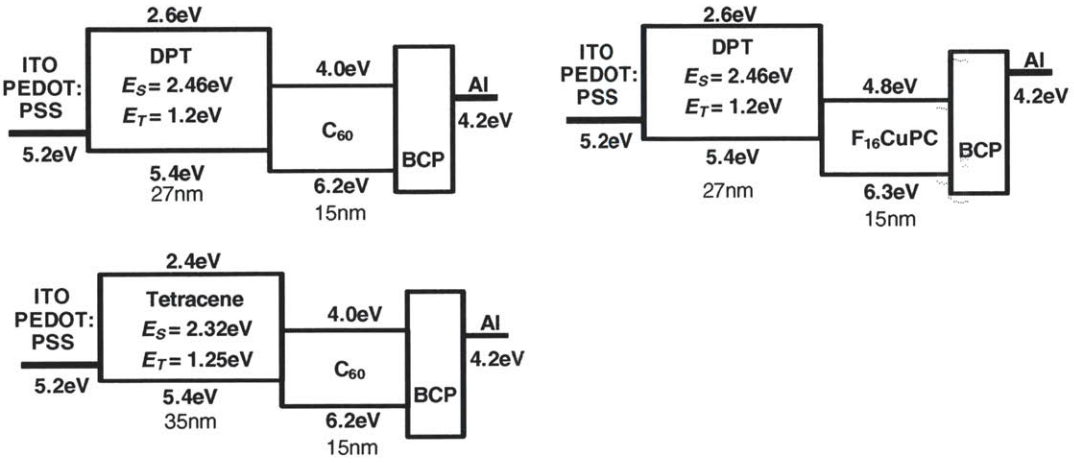

Figure 7.8 Structures of the three devices used to investigate the anomalous magnetic field effect

The magnetic field effect for the three devices is shown in Figure 7.9. We see the tetracene-C_{60} device has the usual negative effect of ~-2% at 0.5T. And the DPT-C_{60} device shows the anomalous +5% at 0.45T.

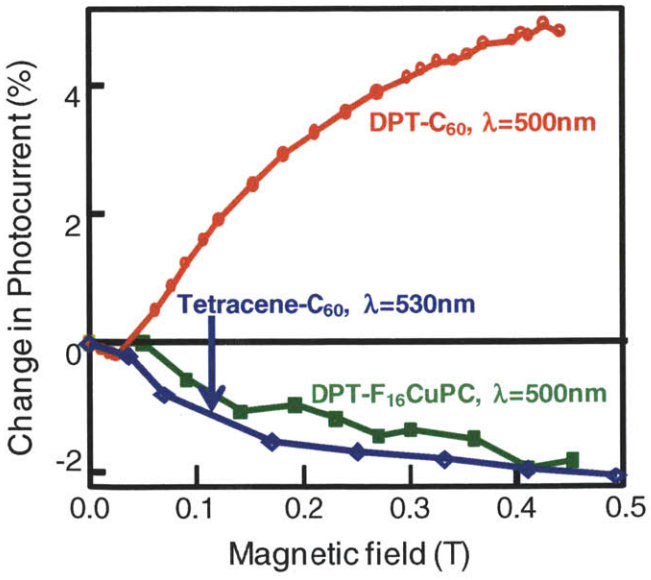

Figure 7.9 Magnetic field effect on the tetracene-C_{60} , DPT-C_{60} and DPT-F_{16}CuPC devices

In the DPT-F_{16}CuPC device we see again the familiar negative maximum photocurrent change of -2% at 500nm at the DPT absorption peak. At 660nm where F_{16}CuPC has strong absorption,[107] we saw a small effect of .15% which could be due to charge recombination effects.[108]

It is interesting to note the large difference in the magnitude of the magnetic field effect in DPT and tetracene devices,[100] considering that the neat films show approximately the same behavior. We did some calculations to a first approximation by assuming the proportional change in the singlet yield in the neat film and in the device on the application of the magnetic field to be equal. From the change in the photocurrent, we deduce that not more than 10% of triplets in the DPT device contribute to current. A part of the remaining triplets can undergo TTA, but the rest will decay to the ground state. This explains the large change in the photocurrent in the DPT device compared to the tetracene device, since the change is now a proportion only of singlet current which is small, rather than triplet and singlet current as it is in the tetracene device.

In the tetracene-C_{60} multilayer structure of chapter 0 we found that out of all the generated excitons that lead to current, 28% singlets became CT states directly and 72% became triplets. Following the same calculation as above, we find that the triplet contribution to current in the device is approximately 50% higher than the triplet yield in the neat tetracene film. In the multilayer structure where the charge generating interface is very close to every exciton, it is likely that the triplets form CT states before they decay as they would in a neat film.

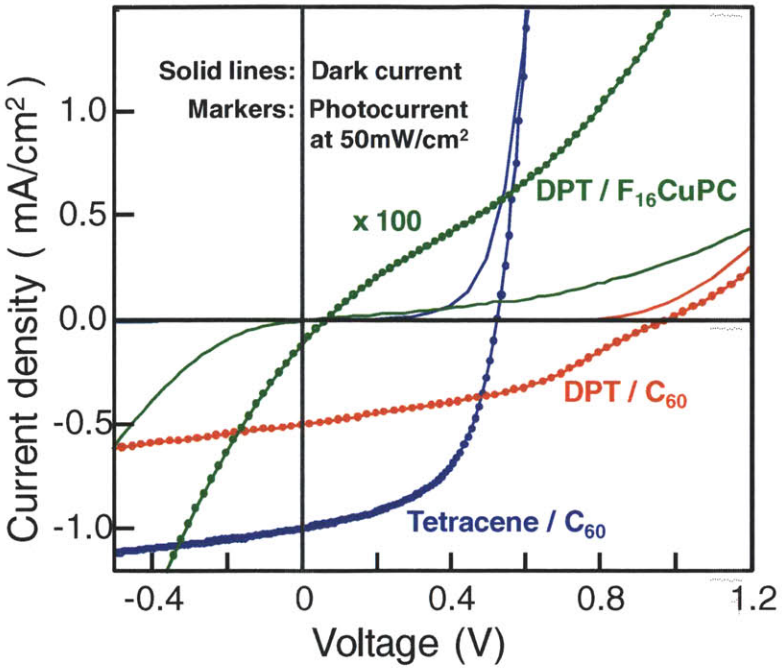

Figure 7.10 Current-voltage characteristics for the three devices

In general, for organic semiconductor photovoltaics, it is understood that $V_{OC} \sim E_{CT}$ -0.5V.[36, 109] The approximate E_{CT} values that we can infer from the V_{OC} data for the three devices from this relation agrees with the analysis in the previous section. The DPT-C_{60} device has a high V_{OC} of .975V and hence high E_{CT} compared to tetracene-C_{60} device with a V_{OC} of .53V. This does suggest that the tetracene triplets with an energy of 1.25eV can dissociate at the device interface but that the DPT triplets do not even though the DPT triplet energy at 1.2eV is a close to the tetracene value. In DPT-F_{16}CuPC, the LUMO of the acceptor is less than the C_{60} LUMO by 1.2eV. This results in a substantially lower E_{CT}, reflected in a low V_{OC} of .06V, and now the DPT triplets can dissociate at the charge generation interface resulting in a negative magnetic effect in the device.

7.4 An Isotropic Magnetic Field Detector

The strong magnetic field effect in this device can be exploited in a magnetic field detector above .05T, where the effect becomes monotonic. The effect has some directionality in a crystal,[110] but in the polycrystalline thin film, the directionality is averaged out and the device can be used as an isotropic detector. Biasing the device at V_{oc} maximizes the effect. The results of this approach are shown in Figure 7.11. Since the base current is almost zero, the application of a magnetic field results in a large signal

change. Since the processes involved operate in the nanosecond or shorter timescale the device should be operable at GHz speeds.

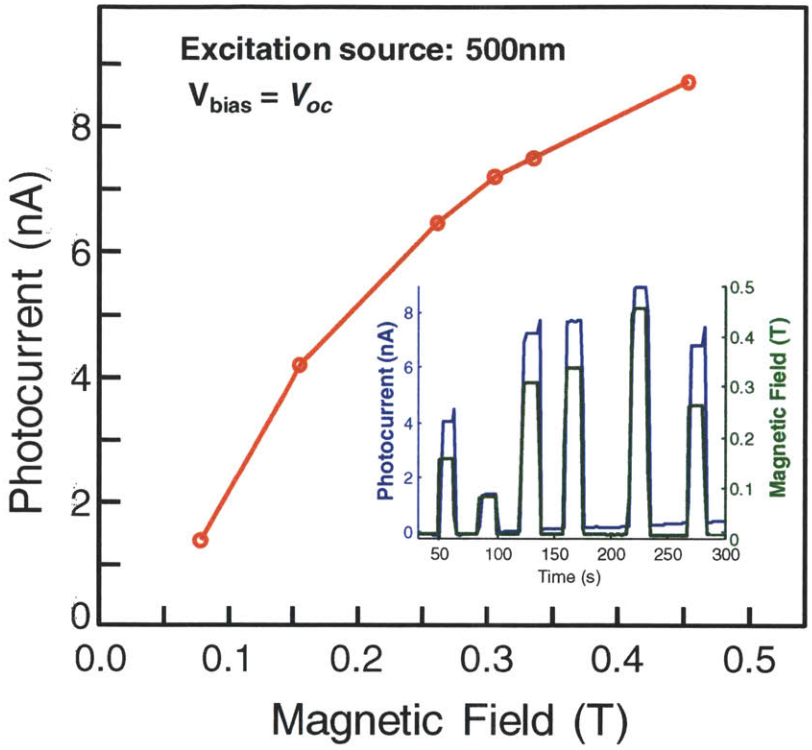

Figure 7.11 Photocurrent as a function of magnetic field in the DPT-C_{60} device biased at Voc. The inset shows the photocurrent and magnetic field traces as a function of time. The spikes in the photocurrent at the end of each pulse are an experimental artifact.

To conclude, we found that the dependence of photocurrent on the magnetic field provides an important probe into the singlet exciton fission yield and the dissociation of singlet and triplet excitons within organic semiconductor devices. In particular, differences between the magnetic field effect on fluorescence and photocurrent can be used to distinguish the inability to dissociate triplet excitons at donor-acceptor interfaces. We also show a large, magnetic field-dependent variation in photocurrent for solar cells biased at their open circuit. This may be employed as an isotropic magnetic field detector.

8 Low energy gap quantum dots as electron acceptors singlet exciton fission solar cells

We saw that singlet exciton fission can enhance the efficiency of organic photovoltaics only if the fission material is paired with an absorptive low-energy-gap material. Unfortunately, conventional fullerene-based acceptors are not suited for absorption at long wavelengths. Pentacene, tetracene, and their acene-based derivatives, which are presently the most efficient singlet fission materials,[48, 49] have triplet energies of ~0.86eV and ~1.25eV respectively. Fullerenes absorb most strongly in the blue-green part of the spectrum and very weakly at these energies in the infrared.

Poor long-wavelength absorption by fullerenes has meant that previous singlet exciton fission-based solar cells have required a third material to absorb in the red and near infrared as we saw in chapter 6.[111] This complicates the structure, because excitons from the long-wavelength absorber must find their way to the donor-acceptor junction formed between the acene material and the fullerene. It would be preferable to replace the acceptor with a long-wavelength absorber and remove the requirement for an additional material.

In this work, we fabricate hybrid organic/inorganic photovoltaics using pentacene, a singlet fission material, as the donor, and infrared-absorptive lead chalcogenide quantum dots as the acceptor. We find that pentacene triplet excitons dissociate at the pentacene/quantum dot heterojunctions with an internal quantum efficiency of 35%. The simple donor-acceptor structure is a significant advance over previous three-component fission-based organic photovoltaics, since it should enable the fabrication of single-layer solution-processed bulk heterostructures.

QDs have previously been used with organic semiconductors both as acceptors [112] and as donors[113]. Thick PbS and PbSe QD films have also demonstrated high power conversion efficiencies without organic layers.[114] QDs can be tuned with optical absorption in the near infrared[115, 116] and electron energy levels sufficient to dissociate triplet excitons from pentacene, while also demonstrating good electron mobilities,[117] and compatibility with solution processing.

8.1 Quantum dots overview

Quantum dots (QD) or nanocrystals are crystalline nanoparticles whose radius is smaller than the exciton Bohr radius in the bulk crystal, causing discrete energy levels to appear above the band gap of

the bulk crystal. See Figure 8.1. Changing the diameter of the quantum dot changes the energy levels resulting in tunable absorbers and emitters that can be used in QD LED and in photovoltaics.

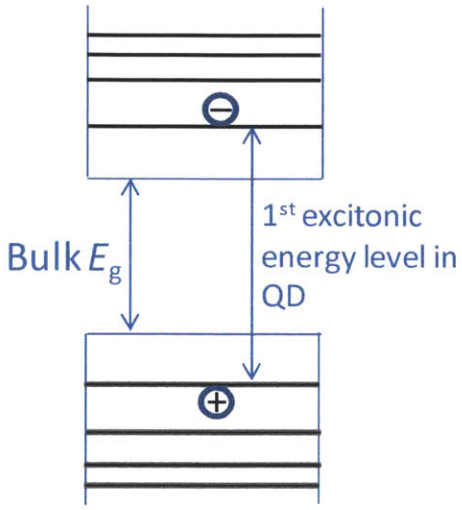

Figure 8.1 Bulk band gap and discrete energy levels in the quantum dots

Colloidal quantum dots are synthesized from a liquid phase and end up with passivating organic ligands on the surface usually suspended in a solvent. The advantage is that they can be solution processed into devices. They are uslaly two material systems like PbS, PbSe, CdTe CdSe etc. For absorption in the infrared, the material to be used should have a low enough band gap, and a large enough Bohr radius (> 5nm) so that the confinement pushes up the energy levels in the QD to an energy which is still low enough to be interesting. Pb(S, Se, Te), In(Sb, As), SnS and FeS_2 are good candidates. [118] For example PbS has a bandgap of 0.37eV in the bulk crystal and an excitonic Bohr radius of 18nm.[119] PbSe has a bandgap of 0.27eV in the bulk crystal and an excitonic Bohr radius of 46nm.[120] Quantum dots can also be epitaxially grown onto semiconductor substrates. In this work we use colloidal quantum dots.

Synthesis

Colloidal quantum dots are usually synthesized by mixing precursors of the two materials and the organic ligands and at a certain temperature. Synthesis conditions can be used to tune the size of the dots. For example, for the PbS dots used in this work, the sulphur precursor hexamethyldisilathiane (TMS2-S) in a solvent was injected into a solvent that had the lead precursor Lead(II) acetate trihydrate (PbAc), and the ligand compound oleic acid (OA) at a temperature of 150C. This resulted in PbS QD with Oleic acid ligands. The reaction synthesis time and temperature can be used to control the size of the QD.

Ligands

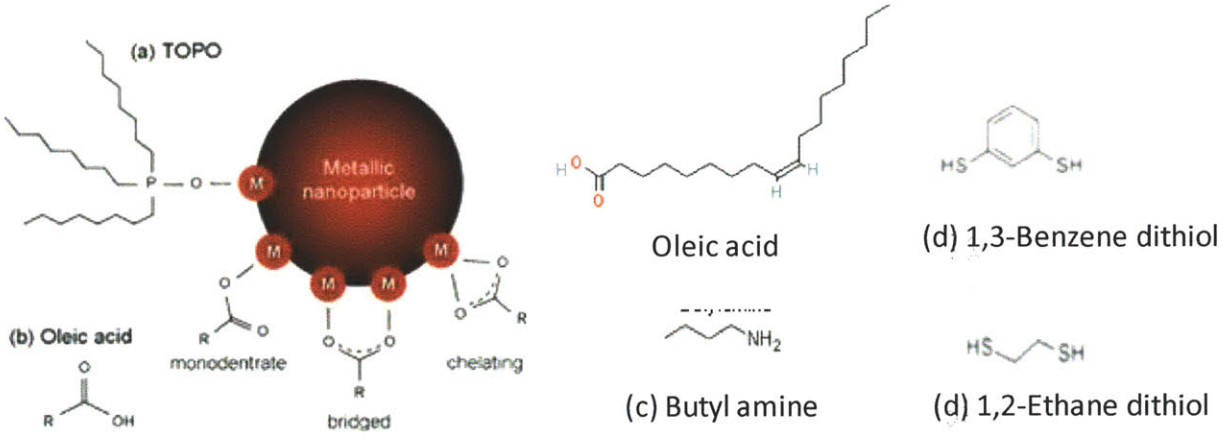

Figure 8.2 Various ligands used to passivate QD . TOPO and Oleic acid attachments from ref[121]

Various organic ligands are used to passivate QD as well as keep them suspended in some solvents. Oleic acid is commonly used in the synthesis process of PbS and PbSe dots and is 2nm long. Butyl amine is shorter at 0.5nm. 1,3-Benzene dithiol, 1,2-Benzene dithiol (BDT) and 1,2-Ethane dithiol (EDT) are linkers and the S atoms connect to a QD each thus linking two QD. Substitution with linkers is usually done after spin coating into a thin film because this makes the film insoluble, and subsequent spins do not remove the deposited film. In this work we use BDT linkers. Recently atomic ligands, Cl^-, Br^- and I^-, have been used on PbS QD to get better mobilities than reported before.[117]

Mobility

The charge carrier mobility of QD is affected by the size, ligands, and the material system. The larger the dots the higher the mobility since there are fewer hops for the charge carrier to make to traverse a distance. See Figure 8.3(a). Shorter ligands usually have higher mobility. Some data is shown in Figure 8.3 (b) for EDT and BDT linkers and discussed below.

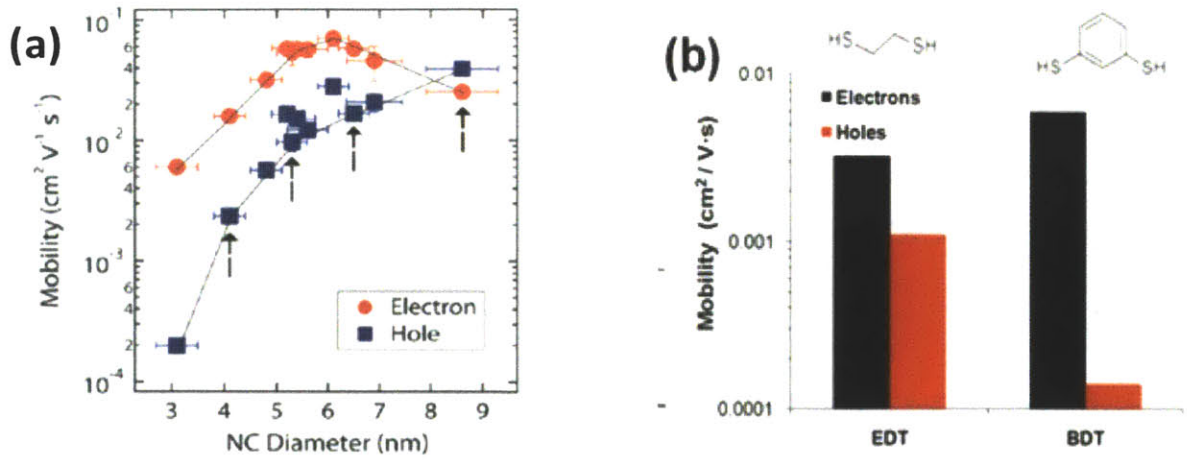

Figure 8.3 (a)Variation of mobility in PbSe nanocrystals with size. [122] (b) The mobility in 1050nm to 1600nm band gap PbS nanocrystals eith EDT and BDT linkers. Taken from ref [123].

PbS dots of band gap 1150nm with 1,3-Benzene dithiol (BDT) linkers have shown electron mobilities of 2.4 x 10^{-4}cm^2/Vs and hole mobilities of 8.5 x 10^{-6}cm^2/Vs. The same dots with 1,2-Ethane dithiol (EDT)have shown electron mobilities of 5.1x 10^{-4}cm^2/Vs and hole mobilities of 6.3 x 10^{-4}cm^2/Vs.[124] Benzenedithiol is in fact a molecular conductor in view of its delocalization of electron molecular orbitals.[125]

TOF (Time of Flight) measurements find in PbSe dots of band gap 1250nm (3.6nm diameter), the electron mobility to be 1.4 × 10^{-3} cm^2 /Vs with BDT linkers, and CELIV (Charge Extraction by Linearly Increasing Voltage) measurements find hole mobility to be 2.4 × 10^{-3} cm^2 /Vs.[126]

Dielectric constants

The dielectric constants of QD are generally lower than their constituent materials in the bulk form. The relative dielectric constants in bulk crystal for PbS and PbSe are 169 and 210 respectively.[127] For QD of bandgap 0.5eV to 1.5eV it has been measured to be 14.5±1.8 for PbS and 21.0±2.5 for PbSe, with no dependence on size.[128]

8.1.1 Schottky Devices

A Schottky device is a simple structure as shown in Figure 8.4. It is generally made on a glass substrate with Indium Tin Oxide(ITO) as the anode, with a p-type PbS or PbSe QD layer and a low work function metal like Aluminum as the cathode. The ITO forms an ohmic junction with the p-type QD layer, and the

cathode forms a Schottky junction with the p-type layer. The depletion width can extend up to 150nm. Schottky devices have reached up to an efficiency of 4.6%.[129] The excitons generated in QD layers have almost no binding energy and immediately split into electrons and holes. The electrons and holes are swept to their respective electrodes by the electric field in the depletion width of the device. The Schottky junction will also be part of the singlet fission – QD device that we fabricated in this work and which we discuss next.

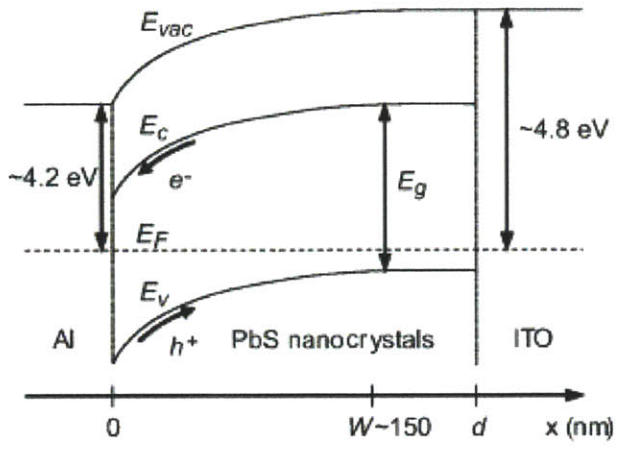

Figure 8.4 A Schottky device energy diagram. From ref [130].

8.2 Device Fabrication

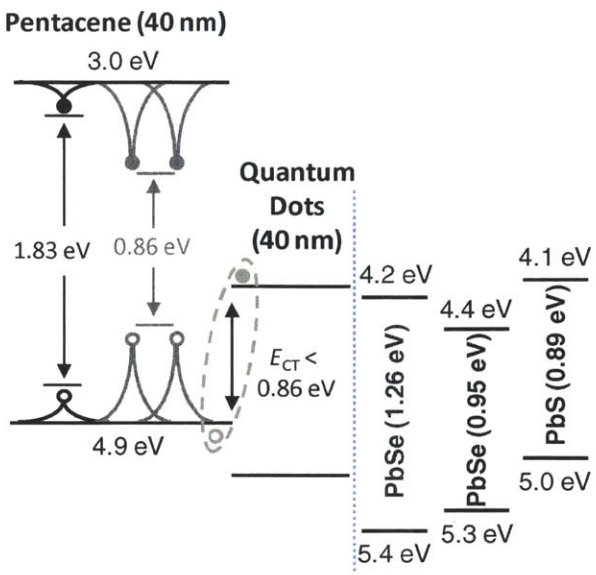

Figure 8.5 Singlet exciton fission dynamics a heterojunction consisting of pentacene and PbSe or PbS quantum dots (QDs). The singlet exciton in pentacene splits into two triplet excitons with approximately half the energy of the singlet exciton. The HOMO and LUMO levels of pentacene are indicated and compared to the energy levels of electron and holes in the various QDs employed here.[115, 116] These energy levels do not consider any charge transfer that may occur at the interfaces. Triplet dissociation at the pentacene/QD interface requires that the charge transfer state energy (E_{CT}) be less than or approximately equal to the energy of the pentacene triplet.

Figure 8.5 shows the device structure employed in this work to characterize pentacene-QD devices and the energy levels of the materials used.[115, 116] Devices were fabricated on precleaned glass substrates coated with indium tin oxide and poly(3,4-ethylenedioxythiophene): poly(4-styrenesulphonate) (PEDOT:PSS). A 40-nm-thick layer of pentacene was deposited by thermal evaporation in a vacuum chamber with a base pressure of 3×10-6 Torr. The oleic acid-capped quantum dots were obtained from Ocean Nanotech (PbSe) or synthesized in-house via standard literature methods (PbS), washed by precipitation and centrifugation in acetone and 1-butanol, dissolved in octane at a concentration of 25mg/ml, and filtered (0.02 μm PTFE).[113] The quantum dot films were deposited in a layer-by-layer process from a solution of 25mg/ml in octane via sequential spin casting described elsewhere.[131] For each layer, approximately 20 μL of quantum dot solution was spun-cast at 1500rpm for 15s; 200μL of 1.7mM 1,3-benzenedithiol (BDT) in acetonitrile was then dropped onto the film and allowed to sit for 30s before spinning off. Three 5s washes with acetonitrile were then performed to remove excess BDT, and the process was repeated. Two cycles resulted in a quantum dot

film thickness of roughly 40nm.Two layers resulted in a quantum dot film thickness of roughly 40nm. An aluminum cathode was thermally evaporated and the device was encapsulated in a nitrogen environment. We also made control devices with no pentacene layer but the same anode and cathode. These devices are believed to generate photocurrent through field dissociation of excitons within the Schottky-junction-induced depleted region between the QD material and the aluminum cathode.[132]

8.3 Characterization

The external quantum efficiency (EQE) measurements for the devices described above are shown in Figure 8.6. The characteristic absorption peaks of pentacene from 500-700-nm range appear in the EQE spectra. The QDs are observed to absorb most strongly in the 400-500-nm range but contribute to photocurrent into the near infrared beyond wavelengths of 700 nm. The device with PbSe (1.26eV) shows the best performance with an EQE from 30-25% in the 400-700-nm range. The dotted lines show the EQE for the corresponding Schottky devices.

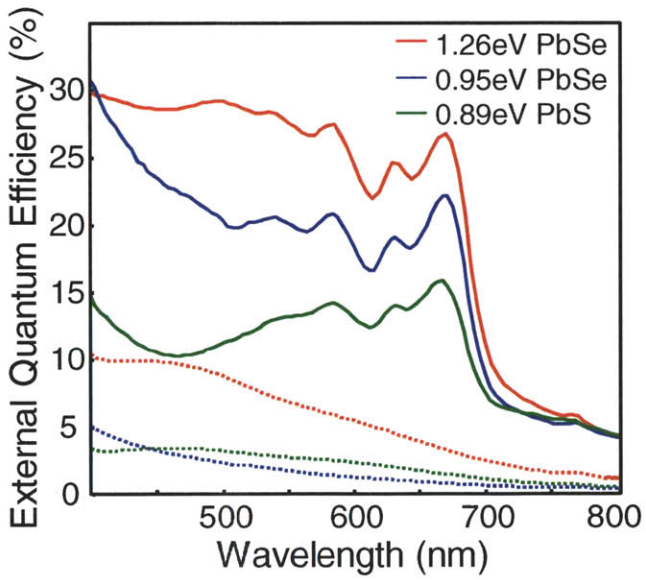

Figure 8.6 Spectrally-resolved external quantum efficiency, defined as the ratio between the number of photoelectrons generated under short circuit conditions and the number of incident photons. The solid lines correspond to pentacene/QD photovoltaics employing three different QD energies, and the dotted lines show the external quantum efficiencies for the corresponding control devices fabricated without pentacene.

The internal quantum efficiencies (IQE) in the pentacene-PbSe (1.26eV) device were determined by modeling the optical absorption using the transfer matrix method.[86] The results are shown in Figure 8.7. A similar analysis is done for a conventional donor-acceptor junction device consisting of pentacene and C_{60}. Pentacene exhibits an IQE of 35% in the QD-containing device and 63% in the C_{60}-containing device. The IQEs of the QDs and C_{60} are both approximately 42%. We assume that triplet generation and diffusion is similar in both pentacene films. It is possible that exposure to solvents or contamination during ligand exchange partially damages the pentacene/QD interface. It may be possible to optimize solvents and the ligands on the QDs at the interface for closer contact with the pentacene surface.

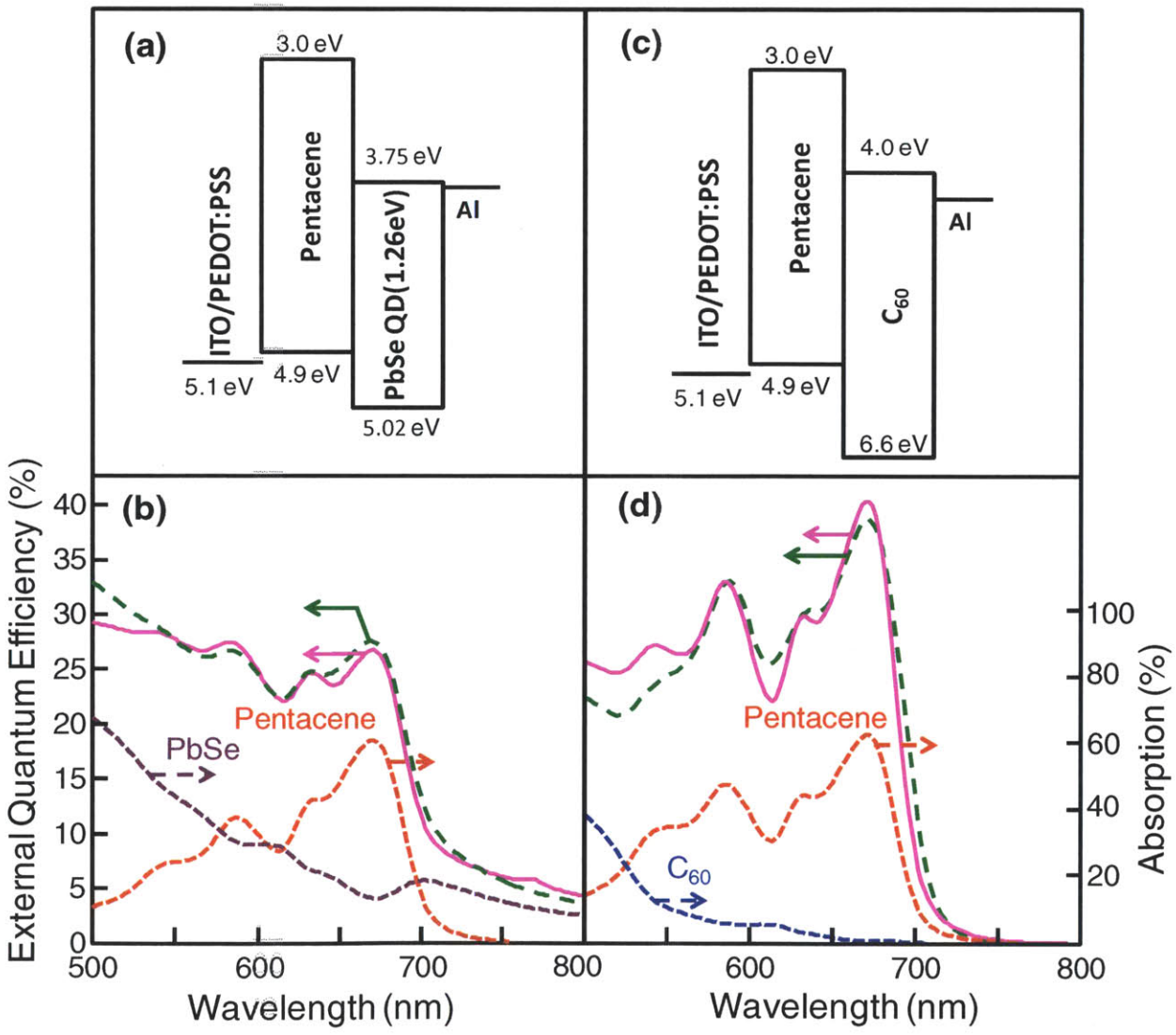

Figure 8.7 **a**) & (**c**) Structure of pentacene/PbSe (1.26 eV) device investigated and a control pentacene/C_{60} device **(b)** & **(d)** Calculated and measured external quantum efficiencies for a pentacene-

PbSe (1.26 eV) device and a pentacene-C_{60} device, each with a 40-nm-thick film of pentacene. The donor-acceptor interfaces are characterized by their internal quantum efficiencies (IQEs), defined as the ratio between the number of photoelectrons generated under short circuit conditions and the number of absorbed photons. The IQE of pentacene in the pentacene/PbSe (1.26 eV) device is 35%, compared to 63% for pentacene in pentacene/C_{60} interfaces.

Figure 8.8 presents the current-voltage characteristics of devices described in Figure 8.5 and Figure 8.7. We find a lower shunt resistance in the Schottky devices that lack the pentacene film at the anode, suggesting that the pentacene acts as an electron blocker. The open circuit voltages for the pentacene/PbSe devices with QD band gaps of 1.26 eV (PbSe), 0.95 eV (PbSe), and 0.89 eV (PbS) are 0.46 V, 0.39 V, and 0.42 V, respectively. These open circuit voltages are higher than previously reported values for Schottky devices with similar materials: 0.37V, 0.21V[132] and ~0.17V,[133] respectively for the three types of dots. The last is a comparison with a 0.926eV ban dap PbS dots device, but we would expect a 0.89eV band gap device to have a lower open circuit voltage. The values are also higher than the open circuit voltage of 0.36 V observed in pentacene/C_{60} devices.[134]

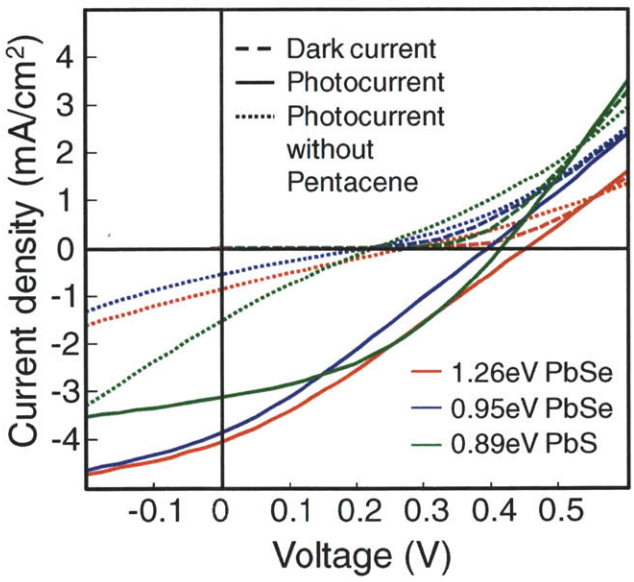

Figure 8.8 Current-voltage characteristics of the pentacene/QD and QD-only devices taken under AM1.5 illumination with intensity of 50mW/cm2

8.4 Analysis of results

The rate of singlet exciton fission into triplets is very high at 1.3×1013s−1 in pentacene[49] and the EQE exceeds 100% in a pentacene-C60 multilayer photodetector structure with pentacene layer thicknesses of only 2 nm.[81] In the bilayer devices presented here, with a pentacene thickness of 40 nm, the majority of excitons that reach the pentacene/QD interface are therefore expected to be triplets rather than singlets, ruling out singlet CT state dissociation as the cause of the EQE increase observed in Fig. 8.5. We can also rule out energy transfer from the pentacene triplet to the QDs, since all the QDs used here have band gaps equal to or greater than the pentacene triplet energy.

8.5 Quantum Dots Size dependence

Confirmation that the pentacene-QD interface dissociates pentacene triplet excitons is shown in Figure 8.9. Here, we plot the measured EQE of pentacene/PbS devices as a function of the QD energy. These devices were fabricated with the same structure and procedure described previously. For the devices containing QDs with band gaps from 0.89eV to 1.08eV, the presence of pentacene absorption peaks in the EQE indicates that pentacene contributes positively to the photocurrent. For the device employing 1,37ev and 1.48eV QDs, the EQE instead decreases at the pentacene peaks, indicating that the triplets are unable to dissociate at the heterojunction and do not contribute to the photocurrent; the pentacene absorption therefore reduces the amount of light reaching the PbS active layer, limiting the EQE. As seen in Figure 8.9(b), as the energy of the QDs increases, the CT state energy at the pentacene/QD interface also increases until it is higher than the pentacene triplet energy. The fact that this transition occurs when the QD band gap is already greater than the triplet energy further indicates that the pentacene contributes to the photocurrent through triplet CT state dissociation rather than energy transfer.

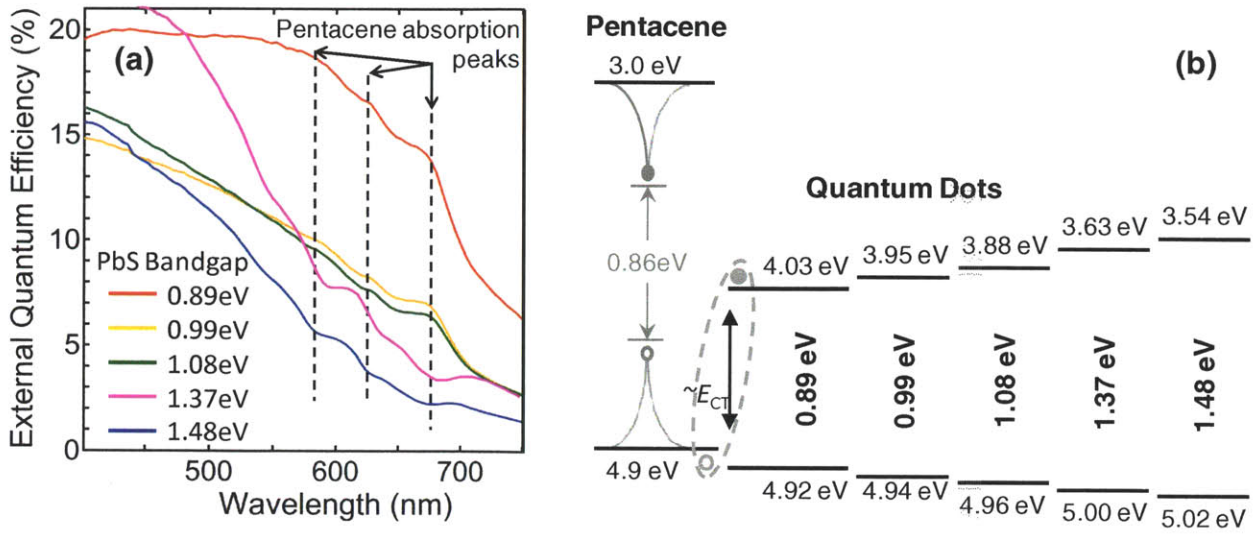

Figure 8.9 (**a**) External quantum efficiencies for a series of pentacene/QD devices with PbS quantum dots of various band gaps. The contribution of pentacene is positive for QD band gaps of 0.89eV, 0.99eV, and 1.08eV, and negative for a QD band gap of 1.37eV and 1.48 eV. **(b)** Energy band diagrams of the materials used here.

In conclusion, we have demonstrated the fabrication of hybrid organic/inorganic photovoltaics that exploit singlet exciton fission paired with QD-based acceptor. The ability to tune the band gap of QDs can be used to create an energetically ideal pairing for singlet exciton fission in photovoltaics. QD-based acceptors also simplify the device structure from three to two components. It is challenging to control the morphology of three component donor-acceptor junctions; thus, this simplification, together with the pending development of soluble exciton fission materials, should allow the fabrication of conventional single layer bulk heterostructures. More broadly, we find that lead chalcogenide dots may provide an alternative to conventional fullerene acceptors, should the large scale synthesis of fullerenes prove challenging.

8.6 PbS Quantum Dots Synthesis

This synthesis procedure is from ref [113].

Materials used:

Lead(II) acetate trihydrate (PbAc), oleic acid (OA), hexamethyldisilathiane (TMS2-S), 1-octadecene (ODE), hexane, methanol, butanol, butylamine, ethanedithiol (EDT), and acetonitrile (all solvents are

anhydrous) were purchased from Sigma-Aldrich and used as received. PCBM was purchased from American Dye Source Co. and used without additional purification.

Quantum Dots Synthesis and Ligand Exchange:

The lead precursor was prepared by dissolving and degassing 11.380 g of PbAc in a mixture of 270 mL of OA and 30 mL of ODE at 100 °C. After the lead precursor was made, the solution was heated to 150 °C under argon, followed by the swift injection of the sulfur precursor formed with 3.15 mL of TMS2-S and 150 mL of ODE. After synthesis, the QDs were purified and extracted with a mixture of methanol and butanol and then redispersed in hexane. Finally, the QDs were washed twice with methanol and stored as a powder.

The ligand exchange was performed inside a nitrogen glovebox by dispersing the OA capped QDs in butylamine. After 3 days, the QDs were precipitated with methanol and redispersed in octane to achieve a typical concentration of 75 mg/mL.

9 Donor-acceptor interface energetics in singlet exciton fission photovoltaics

In the last two chapters we developed two methods to probe triplet dissociation at the heterojunction in singlet fission photovoltaics. One is the magnetic field probe and the other is to vary the energy of the acceptor LUMO or donor HOMO and change the charge transfer state (CT) energy and hence affect the triplet dissociation. In this work we use these methods, as well as results from a series of acceptors to find a suitable acceptor for singlet fission photovoltaics. We looked at C_{60}, Perylene diimides, PbS quantum dots and PbSe quantum dots, paired with pentacene and 6,13-Diphenyl pentacene (DPP) as donors.

9.1 Acceptors and Donors under consideration

9.1.1 Donors

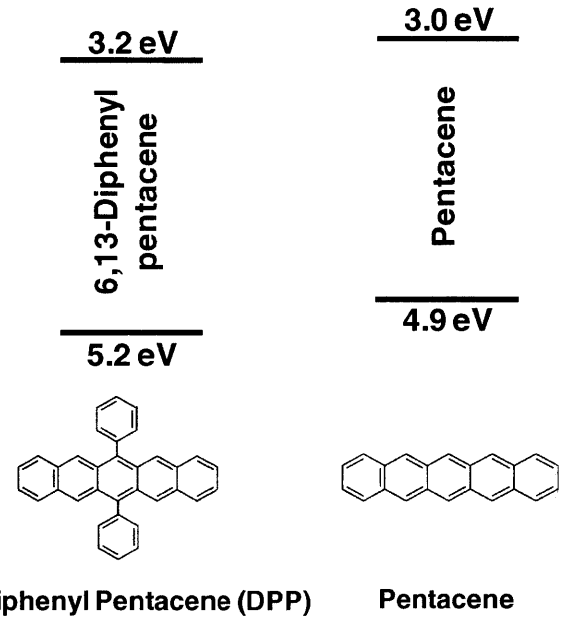

Figure 9.1 The donors used in this work. The energy levels are from refs [135] and [136, 137]

In chapter 8 we varied the LUMO level of the acceptor, the PbS quantum dots, to change the CT energy. Here we also use the HOMO level of the donor to change the CT energy. DPP has a slightly deeper HOMO level at (5.2±0.1)eV, [135] compared to pentacene at (4.9±0.1)eV. [136, 137] See **Figure 9.1**. The triplet energy for the two materials is expected to be the same because the pendent phenyl groups in DPP are perpendicular to the acene core preventing delocalization of the pi-orbitals over the additional

phenyl group. Hence the electron density is concentrated on the acene core just like in pentacene resulting in similar triplet energies.

9.1.2 Small Molecule Acceptors

Just like the photocurrent from a tetracene- C_{60} device showed a negative magnetic field effect and a diphenyl tetracene (DPT)- C_{60} device showed a positive magnetic field effect, a similar phenomena was observed with pentacene and DPP. The pentacene-C_{60} interface could dissociate triplets and the DPP-C_{60} interface could not. Hence we deduce that DPP-C60 forms a higher energy CT state than pentacene-C_{60} possibly because of the slightly deeper HOMO level at (5.2±0.1)eV[135], compared to pentacene at (4.9±0.1)eV[136, 137]. It is also possible that the additional phenyl rings in DPP push it further from the C60 molecule thus raising the CT energy.

So in addition to C_{60}, we use two other small molecule acceptors, perylene diimides, which have lower LUMO levels. Now the CT energy should be low enough such that triplets from DPP can dissociate at the interface between DPP and the new acceptors. The molecular structures and the energy levels of the small molecules explored is given in **Figure 9.2**.

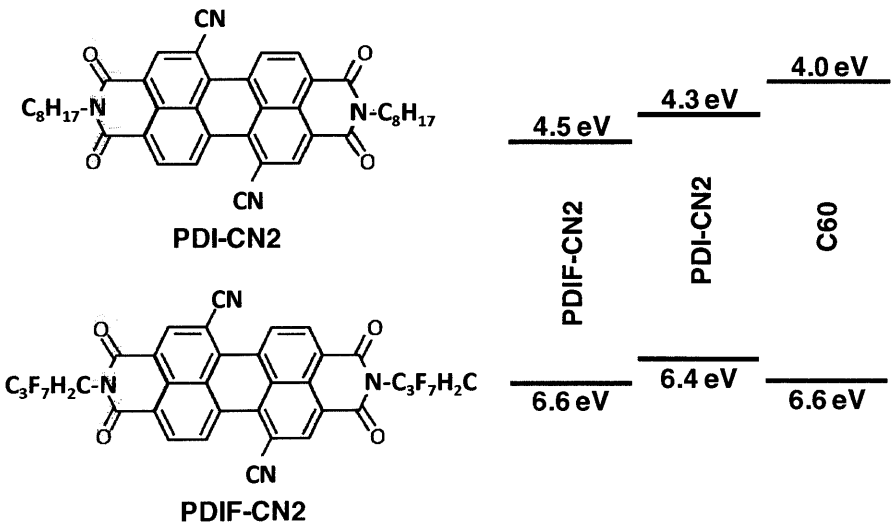

Figure 9.2 Molecular structures and energy levels of the small molecule acceptors investigated. The energy levels for the perylene diimides is taken from the vendor Polyera's website.

9.1.3 Quantum Dot acceptors

The QD acceptors and data is the same as dealt with in chapter 8 but the energy levels for the devices being considered are given in 9.1.3 again.

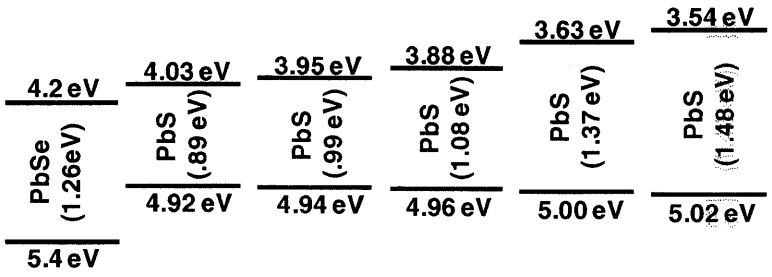

Figure 9.3 Energy levels for QD being considered as acceptors

9.2 Small molecule acceptors

9.2.1 Magnetic field effect

We use the magnetic field probe developed in chapter 7 to investigate triplet dissociation in the three devices indicated in **Figure 9.4**. As can be seen from this data, the DPP-C_{60} devices does not dissociate triplets, but the DPP-PDIFCN2 and the Pentacene- C_{60} do.

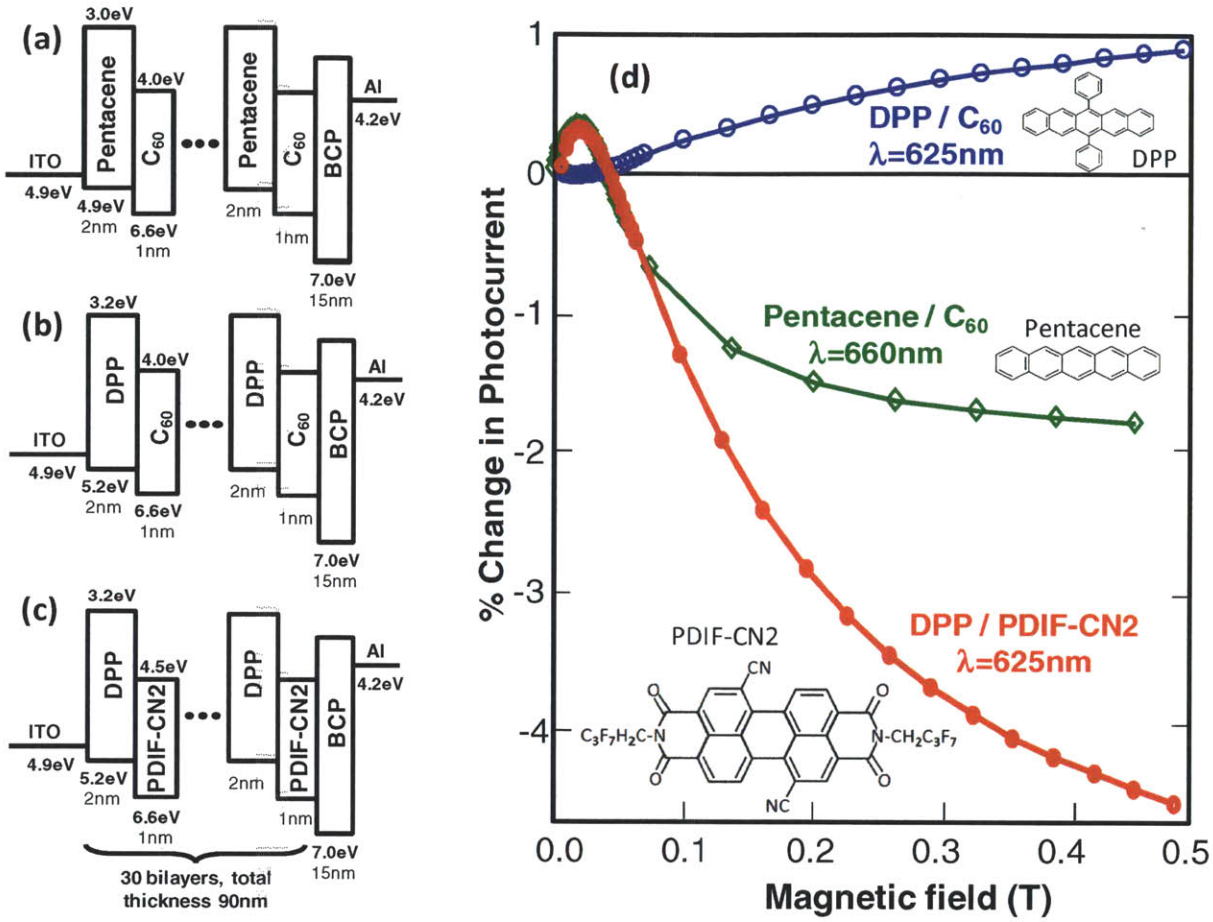

Figure 9.4 Device structures and magnetic field effect on photocurrent for a series of small molecule acceptor – pentacene or DPP donor devices.

9.2.2 Device performance

The small molecule devices were characterized by External Quantum Efficiency (EQE) measurements – shown in **Figure 9.5**, and current voltage characteristics shown in **Figure 9.6**.

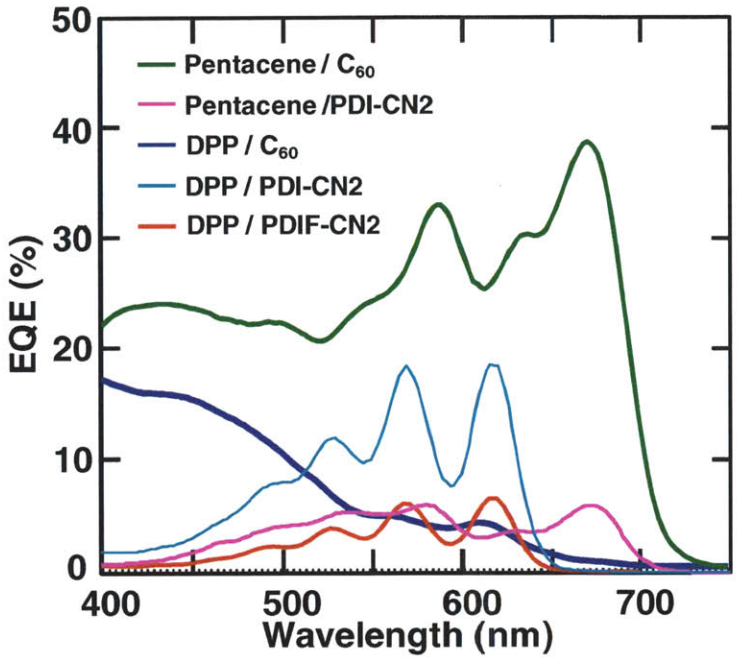

Figure 9.5 Measured External Quantum Efficiencies for the devices investigated.

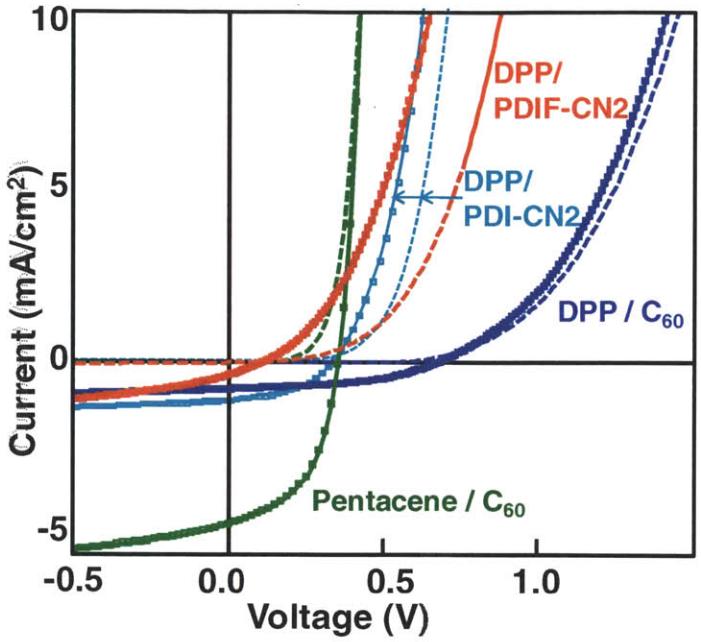

Figure 9.6 Current-voltage characteristics of the devices under consideration

Optical modeling using the transfer matrix method was used to calculate the absorptions in the various layers of the devices and thence to calculate the Internal Quantum Efficiencies (IQE) by generating fits to the measured EQE. The calculated IQE and V_{oc} are show in Table 9.1.

Table 9.1 Calculated IQE and measured V_{oc}

Device	IQE	Voc
Pc-C_{60}	63,42	0.36
DPP-PDICN2	40,11	0.36
Pc-PDICN2	16,13	0.02
DPP-PDIFCN2	13,2	0.13
DPP-C_{60}	4,36	0.70

IQE values deduced from the calculations show that the pentacene-C_{60} device shows the highest acene IQE of 63%, and a C_{60} IQE of 36%. The DPP- C_{60} device shows the same C_{60} IQE of 36% and a low DPP IQE of 4%, indicating that the DPP contribution is very poor. Since the major current contribution in a bilayer device has to come from triplets, the inability of triplet dissociation results in a low EQE. In the DPP - PDIFCN2 device, since the triplets can dissociate, the DPP contribution is three times higher at 12%. The poor overall performance of the device indicated by the low IQE of the acceptor at 2% explains why the contribution of DPP s still low compared to pentacene in the pentacene-C60 device. The performance of PDICN2 seems to be a better and hence the IQEs for the donor and acceptor in the DPP-PDICN2 device are higher at 40% and 11%. It is notable that neither PDI nor PDIF-CN2 is a strong source of photocurrent.

9.3 Quantum dot acceptors

We analyze here the data and results from chapter 8. The PbS devices show much lower performance compared to the PbSe devices and hence we neglect the IQE calculation. Out of the PbSe devices we consider the Pentacene-PbSe(1.26eV) device from Figure 8.7. Pentacene exhibits an IQE of 35% and PbSe QD an IQE of 42%.

9.4 Summary of interface energetics

To get a better insight into the energy levels involved, we collate in **Figure 9.7**, the triplet dissociation result for all devices discussed in this work. Plotted on the y-axis is a quantity that is reflective of the CT energy, which is the difference in energies of the acceptor's LUMO and the donor's HOMO. The quantity $E_{LUMO,\,acceptor} - E_{HOMO,\,donor}$ does not consider the binding energy which may be few tenths of an eV. This would lower the CT energy, and may be lower in the QD systems which have a higher dielectric constant than organic semiconductors. As can be seen, all devices with CT energy below a certain value allow dissociation of triplets.

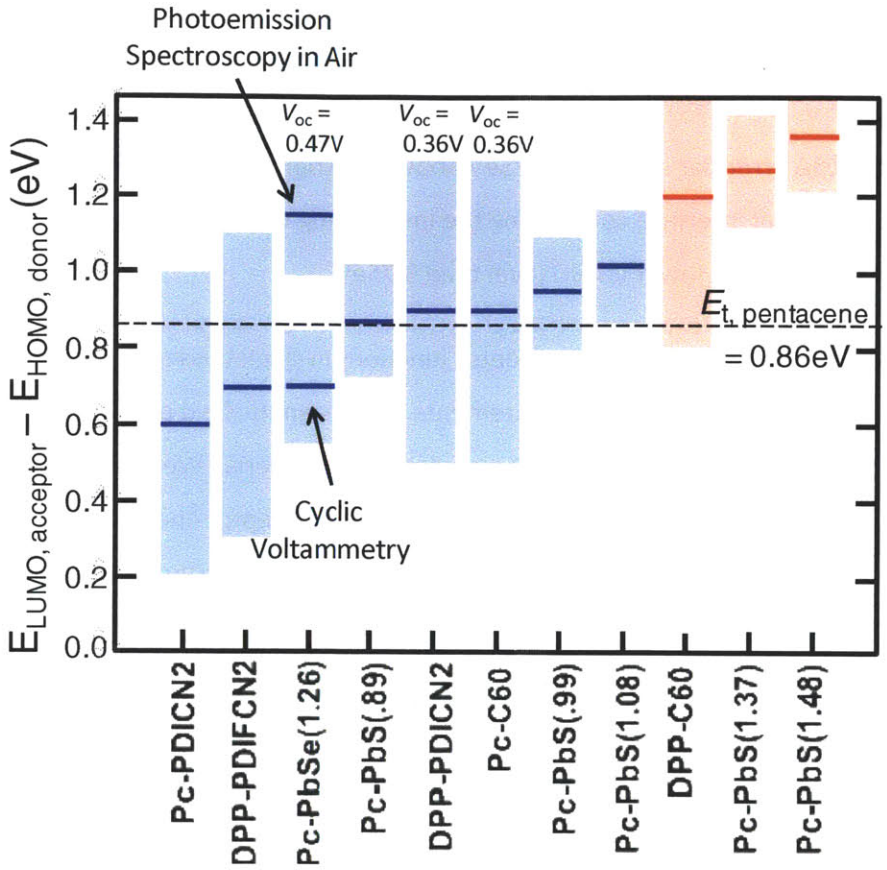

Figure 9.7 $E_{LUMO, acceptor} - E_{HOMO, donor}$ for various junctions. The blue dashes indicate that the device can dissociate the triplets of the singlet fission material, while the red dashes indicate the converse. The light blue regions and the pink regions indicate the error bars due to uncertainty in the values of $E_{LUMO, acceptor}$ and $E_{HOMO, donor}$. The Pc-PbSe(1.26) device is indicated by two different levels which represent $E_{LUMO, acceptor}$ measured through two different methods.

Overall, we find reasonable agreement between our observations of triplet exciton dissociation and our estimates of the CT energy at the donor-acceptor junctions. There are two notable discrepancies. When we exclude the binding energy of the CT state, we find that exciton dissociation at pentacene/C_{60} junctions is expected to be slightly endothermic. The temperature dependence of the magnetic field effect confirms this is not the case, suggesting that triplet exciton dissociation occurs at this interface due to Columbic stabilization of CT state. The other notable conclusion concerns the nanocrystalline acceptors. Given their high polarizability, these are not expected to exhibit CT states with large binding energies. Nevertheless, triplet exciton dissociation in many of these junctions is also predicted to be endothermic. The pentacene photocurrent in the PbS-based junctions is small at best and may rely on

size and energetic dispersity in the nanocrystals. PbSe jucntions, however, are relatively efficient. We quote two energies for the Pc-PbSe(1.26) device representing two LUMO measurements: (4.2±0.1) eV by cyclic voltammetry, and (3.75±0.1) eV by photoemission spectroscopy in air (PESA).[138, 139] The lower limit of the PESA error bar is at least 0.15eV above the triplet energy, which makes it unlikely for triplets to break up at that interface considering the low binding energy expected for a pentacene-QD interface. This implies a much lower LUMO level than 3.75eV.

In conclusion we have investigated donor-acceptor junctions in singlet fission structures using the magnetic field effect, and through EQE measurements. The magnetic field provides a clear probe to investigate triplet dissociation in thin layers of a singlet fission material. We find that pentacene/C_{60} interfaces are sensitive to small changes in either the donor or acceptor energy levels. Small changes, such as the use of the pentacene derivative DPP, prevent the interface from operating. The most promising donor-acceptor junction is pentacene/PbSe(1.26eV). This interface efficiently dissociates triplet excitons and also absorbs long wavelength light.

10 Summary and Outlook

In this thesis we have explored singlet exciton fission in organic semiconductor photovoltaics as a possible work around to the Shockley-Queisser limit. Singlet exciton fission moves the theoretical efficiency limit of 33.7% for single junction cells to 42%. We also explored triplet dissociation in singlet fission devices using the magnetic field effect and EQE measurements.

We implemented a tetracene-CuPC-C_{60} device, where the singlet fission material tetracene, and CuPC, were both donors, and C_{60} was the acceptor. For a singlet fission photovoltaic to be useful, a high band gap singlet fission material must be paired with a low band gap material. Since C_{60} is the only useful acceptor and it absorbs in the blue-green from 350-500-nm, which overlaps with tetracene, we add CuPC which absorbs in the red in the 500-800-nm range. The triplets from tetracene are shown to traverse through CuPC to the charge generating CuPC- C_{60} interface resulting in an EQE of 35-40%. The magnetic field effect on singlet fission is used to confirm the positive contribution to the device performance.

Singlet fission in tetracene is thermally activated. We use this property to do a low temperature External Quantum Efficiency (EQE) measurement to quantify the efficiency of singlet fission in a tetracene-C_{60} device and measured a value of 72% at room temperature.

We implemented a series of bulk heterojunction tetracene-C_{60} devices with varying tetracene content and showed that the singlet fission efficiency, as measured through the magnetic field effect stayed constant even when the concentration of tetracene was reduced, thereby demonstrating that it is possible for singlet fission to be implemented in bulk heterojunction OPVs. This is an important result since many of the high efficiency OPVs are solution processed bulk heterojunction devices.

Next we extended our exploration of singlet fission materials by fabricating a 5,6-diphenyl-tetracene (DPT) – C_{60} device. And we found that on application of a magnetic field the photocurrent increased rather than decreased as it did for the tetracene device. This led us to conclude that the charge transfer state (CT) energy at in the DPT device was too high for the triplets to dissociate. This work helped us identify the magnetic field as a probe to investigate energetics at the interface of singlet fission devices.

We used lead chalcogenide quantum dots(QD) as the required low band gap acceptor in singlet fission devices. We paired PbS and PbSe QD with pentacene and saw internal quantum efficiency of 35% in

pentacene. We saw high EQE when we paired pentacene with QD of higher energy than the triplet in pentacene providing clear evidence that the pentacene triplets were splitting at the heterojunction and not energy transferring to the QD. The QD sizes, and hence energies, gave us a lever to vary the LUMO level of the acceptor. EQE measurements indicate at which point the CT energy is too large for triplet dissociation to occur.

The last two works provided two probes to investigate triplet dissociation in singlet fission devices. Using the methods and results from above we looked at various devices fabricated with pentacene and 6,13-diphenyl-pentacene(DPP) as singlet fission donors, and C_{60}, perylene diimides, PbS QD and PbSe QD as acceptors. Some of these devices allowed dissociation pentacene and DPP triplets, and others did not. We concluded that the PbSe QD show the most promise as good acceptors in singlet fission photovoltaics.

We saw that singlet fission can be efficient in a bulk heterojunction. In the search for higher efficiency, cheaply manufactured solar cells, it would be useful endeavor to fabricate solution processed bulk heterojunction structures using singlet fission materials and low energy absorbers like lead chalcogenide QD. Singlet fission photovoltaics are limited somewhat by the library of materials available today. Tetracene and pentacene and their derivatives are the only efficient singlet fission materials and they are not necessarily good absorbers. Synthesis of new singlet fission materials can help us reach the goal of more efficient solar cells through singlet fission. The products of singlet fission, triplets, are dark states. If the energy from a triplet can be transferred to an emissive state, the efficient multi-exciton generation process of singlet fission can be exploited in configurations other than organic solar cells like Luminescent Solar Concentrators or in conjunction with inorganic photovoltaics.

References

1. *Key World Energy Statistics*. 2010, International Energy Agency.

2. *NREL, UCLA Certify World Record for Polymer Solar Cell Efficiency*. 2012 [cited; Available from: http://www.nrel.gov/news/press/2012/1801.html.

3. *Solarbuzz*. 2012 [cited; Available from: http://www.solarbuzz.com/going-solar/understanding/technologies.

4. *NREL - Best Research-Cell Efficiencies*. [cited; Available from: http://www.nrel.gov/ncpv/images/efficiency_chart.jpg.

5. *SolarBuzz*. [cited; Available from: http://www.solarbuzz.com.

6. Fthenakis, V.M. and H.C. Kim, *Photovoltaics: Life-cycle analyses*. Solar Energy. **85**(8): p. 1609-1628.

7. *First Solar Press Release*. 2012 [cited 2012 Aril 2, 2012]; Available from: http://investor.firstsolar.com/releasedetail.cfm?releaseid=639463.

8. Wu, X., *High-efficiency polycrystalline CdTe thin-film solar cells*. Solar Energy, 2004. **77**(6): p. 803-814.

9. *TSMC CIGS modules on display at 26th EU PVSEC*. 2011 [cited; Available from: http://guntherportfolio.com/2011/09/tsmc-solar-ramping-cigs-photovoltaic-module-production/.

10. *NREL-Photovoltaics Research*. 2011 [cited; Available from: http://www.nrel.gov/pv/thinfilm.html.

11. Ramanathan, K., et al., *Properties of 19.2% efficiency ZnO/CdS/CuInGaSe2 thin-film solar cells*. Progress in Photovoltaics, 2003. **11**(4): p. 225-230.

12. *Konarka*. [cited; Available from: www.konarka.com.

13. Gaudiana, R. and C. Brabec, *Organic materials: Fantastic plastic*. Nat Photon, 2008. **2**(5): p. 287-289.

14. Shockley, W. and H.J. Queisser, *Detailed balance limit of efficiency of p-n junction solar cells*. Journal of Applied Physics, 1961. **32**(3): p. 510-519.

15. Brown, N. *Solar Junction Breaks Concentrated Solar World Record with 43.5% Efficiency*. Clean Technica 2011 [cited 2011 April 19, 2011]; Available from: http://cleantechnica.com/2011/04/19/solar-junction-breaks-concentrated-solar-world-record-with-43-5-efficiency/.

16. Naka, S., et al., *Carrier transport properties of organic materials for EL device operation*. Synthetic Metals, 2000. **111â€"112**(0): p. 331-333.

17. Sundar, V.C., et al., *Elastomeric Transistor Stamps: Reversible Probing of Charge Transport in Organic Crystals.* Science, 2004. **303**(5664): p. 1644-1646.

18. Gardener, J., et al., *A scanning tunnelling microscopy investigation into the initial stages of copper phthalocyanine growth on passivated silicon surfaces.* Surface Science, 2008. **602**(4): p. 843-851.

19. Pauling, L., *THE NATURE OF THE CHEMICAL BOND. APPLICATION OF RESULTS OBTAINED FROM THE QUANTUM MECHANICS AND FROM A THEORY OF PARAMAGNETIC SUSCEPTIBILITY TO THE STRUCTURE OF MOLECULES.* Journal of the American Chemical Society, 1931. **53**(4): p. 1367-1400.

20. *UC Davis, Chemi Wiki.* [cited; Available from: http://chemwiki.ucdavis.edu/Organic_Chemistry/Organic_Chemistry_With_a_Biological_Emphasis/Chapter_1:_Chapter_1:_Introduction_to_organic_structure_and_bonding_I/Section_5:_Valence_bond_theory.

21. Kim, Y., et al., *A strong regioregularity effect in self-organizing conjugated polymer films and high-efficiency polythiophene:fullerene solar cells.* Nat Mater, 2006. **5**(3): p. 197-203.

22. Warta, W. and N. Karl, *Hot holes in naphthalene: High, electric-field-dependent mobilities.* Physical Review B, 1985. **32**(2): p. 1172-1182.

23. Celebi, K., et al., *The density of states in thin film copper phthalocyanine measured by Kelvin probe force microscopy.* Applied Physics Letters, 2008. **93**(8).

24. Marianer, S. and B.I. Shklovskii, *EFFECTIVE TEMPERATURE OF HOPPING ELECTRONS IN A STRONG ELECTRIC-FIELD.* Physical Review B, 1992. **46**(20): p. 13100-13103.

25. Baranovskii, S.D., et al., *EFFECTIVE TEMPERATURE FOR ELECTRONS IN BAND TAILS.* Journal of Non-Crystalline Solids, 1993. **166**: p. 437-440.

26. Limketkai, B.N., P. Jadhav, and M.A. Baldo, *Electric field dependent percolation model of charge carrier mobility in amorphous organic semiconductors.* Physical Review B, 2007. **75**: p. 113203.

27. Miller, A. and E. Abrahams, *Impurity Conduction at Low Concentrations.* Physical Review, 1960. **120**(3): p. 745-755.

28. Vissenberg, M.C.J.M., *Opto-Electronic Properties of Disordered Organic Semiconductors*. 1999: University of Leiden.

29. Pike, G.E. and C.H. Seager, *Percolation and Conductivity - Computer Study .1.* Physical Review B, 1974. **10**(4): p. 1421-1434.

30. Yan, H., et al., *A high-mobility electron-transporting polymer for printed transistors.* Nature, 2009. **457**(7230): p. 679-U1.

31. Ritjareonwattu, S., et al., *Enhanced sensitivity of an organic field-effect transistor pH sensor using a fatty acid Langmuir-Blodgett film.* Organic Electronics, 2010. **11**(11): p. 1792-1795.

32. Someya, T., et al., *A large-area, flexible pressure sensor matrix with organic field-effect transistors for artificial skin applications.* Proceedings of the National Academy of Sciences of the United States of America, 2004. **101**(27): p. 9966-9970.

33. Bouvet, M., *Phthalocyanine-based field-effect transistors as gas sensors.* Analytical and Bioanalytical Chemistry, 2006. **384**(2): p. 366-373.

34. Atkins, P.W. and R.S. Friedman, *The Pauli Principle*, in *Molecular Quantum Mechanics*. 2011, Oxford. p. 227-229.

35. Hill, I.G., et al., *Charge-separation energy in films of pi-conjugated organic molecules.* Chemical Physics Letters, 2000. **327**: p. 181-188.

36. Veldman, D., S.C.J. Meskers, and R.A.J. Janssen, *The Energy of Charge-Transfer States in Electron Donor–Acceptor Blends: Insight into the Energy Losses in Organic Solar Cells.* Advanced Functional Materials, 2009. **19**(12): p. 1939-1948.

37. Peumans, P., V. Bulovic, and S.R. Forrest, *Efficient, high-bandwidth organic multilayer photodetectors.* Applied Physics Letters, 2000. **76**(20): p. 3855-3857.

38. Hofberger, W. and H. Bassler, *DIFFUSION OF TRIPLET EXCITONS IN AMORPHOUS TETRACENE.* Physica Status Solidi B-Basic Research, 1975. **69**(2): p. 725-730.

39. Rand, B.P., D.P. Burk, and S.R. Forrest, *Offset energies at organic semiconductor heterojunctions and their influence on the open-circuit voltage of thin-film solar cells.* Physical Review B, 2007. **75**(11): p. 115327.

40. Tang, C.W., *Two-layer organic photovoltaic cell.* Applied Physics Letters, 1985. **48**(2): p. 183-185.

41. Li, G., et al., *High-efficiency solution processable polymer photovoltaic cells by self-organization of polymer blends.* Nature Materials, 2005. **4**(11): p. 864-868.

42. Gilot, J., M.M. Wienk, and R.A.J. Janssen, *Optimizing Polymer Tandem Solar Cells.* Advanced Materials. **22**(8): p. E67-E71.

43. Kalowekamo, J. and E. Baker, *Estimating the manufacturing cost of purely organic solar cells.* Solar Energy, 2009. **83**(8): p. 1224-1231.

44. *Update of the MIT 2003 Future of Nuclear Power Study*. 2009, Massachusetts Institute of Technology.

45. Peters, C.H., et al., *The Mechanism of Burn-in Loss in a High Efficiency Polymer Solar Cell.* Advanced Materials, 2012. **24**(5): p. 663-+.

46. Krebs, F.C., et al., *Manufacture, integration and demonstration of polymer solar cells in a lamp for the "Lighting Africa" initiative.* Energy & Environmental Science, 2010. **3**(5): p. 512-525.

47. Swenberg, C.E. and W.T. Stacy, *Bimolecular radiationless transitions in crystalline tetracene.* Chemical Physics Letters, 1968. **2**(5): p. 327-328.

48. Merrifield, R.E., P. Avakian, and R.P. Groff, *Fission of singlet excitons into pairs of triplet excitons in tetracene crystals.* Chemical Physics Letters, 1969. **3**: p. 155-157.

49. Jundt, C., et al., *Exciton dynamics in pentacene thin-films studied by pump-probe spectroscopy.* Chemical Physics Letters, 1995. **241**(1-2): p. 84-88.

50. Thorsmolle, V.K., et al., *Morphology effectively controls singlet-triplet exciton relaxation and charge transport in organic semiconductors.* Physical Review Letters, 2009. **102**(1): p. 017401.

51. Hanna, M.C. and A.J. Nozik, *Solar conversion efficiency of photovoltaic and photoelectrolysis cells with carrier multiplication absorbers.* Journal of Applied Physics, 2006. **100**(7).

52. Sukhovatkin, V., et al., *Colloidal Quantum-Dot Photodetectors Exploiting Multiexciton Generation.* Science, 2009. **324**(5934): p. 1542-1544.

53. Conibeer, G.J., et al., *Selective energy contacts for hot carrier solar cells.* Thin Solid Films, 2008. **516**(20): p. 6968-6973.

54. Ross, R.T. and A.J. Nozik, *EFFICIENCY OF HOT-CARRIER SOLAR-ENERGY CONVERTERS.* Journal of Applied Physics, 1982. **53**(5): p. 3813-3818.

55. Brown, A.S. and M.A. Green, *Impurity photovoltaic effect: Fundamental energy conversion efficiency limits.* Journal of Applied Physics, 2002. **92**(3): p. 1329-1336.

56. Schaller, R.D. and V.I. Klimov, *High efficiency carrier multiplication in PbSe nanocrystals: Implications for solar energy conversion.* Physical Review Letters, 2004. **92**(18).

57. Nair, G. and M.G. Bawendi, *Carrier multiplication yields of CdSe and CdTe nanocrystals by transient photoluminescence spectroscopy.* Physical Review B, 2007. **76**(8).

58. Sambur, J.B., T. Novet, and B.A. Parkinson, *Multiple Exciton Collection in a Sensitized Photovoltaic System.* Science, 2010. **330**(6000): p. 63-66.

59. Nozik, A.J., *Multiple exciton generation in semiconductor quantum dots.* Chemical Physics Letters, 2008. **457**(1â€“3): p. 3-11.

60. Kepler, R.G., et al., *Triplet excitons and Delayed Fluorescence in Anthracene Crystals.* Physical Review Letters, 1963. **10**(9): p. 400.

61. Birks, J.B., T.A. King, and I.H. Munro, *The Photoluminescence Decay of Organic Crystals.* Proceedings of the Physical Society, 1962. **80**(2): p. 355.

62. Singh, S., et al., *LASER GENERATION OF EXCITONS AND FLUORESCENCE IN ANTHRACENE CRYSTALS.* Journal of Chemical Physics, 1965. **42**(1): p. 330-&.

63. Kazzaz, A.A. and A.B. Zahlan, *TEMPERATURE DEPENDENCE OF CRYSTALLINE TETRACENE FLUORESCENCE.* Journal of Chemical Physics, 1968. **48**(3): p. 1242-&.

64. Geacintov, N., M. Pope, and F. Vogel, *Effect of magnetic field on fluorescence of tetracene crystals - exciton fission.* Physical Review Letters, 1969. **22**(12): p. 593-596.

65. Johnson, R.C. and R.E. Merrifield, *Effects of Magnetic Fields on the Mutual Annihilation of Triplet Excitons in Anthracene Crystals.* Physical Review B, 1970. **1**(2): p. 896-902.

66. Klein, G., R. Voltz, and M. Schott, *Magnetic-field effect on prompt fluorescence in anthracene - evidence for singlet exciton fission.* Chemical Physics Letters, 1972. **16**(2): p. 340-344.

67. Groff, R.P., G.P. Avakian, and R.E. Merrifield, *Coexistence of exciton fission and fusion in tetracene crystals.* Physical Review B, 1970. **1**(2): p. 815-817.

68. Burdett, J.J., et al., *Excited state dynamics in solid and monomeric tetracene: The roles of superradiance and exciton fission.* Journal of Chemical Physics, 2010. **133**(14): p. 12.

69. Silinsh, E.A. and V. Capek, ***Organic Molecular Crystals: Interaction, Localization, and Transport Phenomena***. 1994, Woodbury: AIP Press.

70. Yoshizawa, M., M. Taiji, and T. Kobayashi, *RELAXATION DYNAMICS OF PHOTOEXCITATIONS IN POLYDIACETYLENE FILMS.* IEEE Journal of Quantum Electronics, 1989. **25**(12): p. 2532-2539.

71. Ishihara, S., et al., *Relaxation dynamics of photoexcitations in C-60 films.* Chemical Physics Letters, 1998. **295**(5-6): p. 475-480.

72. Moses, D., A. Dogariu, and A.J. Heeger, *Ultrafast photoinduced charge generation in conjugated polymers.* Chemical Physics Letters, 2000. **316**(5-6): p. 356-360.

73. Rademaker, H., et al., *CAROTENOID TRIPLET YIELDS IN NORMAL AND DEUTERATED RHODOSPIRILLUM-RUBRUM.* Biochimica et Biophysica acta, 1980. **592**(2): p. 240-257.

74. Austin, R.H., et al., *MAGNETIC-FIELD EFFECTS ON TRIPLET EXCITON FISSION AND FUSION IN A POLYDIACETYLENE.* Journal of Chemical Physics, 1989. **90**(11): p. 6642-6646.

75. Paci, I., et al., *Singlet Fission for Dye-Sensitized Solar Cells:â€‰ Can a Suitable Sensitizer Be Found?* Journal of the American Chemical Society, 2006. **128**(51): p. 16546-16553.

76. Schwerin, A.F., et al., *Toward Designed Singlet Fission: Electronic States and Photophysics of 1,3-Diphenylisobenzofuranâ€* The Journal of Physical Chemistry A, 2009. **114**(3): p. 1457-1473.

77. Johnson, R.C. and Merrifie.Re, *EFFECTS OF MAGNETIC FIELDS ON MUTUAL ANNIHILATION OF TRIPLET EXCITONS IN ANTHRACENE CRYSTALS.* Physical Review B-Solid State, 1970. **1**(2): p. 896-&.

78. Suna, A., *KINEMATICS OF EXCITON-EXCITON ANNIHILATION IN MOLECULAR CRYSTALS.* Physical Review B, 1970. **1**(4): p. 1716-&.

79. Smith, M.B. and J. Michl, *Singlet Fission.* Chemical Reviews, 2010. **110**(11): p. 6891-6936.

80. Chan, W.-L., et al., *Observing the Multiexciton State in Singlet Fission and Ensuing Ultrafast Multielectron Transfer.* Science, 2011. **334**(6062): p. 1541-1545.

81. Lee, J., P. Jadhav, and M.A. Baldo, *High efficiency organic multilayer photodetectors based on singlet exciton fission.* Applied Physics Letters, 2009. **95**(3): p. 033301.

82. Funfschilling, J., et al., *QUANTUM BEATS IN THE FLUORESCENCE DECAY OF TETRACENE CRYSTALS.* Helvetica Physica Acta, 1985. **58**(2-3): p. 347-354.

83. Burdett, J.J. and C.J. Bardeen, *Quantum beats in crystalline tetracene delayed fluorescence due to triplet pair coherences produced by direct singlet fission.* Journal of the American Chemical Society, 2012.

84. Grumstrup, E.M., J.C. Johnson, and N.H. Damrauer, *Enhanced Triplet Formation in Polycrystalline Tetracene Films by Femtosecond Optical-Pulse Shaping.* Physical Review Letters, 2010. **105**(25): p. 257403.

85. Lim, S.-H., et al., *Exciton Delocalization and Superradiance in Tetracene Thin Films and Nanoaggregates.* Physical Review Letters, 2004. **92**(10): p. 107402.

86. Peumans, P., A. Yakimov, and S.R. Forrest, *Small molecular weight organic thin-film photodetectors and solar cells.* Journal of Applied Physics, 2003. **93**(7): p. 3693-3723.

87. Peumans, P. and S.R. Forrest, *Very-high-efficiency double-heterostructure copper phthalocyanine/C-60 photovoltaic cells.* Applied Physics Letters, 2001. **79**(1): p. 126-128.

88. Hill, I.G. and A. Kahn, *Combined photoemission/in vacuo transport study of the indium tin oxide/copper phthalocyanine/N,N '-diphenyl-N,N '-bis(l-naphthyl)-1,1 ' biphenyl-4,4 '' diamine molecular organic semiconductor system.* Journal of Applied Physics, 1999. **86**(4): p. 2116-2122.

89. Kochi, M., et al., *Photoemission from Organic Crystal in Vacuum Ultraviolet Region. IV.* Bulletin of the Chemical Society of Japan, 1970. **43**(9): p. 2690-2702.

90. Dexter, D.L., *A theory of sensitized luminescence in solids.* Journal of Chemical Physics, 1953. **21**: p. 836-850.

91. Hepp, A., et al., *Light-Emitting Field-Effect Transistor Based on a Tetracene Thin Film.* Physical Review Letters, 2003. **91**(15): p. 157406.

92. Aladekomo, J.B., S. Arnold, and M. Pope, *Triplet exciton diffusion and double photon absorption in tetracene.* physica status solidi (b), 1977. **80**(1): p. 333-340.

93. Pope, M. and C. Swenberg, *Electronic Processes in Organic Crystals*. 1st ed. 1982, Oxford: Oxford University Press.

94. Chu, C.W., et al., *Efficient photovoltaic energy conversion in tetracene-C-60 based heterojunctions.* Applied Physics Letters, 2005. **86**(24).

95. Burkhard, G.F., E.T. Hoke, and M.D. McGehee, *Accounting for Interference, Scattering, and Electrode Absorption to Make Accurate Internal Quantum Efficiency Measurements in Organic and Other Thin Solar Cells.* Advanced Materials, 2010. **22**(30): p. 3293-3297.

96. Kraabel, B., et al., *Ultrafast spectroscopic studies of photoinduced electron transfer from semiconducting polymers to C_{60}.* Physical Review B, 1994. **50**(24): p. 18543.

97. Brabec, C.J., et al., *Tracing photoinduced electron transfer process in conjugated polymer/fullerene bulk heterojunctions in real time.* Chemical Physics Letters, 2001. **340**(3-4): p. 232-236.

98. Dutton, G.J., et al., *Ultrafast charge-transfer processes at an oriented phthalocyanine/C-60 interface.* Physical Review B. **82**(7).

99. Zimmerman, P.M., Z.Y. Zhang, and C.B. Musgrave, *Singlet fission in pentacene through multi-exciton quantum states.* Nature Chemistry, 2010. **2**(8): p. 648-652.

100. Jadhav, P.J., et al., *Singlet Exciton Fission in Nanostructured Organic Solar Cells.* Nano Letters: p. null-null.

101. Roberts, S.T., et al., *Observation of Triplet Exciton Formation in a Platinum-Sensitized Organic Photovoltaic Device.* The Journal of Physical Chemistry Letters. **2**(2): p. 48-54.

102. Burgdorff, C., T. Kircher, and H.G. Löhmannsröben, *Photophysical properties of tetracene derivatives in solution.* Spectrochimica Acta Part A: Molecular Spectroscopy, 1988. **44**(11): p. 1137-1141.

103. Segal, M., et al., *Frequency response and origin of the spin- 1/2 photoluminescence-detected magnetic resonance in a pi -conjugated polymer.* Physical Review B, 2005. **71**(24): p. 245201.

104. Hu, B. and Y. Wu, *Tuning magnetoresistance between positive and negative values in organic semiconductors.* Nat Mater, 2007. **6**(12): p. 985-991.

105. Shen, C. and A. Kahn, *Electronic structure, diffusion, and p-doping at the <equation>Au/F₁₆CuPc</equation> interface.* Journal of Applied Physics, 2001. **90**(9): p. 4549-4554.

106. Weaver, J.H., *ELECTRONIC-STRUCTURES OF C-60, C-70 AND THE FULLERIDES - PHOTOEMISSION AND INVERSE PHOTOEMISSION-STUDIES.* Journal of Physics and Chemistry of Solids, 1992. **53**(11): p. 1433-1447.

107. Jiang, X., et al., *Organic photovoltaic cells using hexadecafluorophthalocyaninatocopper (F16CuPc) as electron acceptor material.* Chemical Physics Letters, 2007. **446**(4-6): p. 329-332.

108. Xu, Z. and B. Hu, *Photovoltaic Processes of Singlet and Triplet Excited States in Organic Solar Cells.* Advanced Functional Materials, 2008. **18**(17): p. 2611-2617.

109. Vandewal, K., et al., *On the origin of the open-circuit voltage of polymer-fullerene solar cells.* Nat Mater, 2009. **8**(11): p. 904-909.

110. Groff, R.P., P. Avakian, and R.E. Merrifield, *Magnetic field dependence of delayed fluorescence from tetracene crystals.* Journal of Luminescence, 1970. **1-2**: p. 218-223.

111. Jadhav, P.J., et al., *Singlet Exciton Fission in Nanostructured Organic Solar Cells.* Nano Letters, 2011. **11**(4): p. 1495-1498.

112. McDonald, S.A., et al., *Solution-processed PbS quantum dot infrared photodetectors and photovoltaics.* Nature Materials, 2005. **4**(2): p. 138-142.

113. Zhao, N., et al., *Colloidal PbS Quantum Dot Solar Cells with High Fill Factor.* ACS Nano, 2010. **4**(7): p. 3743-3752.

114. Pattantyus-Abraham, A.G., et al., *Depleted-Heterojunction Colloidal Quantum Dot Solar Cells.* ACS Nano, 2010. **4**(6): p. 3374-3380.

115. Hyun, B.R., et al., *Electron Injection from Colloidal PbS Quantum Dots into Titanium Dioxide Nanoparticles.* ACS Nano, 2008. **2**(11): p. 2206-2212.

116. Jiang, X.M., et al., *PbSe nanocrystal/conducting polymer solar cells with an infrared response to 2 micron.* Journal of Materials Research, 2007. **22**(8): p. 2204-2210.

117. Tang, J., et al., *Colloidal-quantum-dot photovoltaics using atomic-ligand passivation.* Nature Materials, 2011. **10**(10): p. 765-771.

118. Sargent, E.H., *Colloidal quantum dot solar cells.* Nat Photon, 2012. **6**(3): p. 133-135.

119. Navaneethan, M., et al., *OPTICAL, STRUCTURAL AND SURFACE MORPHOLOGICAL STUDIES OF N-METHYLANILINE CAPPED LEAD SULPHIDE NANOPARTICLES.* Reviews on Advanced Materials Science, 2009. **21**(2): p. 217-224.

120. Lipovskii, A., et al., *Synthesis and characterization of PbSe quantum dots in phosphate glass.* Applied Physics Letters, 1997. **71**(23): p. 3406-3408.

121. Weddemann, A., et al., *Review and outlook: from single nanoparticles to self-assembled monolayers and granular GMR sensors.* Beilstein Journal of Nanotechnology, 2010. **1**: p. 75-93.

122. Liu, Y., et al., *Dependence of Carrier Mobility on Nanocrystal Size and Ligand Length in PbSe Nanocrystal Solids.* Nano Letters, 2010. **10**(5): p. 1960-1969.

123. Ma, X., et al. *Hybrid polymer-nanocrystal heterostructures for high-performance chip-integrated near-infrared LEDs*. in *Group IV Photonics (GFP), 2011 8th IEEE International Conference on*. 2011.

124. Brown, P.R. 2012.

125. Dadosh, T., et al., *Measurement of the conductance of single conjugated molecules.* Nature, 2005. **436**(7051): p. 677-680.

126. Koleilat, G.I., et al., *Efficient, stable infrared photovoltaics based on solution-cast colloidal quantum dots.* Acs Nano, 2008. **2**(5): p. 833-840.

127. Zemel, J.N., J.D. Jensen, and R.B. Schoolar, *ELECTRICAL AND OPTICAL PROPERTIES OF EPITAXIAL FILMS OF PBS PBSE PBTE AND SNTE.* Physical Review, 1965. **140**(1A): p. A330-&.

128. Moreels, I., et al., *Dielectric function of colloidal lead chalcogenide quantum dots obtained by a Kramers-Kronig analysis of the absorbance spectrum.* Physical Review B, 2010. **81**(23).

129. Ma, W., et al., *Photovoltaic Performance of Ultrasmall PbSe Quantum Dots.* Acs Nano, 2011. **5**(10): p. 8140-8147.

130. Johnston, K.W., et al., *Efficient Schottky-quantum-dot photovoltaics: The roles of depletion, drift, and diffusion.* Applied Physics Letters, 2008. **92**(12).

131. Brown, P.R., et al., *Improved Current Extraction from ZnO/PbS Quantum Dot Heterojunction Photovoltaics Using a MoO3 Interfacial Layer.* Nano Letters, 2011. **11**(7): p. 2955-2961.

132. Luther, J.M., et al., *Schottky Solar Cells Based on Colloidal Nanocrystal Films.* Nano Letters, 2008. **8**(10): p. 3488-3492.

133. Klem, E.J.D., et al., *Efficient solution-processed infrared photovoltaic cells: Planarized all-inorganic bulk heterojunction devices via inter-quantum-dot bridging during growth from solution.* Applied Physics Letters, 2007. **90**(18): p. 183113.

134. Yoo, S., B. Domercq, and B. Kippelen, *Efficient thin-film organic solar cells based on pentacene/C-60 heterojunctions.* Applied Physics Letters, 2004. **85**(22): p. 5427-5429.

135. Picciolo, L.C., H. Murata, and Z.H. Kafafi, *Organic light-emitting devices with saturated red emission using 6,13-diphenylpentacene.* Applied Physics Letters, 2001. **78**(16): p. 2378-2380.

136. Kahn, A., N. Koch, and W.Y. Gao, *Electronic structure and electrical properties of interfaces between metals and pi-conjugated molecular films.* Journal of Polymer Science Part B-Polymer Physics, 2003. **41**(21): p. 2529-2548.

137. Griffith, O.L., et al., *Electronic Properties of Pentacene versus Triisopropylsilylethynyl-Substituted Pentacene: Environment-Dependent Effects of the Silyl Substituent.* Journal of the American Chemical Society, 2009. **132**(2): p. 580-586.

138. Choi, J.J., et al., *PbSe Nanocrystal Excitonic Solar Cells.* Nano Letters, 2009. **9**(11): p. 3749-3755.

139. Jasieniak, J., M. Califano, and S.E. Watkins, *Size-Dependent Valence and Conduction Band-Edge Energies of Semiconductor Nanocrystals.* ACS Nano, 2011. **5**(7): p. 5888-5902.